2017

The physical principle of magnetic phase transition for the magnetocaloric materials: RCo2Mnx AND Tb1-xYxMn2Ge2 (R = Tb, Ho, Dy, 0 ≤ ?? ≤ 11.00) series compounds

Chunsheng Fang

THE PHYSICAL PRINCIPLE OF MAGNETIC PHASE TRANSITION FOR THE MAGNETOCALORIC MATERIALS: RCo_2Mn_x AND $Tb_{1-x}Y_xMn_2Ge_2$ (R = Tb, Ho, Dy, $0 \leq x \leq 1.0$) SERIES COMPOUNDS

A thesis submitted in fulfilment of the
requirements for the award of the degree

DOCTOR OF PHILOSOPHY

From

UNIVERSITY OF WOLLONGONG

By

Chunsheng Fang

Institute of Superconducting & Electronic Materials (ISEM), University of Wollongong

Faculty of Engineering and Information Science

CERTIFICATION

I, Chunsheng Fang, declare that this thesis, submitted in fulfilment of the requirements for the award of Doctor of Philosophy, in the Institute of superconducting and electronic materials, University of Wollongong, is wholly my own work unless otherwise referenced or acknowledged. The document has not been submitted for qualifications at any other academic institution.

The following publications are related to the research work conducted in this study:

C. S. Fang, J. L. Wang, W. D. Hutchison， S. X. Dou, S. J. Campbell & Z. X. Cheng, "Tuning the magnetic and structural transitions in $TbCo_2Mn_x$ compounds" Phys. Rev. B **96**, 064425 (2017). (Related to Chapter 3)

C. S. Fang, et al, "Tuning magnetic properties and thermal expansion in designed $HoCo_2Mn_x$ compounds" **(to be submitted).** (Related to Chapter 4)

C. S. Fang, et al, "Systematic investigation on the $DyCo_2Mn_x$ (x = 0, 0.1, 0.2, 0.4, 0.6 and 1.0) compounds" **(to be submitted).** (Related to Chapter 5)

C. S. Fang, G. X. Li, J. L. Wang, W. D. Hutchison, Q. Y. Ren, Z. Y. Deng, G. H. Ma, S. X. Dou, S. J. Campbell & Z. X. Cheng, "New insight into magnetostructural phase transitions in layered $TbMn_2Ge_2$-based compounds" Scientific reports **7,** 45814 (2017). (Related to Chapter 6)

October 7, 2017

Abstract

Since $Gd_5(Si_2Ge_2)$ was found to have huge magnetic entropy near room temperature, various magnetocaloric materials have been produced and investigated. Meanwhile, different methods were used to optimize their magnetic properties, such as element doping, applying strong magnetic fields or mechanical pressure, etc. My work during this PhD study has been mainly focused on the Mn doped RCo_2Mn_x (R = Tb, Ho, Dy， $0 \leq x \leq 1.0$) series compounds. It was found that all the Mn doped samples are isostructural to RCo_2 series compounds with the cubic $MgCu_2$ structure ($Fd\bar{3}m$ space group). To further investigate the Mn doping effect on the magnetic properties such as the Curie temperature (T_C), the coercivity (H_C), the spontaneous magnetic moment (M_S), and the magnetic entropy change ($-\Delta S$), magnetic measurement were performed on a physical properties measurement system (PPMS). Meanwhile, critical exponent analysis was conducted for all the second order transitions belonging to the three-dimensional (3D) Heisenberg model, mean-field theory, or 3D Ising model. High resolution neutron and synchrotron measurements were then carried out to clarify the magnetic transitions and the crystal structure transitions during the magnetic-state transitions. By the way another series compounds $Tb_{1-x}Y_xMn_2Ge_2$ (x = 0, 0.1, 0.2) was studied and included in the thesis.

For the first part of the research, novel $TbCo_2Mn_x$ compounds (x = 0, 0.1, 0.2, and 0.3) were synthesized using the standard arc melting method. $TbCo_2Mn_x$ compounds at room temperature crystallize in the cubic $MgCu_2$-type structure, being isostructural to $TbCo_2$, although the doped Mn atom breaks the ideal stoichiometric ratio of rare earth to transition-metal element (1:2). With increasing Mn content from x = 0 to 0.3, the Curie temperature T_C increases significantly from 227 K to 332 K, while spontaneous magnetization at 5 K decreases from 6.19 to 5.0 μ_B/f.u. Furthermore, the nature of the magnetic transition around T_C changes from the first order for x = 0 to second order for x = 0.1, 0.2, and 0.3. To further clarify the nature of the second order transitions, we carried out a detailed critical exponent study. The derived critical exponents are close to the theoretical prediction from the mean-field model, indicating that the magnetic interactions are long-range. Neutron (5 K−400 K) and synchrotron (90 K−400 K) diffraction patterns confirmed that, in $TbCo_2Mn_x$ compounds, the Mn atoms occupied both Tb and Co sites. The compounds exhibit a rhombohedral distortion below T_C, with the structure changing from cubic $Fd\bar{3}m$ at above T_C to $R\bar{3}m$ below T_C.

For the second part of the research, $HoCo_2Mn_x$ (x = 0, 0.2, 0.5, 0.7 and 1.0) series compounds were synthesized and characterized by the x-ray diffraction and found to be pure single phase compounds isostructural to the original compound $HoCo_2$ with $MgCu_2$-type structure (space group $Fd\bar{3}m$). Curie temperature was significantly raised from T_C = 88 K for $HoCo_2$ to T_C =253 K for $HoCo_2Mn$ due to the addition of Mn. Similar to $HoCo_2$, spin reorientations with the easy magnetization direction from [100] to [110] occur for all $HoCo_2Mn_x$ compounds during cooling. Neutron diffraction revealed that the compounds with x < 0.7 had strong magneto-elastic coupling accompanying their magnetic transitions around both Curie temperature T_C and spin reorientation temperature T_{sr}. Unusual transformation from strong negative to positive thermal expansion in $HoCo_2Mn_x$ compounds had been detected. Almost zero thermal expansion over a wide temperature range (over 200 K) can be achieved in the compound $HoCo_2Mn_{0.5}$. A magnetic phase diagram had been constructed. Besides, a broad operational temperature range during the paramagnetism-ferromagnetism (PM-FM) transition was found with higher Mn doping: from the range of 80-120K for $HoCo_2$ to 40-280 K for $HoCo_2Mn$. Meanwhile, the nature of the magnetic transition transformed from first order for $HoCo_2$ to second order for the Mn doped materials. Furthermore, to deeply investigate the nature of the second order phase transition, critical exponent (β, γ, and δ) analysis using different techniques such as Arrott-Noaks plots, Kouvel-Fisher plots, and isotherm analysis was conducted. It proved that with higher Mn doping, the nature of the second order transition transformed from the mean-field theory prediction for x = 0.2 to some deviation from the mean-field theory for x = 0.5, 0.7, and 1.0.

For the third part of the research, a series of $DyCo_2Mn_x$ (x = 0, 0.1, 0.2, 0.4, 0.6, and 1.0) compounds were characterised and found to be pure and isostructural to $DyCo_2$ with cubic structure ($Fd\bar{3}m$ space group). It was found that with the more Mn doping, the Curie temperature increased with the spontaneous magnetization M_S, while the magnetic entropy change decreased. In addition, huge coercivity H_C appeared after more Mn doping. The nature of the magnetic transition was transformed from first order for $DyCo_2$ to second order for the Mn doped materials. To analyse the nature (3D Heisenberg model, mean-field theory, or 3D Ising model) of all the second order transitions, the critical exponents $\beta \approx 0.5$, $\gamma \approx 1.0$, and $\delta \approx 3.0$ were calculated using different methods such as Arrott-Noaks plots, Kouvel-Fisher plots, and critical isotherm analysis. The results proved that all the second order transitions are close to the mean-field theory predictions with long-range interaction.

In the final part of the research, the critical magnetic behaviour around first order transitions in the $Tb_{1-x}Y_xMn_2Ge_2$ series (x = 0, 0.1, 0.2) was investigated in detail. All the compounds were found to exhibit two magnetic phase transitions. On cooling from the paramagnetic region, the first transition from the paramagnetic state (PM) to the antiferromagnetic interlayer (AFil) state occurs at the temperature T_N^{inter}, with the second transition from the AFil magnetic structure to a collinear ferrimagnetic interlayer structure taking place at the temperature T_C^{inter}. Compared with only a slight change in T_N^{inter} (409 K, 410 K, and 417 K for x = 0, 0.1, and 0.2, respectively), the substitution of Y for Tb led to a significant decrease in T_C^{inter} from 97.5 K for x = 0 to 74.6 K for x = 0.2, This behaviour was fully investigated by calculating the proportions of two effects (1) chemical pressure due to the smaller atomic size of Y compared with Tb and (2) the magnetic dilution effect due to the non-magnetic nature of Y. In addition, a strong anisotropic magnet-volume effect has been detected around T_C^{inter} in all compounds with relative change in the lattice constant $\Delta a/a$ = 0.125%, 0.124% and 0.130% for x = 0, 0.1, and 0.2, respectively, while no obvious effect was detected along the c-axis. The maximum magnetic entropy changes were found to be $-\Delta S_{max}$ = 9.1 J kg^{-1} K^{-1}, 11.9 J kg^{-1} K^{-1}, and 6.3 J kg^{-1} K^{-1} with a field change from 0 T to 5 T for $TbMn_2Ge_2$, $Tb_{0.9}Y_{0.1}Mn_2Ge_2$, and $Tb_{0.8}Y_{0.2}Mn_2Ge_2$, respectively.

ACKNOWLEDGEMENTS

First of all, I would like to thank my supervisors, Prof. Zhenxiang Cheng and Dr. Jianli Wang, for their great helps. This thesis would not have been completed without their supports. Their kind encouragements and critical suggestions let me do research on this area in a right way. Sincere appreciation also goes to Prof. Stewart Campbell, Dr. Wayne Hutchison (from UNSW at Canberra), Dr. Tania Sliver for their contribution to my papers or thesis, and to Dr. Andrew Studer, Dr. Maxim Avdeev, (from ANSTO), Dr. Qinfeng Gu, Dr. J. A. Kimpton, (from Australian Synchrotron), Dr. Zheyin Yu, Dr. Lijuan Zhang and Dr. Qingyong Ren for their enthusiastic helps on my Neutron and Synchrotron measurements.

TABLE OF CONTENTS

LIST OF FIGURES

LIST OF TABLES

LIST OF NOTATIONS

PPMS	Physics property measurement system
PM-FM	parimagnetism-ferromagnetism transition PM
AFil	interlayer antiferromagnetic
ECE	elastocaloric effect
MCE	magnetocaloric effect
C_p	heat capacity
θ_D	Debye temperature
$N\,(E_F)$	electronic density of states
ΔT_{ad}	reversible temperature change
ΔS_m	magnetic entropy
ΔS_r	lattice entropy
ΔS_e	electronic entropy of the free electron
p	the pressure
V	the volume of the sample
μ_0	the magnetic permeability of the vacuum
H	the intensity of the magnetic field
M	the magnetic momentum
σ	the magnetic momentum per unit of mass
$\chi_0^{-1}(0, T)$	inverse initial susceptibility
C_{ph}	heat capacity caused by lattice
C_{el}	heat capacity caused by electronic
C_m	heat capacity caused by magnetic contributions
k	the compressibility
C_v	the specific heat at constant volume caused by lattice vibrations
k_B	Boltzmann constant
ω_s	spontaneous volume magnetostriction (= $\Delta V/V$)
Δp	chemical pressure
V_0,	initial volume
B_0	bulk moduli
B_0'	the first derivative of bulk moduli
$\Delta T_c^{chemical}$	the Curie temperature T_C change caused by the chemical pressure

CHAPTER 1 INTRODUCTION

1.1 Research Background

Nowadays, energy shortage and environment pollution are still two big problems for humanity's development. Scientists are trying to find the environmentally-friendly materials for our technology with high energy efficiency. The materials should be not only easy and cheap to produce, but also have high energy efficiency without releasing pollution. Cooling technology is so important that, regardless of whether it is for achieving extreme conditions for experiments or for ordinary life, it is essential. The traditional refrigeration technology is steam compression refrigeration. There is no longer any potential space, however, to further improve its energy consumption and energy efficiency. The use of traditional refrigerant gases causes ozone depletion and also has global warming potential, which are considerable problems.[1] Thus, new technologies for cooling, such as thermoelectric cooling,[2] thermoacoustic refrigeration, absorption refrigeration[3,4,5] and magnetic refrigeration,[6] have been developed. Among them, the magnetic cooling method was thought to be a promising technique for both extreme low temperatures or room temperature refrigeration.[7] Refrigeration systems depend on the materials entropy change ($-\Delta S$) to absorb or release energy, in accordance with the variation of an external parameter such as the pressure, electric field, or magnetisation. Conventional cooling systems are based on the elastocaloric effect (ECE), while magnetic refrigeration technologies are based on the magnetocaloric effect (MCE), which can be defined as the heat absorption and emission when magnetocaloric materials are subjected to changes in an external magnetic field.

As a new technology for cooling, magnetic refrigeration has become a promising technique because of its both energy efficient and environmentally-friendly features. First, the efficiency of the magnetic cooling process can reach 30%-60% of the Carnot cycle.[8] Secondly, since the cooling only depends on the external magnetic field and magnetocaloric materials, there are no ozone-depleting and greenhouse effects. Compared with the traditional compression refrigeration, the magnetic cooling process gets rid of the compressors with movable components, large rotational speed, mechanical vibration, noise, bad stability, and short longevity.[6] So intensive research on the magnetocaloric materials is very meaningful for the new energy technology and innovation in the future.

1.2 Statement of the Problem

Although the magnetic cooling method has so many advantages compared with the traditional vapour compression refrigeration, there are also some difficulties for the wide application of magnetic refrigeration. Research on magnetocaloric materials is normally focused only on the magnetocaloric materials themselves, but not the entire magnetic refrigeration system. Here are some general considerations for magnetic cooling system application:

1. Tunable Curie temperature of the magnetocaloric materials

The element doping method is a usual method to change the intrinsic magnetic properties such as Curie temperature, magnetic entropy change, etc.[9, 10, 11] Normally after element doping, however, the Curie temperature may increase significantly, while the magnetic entropy change decreases sharply.[12, 13, 14, 15]

2. Large magnetic entropy change

The ideal magnetocaloric material is a material with a large magnetic entropy change while subject to a low external magnetic field.

3. Operational temperature

The operational temperature can be defined as the temperature range of the total peak on the magnetic entropy change $-\Delta S$ depending on the temperature. A large operation temperature range means a wide temperature region applicable where magnetocaloric effect (MCE) decreases slowly as the temperature drops below the Curie temperature (T_C).

4. Strong external magnetic field

At present, a strong magnetic field is still needed to produce large magnetic entropy change. Normally, superconductor magnets, electromagnets, are used to produce high external magnetic fields producing 5-7 T strong magnetic fields. However, using superconductors is very expensiveand needs the extremely low temperatures produced by the liquid-helium cooling. In the case of the electromagnets, too much electric power is needed to produce high magnetic field.

5. Excellent heat regeneration and transfer

Apart from the magnetocaloric material itself, the behaviour of the regenerator and heat exchanger in the refrigeration system is also a key point, so the mechanical and structural design of the refrigerator is also an area where the efficiency of the refrigeration can be improved. In addition, the heat transfer and flow characteristic, such as the internal heat source, flow frequency, flow media, etc., are key factors for the refrigeration capacity. All the above points are just to make the internal heat transfer in the regenerator faster and more abundant to transfer more heat to the external heat exchanger.

1.3 Objectives and Scopes

The objective of our research is not only to explore suitable magnetic materials for magnetic refrigeration, but also to clarify the physical principles during the magnetic transition. So, we have synthesised and investigated a series of magnetic materials, with the main focus on $TbCo_2Mn_x$ (x = 0, 0.1, 0.2, and 0.3), $HoCo_2Mn_x$ (x = 0, 0.2, 0.5, 0.7, and 1.0), $DyCo_2Mn_x$ (x = 0.1, 0.2, 0.4, 0.6, and 1.0). All the crystal structures of the Mn doped materials are all isostructural to the original compounds, Especially for $TbCo_2Mn_x$, $HoCo_2Mn_x$ and $DyCo_2Mn_x$ compounds, the Mn atoms were actually added into both rare earth sites (8a) and Co sites (16d) without substitution for the rare earth and Co, keeping the structure isostructural to the original compound RCo_2 with the $MgCu_2$ structure (space group $Fd\bar{3}m$). This is a novel phenomenon which inspire us to clarify the crystal structure relative parameters such as the atomic occupation, lattice parameter after Mn doped. Meanwhile, we are motivated to the special Mn doped behaviour effect on the magnetic properties such as the Curie temperature T_C, spontaneous magnetization (M_S), coercivity (H_C), the nature of the magnetic transition (first order or second order), the specific nature of any second order transition (3D Heisenberg model, 3D Ising model, or mean-field theory), the magnetic entropy change $-\Delta S$, the heat capacity C_p, the Debye temperature (θ_D), the electronic density of states at the Fermi level E_F ($N(E_F)$), etc. To further clarify the structure and magnetic structure below and above the magnetic state transition, high resolution synchrotron and neutron measurements were performed. By the way, another series $Tb_{1-x}Y_xCo_2Mn_x$ (x = 0, 0.1, and 0.2) was detailed studied combined in the thesis.

1.4 Thesis Outline

This research thesis is divided into 7 chapters, including the Introduction, and is organised as

follows:

Chapter 1: Introduce the research background, a statement of the problems of the magnetic refrigeration, the objectives and scope of the research.

Chapter 2: A critical literature review of the fundamental theory of the magnetocaloric effect and the crucial relative researches on magnetocaloric materials.

Chapter 3: Investigation on $TbCo_2Mn_x$ (x = 0, 0.1, 0.2, and 0.3) compounds.

Chapter 4: Investigation on $HoCo_2Mn_x$ (x = 0, 0.2, 0.5, 0.7, and 1.0) compounds.

Chapter 5: Investigation on $DyCo_2Mn_x$ (x= 0.1, 0.2, 0.4, 0.6, and 1.0) compounds.

Chapter 6: Investigation on $Tb_{1-x}Y_xCo_2Mn_x$ (x = 0, 0.1, and 0.2) compounds.

Chapter 7: Conclusions and Outlook, followed by a list of references.

CHAPTER 2 LITERATURE REVIEW

2.1 Introduction

The magnetocaloric effect (MCE) was first discovered by Warburg in 1881.[16] It was only in 1918, however, that Weiss and Picard first described the physical principles of the MCE phenomenon,[17] leading to the first application of the MCE by Debye in 1926.[18] Then, Giauque invented magnetoresistance (MR) cycling to reach lower temperature before liquid helium was used in1927,[19] followed by the work of Giaque and MacDougal, who reached a record low 250 mK temperature, surpassing 1 K for the first time in 1933. Apart from the super-low-temperature cooling, room temperature magnetic refrigeration was realized by Brow in 1976 using Gd material in the varying magnetic field created by superconducting magnets.[20] After that, Pecharsky and Gschneidner discovered many materials with a significant magnetocaloric effect (MCE) at room temperature in 1997,[21] and the Astronautics Cooperation used permanent magnets to create the external magnetic field instead of the superconducting magnets in 2001.[22] All these developments make magnetocaloric effect materials promising as substitutes for conventional refrigeration materials, to create a much more efficient and environmentally-friendly cooling technology. Many scientists, researchers, and companies have devoted many efforts to the magnetocaloric effect research area since then. Many publications and patents focused on magnetocaloric materials have also appeared.[23]

2.2 Foundational Theories for Magnetocaloric Effect (MCE) Research

2.2.1 Thermodynamics of the MCE Theory[27]

The magnetocaloric effect (MCE) generates due to the magnetocaloric materials` thermal response with the magnetic field varying. It is an intrinsic magnetic property for all the magnetocaloric materials. To quantify the MCE, reversible temperature change ΔT_{ad} in the refrigeration material during the magnetic field change is used if in an adiabatic process； or the reversible magnetic entropy change ΔS_m if in the isothermal process. Actually, the most important property is the total entropy, which is consist of magnetic entropy ΔS_m,[24] lattice entropy ΔS_r[25] and electronic entropy of the free electron ΔS_e, expressed as following:[26]

$$S_T(H, T) = S_m(H, T) + S_r(T) + S_e(T) \quad (2.1)$$

Here the lattice and electronic entropy only depend on the temperature independent on the magnetic field. While the magnetic entropy depends on both magnetic field and temperature variation.

According to the second law of thermodynamics, the internal energy change can be expressed as following:

$$dU = TdS - pdV + \mu_0 HdM \quad (2.2)$$

where p is the pressure, V is the volume of the sample, μ_0 is the magnetic permeability of the vacuum, H is the intensity of the magnetic field, and M is the magnetic momentum. When the system's volume keeps still, $dV = 0$, Eq. 2.2 can be expressed as:

$$dU = TdS + \mu_0 HdM \quad (2.3)$$

Eq. 2.3 can be evolved as:

$$dU = TdS + \mu_0 Hd\sigma \quad (2.4)$$

where σ is the magnetic momentum per unit of mass. So the total specific entropy change can be formulated as:

$$ds = \left(\frac{\partial s}{\partial T}\right)_H dT + \left(\frac{\partial s}{\partial T}\right)_H dH \quad (2.5)$$

The specific heat c of the sample under constant state or a parameter x can be defined as:

$$c_x = \left(\frac{\delta q}{dT}\right)_x \quad (2.6)$$

$$ds = \frac{\delta q}{dT} \quad (2.7)$$

Where the Eq. 2.7 defines as second law. Combining the Eq. (2.6) and Eq. (2.7), the specific heat during isobaric process for a constant magnetic field (c_{pH}) can be expressed as:

$$c_{pH} = T\left(\frac{\partial s}{\partial T}\right)_H \quad (2.8)$$

According to Maxwell relation, the magnetic field dependent entropy can be expressed in terms of magnetisation as following:

$$(\frac{\partial s}{\partial H})_T = \mu_0(\frac{\partial \sigma}{\partial T})_H \quad (2.9)$$

Through putting Eqs. 2.8 and 2.9 into Eq. 2.5, the entropy expression is deduced out:

$$ds = \left(\frac{c_{pH}}{T}\right) dT + \mu_0(\frac{\partial s}{\partial T})dH \quad (2.10)$$

The reversible temperature change ΔT_{ad} in adiabatic process can be obtained:

$$\Delta T_{ad} = -\mu_0 \int_{H_0}^{H_1} (\frac{T}{c_{pH}}) (\frac{\partial \sigma}{\partial T})_H dH \quad (2.11)$$

Eq. 2.11 is just the quantified MCE in the adiabatic process.

As for the isothermal process, the total entropy change Δ_S is equal to the magnetic entropy change Δ_{Sm} and $dT = 0$. Refer to Eq. 2.10, the entropy change Δ_S can be calculated out as:

$$\Delta s = \Delta s_m = -\mu_0 \int_{H_0}^{H_1} (\frac{\partial \sigma}{\partial T})dH \quad (2.12)$$

And the reversible change of the temperature can be expressed as:

$$\Delta T_{ad} = -\mu_0 \int_{H_0}^{H_1} (\frac{\partial \sigma}{\partial T})_H dH. \quad (2.13)$$

As a usual research method, the magnetic entropy change can be obtained according to the isothermal magnetisation versus magnetic field (*M*-*H*) curves with a range of temperatures.

2.2.2 Banerjee Criterion

Referring to all the magnetocaloric material research, the element doping behaviour usually leads to the magnetic transition from first order to second order. The condition also happened in our research in $TbCo_2Mn_x$, $HoCo_2Mn_x$ and $DyCo_2Mn_x$ compounds. Traditionally, to distinguish the first order and second order, Banerjee Criterion[28] was used, based on Arrott plot(*H/M* versus M^2) construction.[29] According to the Banerjee Criterion, an "S"shape negative slope of the Arrott plot near the magnetic phase transition temperature symbolizes a first order transition while an "L" shape with positive slope of the Arrott plots means a second magnetic transition . However, the criterion is not always suitable in some magnetic materials such as $DyCo_2$, $NdCo_2$ and $PrCo_2$ compounds.[30] And as Banerjee Criterion figured out, the slope will increase continuously with the temperature increasing, which is not

observed in most experiments.[30, 31, 32, 33] Although with limitation, the Banerjee Criterion is widely used and credible in most condition. So here we simply introduce how the Banerjee Criterion was derived out after the Arrott plot had been constructed.

2.2.2.1 Arrott Plot

The normal second-order transition can be described by the free-energy density as following: [28]

$$f = f_0 + \frac{A}{2(\tau-\tau_c)}m^2 + \frac{B}{4m^4} - hm \tag{2.14}$$

Where *A*, *B* are positive constant and $\tau = \frac{T}{T_C}$, T_C is the proportional to the exchange interaction and corresponds, τ_c is the critical reduced temperature. When $\frac{\partial f}{\partial m} = 0$, the equation of the state can be expressed as:

$$\frac{h}{m} = A(\tau - \tau_c)m + Bm^2 = g(x) \tag{2.15}$$

Where $g(x) = A(\tau - \tau_c)m + Bx$. In this way, *h/m* as a function of m^2 is a simple linear behavior where the slope is associated to the fourth-order term in the free energy density and the intercept of these lines ($m^2 = 0$) is temperature dependent with positive value when $\tau > \tau_c$ and negative otherwise. So this is a simple way to obtain the value of the critical temperature T_C. Furthermore, the curves of *h/m* versus m^2 are strongly affected by the magnetic moment *M* and volume *V*. In this case, the temperature and field dependent high and low magnetic state ($\frac{\partial f}{\partial m} = 0$) can be expressed as:[28]

$$\frac{h}{m} = 2(1 - \alpha V_0 \frac{\partial T_c}{\partial V})(\tau - \tau_1)m + \frac{2}{3(\tau-\tau_2)m^2} + \frac{6}{15}\tau m^4. \tag{2.16}$$

Where α is the constant thermal expansion coefficient, V_0 is the critical volume, T_0 is the initial Curie temperature without the volume magnetization coupling. So come to this step, the Arrott plot *H/M* versus M^2 are finally constructed.

2.2.2.2 Banerjee Criterion

According to Eq. 2.16, when $\tau_2 > \tau_1$ there is a negative slope in the Arrott plot indicating first order transition as figured out by Banerjee.[28] Except to the law to decide the first order transition, Banerjee also made a second important observation: the value of the negative

slope will increase with the temperature increasing. The observation is also deduced out from Eq. 2.16, when $m^2 \to 0$, the slope of the Arrott plot can be expressed as:

$$s = \frac{\partial(h/m)}{\partial(m^2)} = 2/3(\tau - \tau_2) \tag{2.17}$$

it changes the sign at $\tau - \tau_2 > \tau_c > \tau^*$.[35] The theory is in accordance well with the MnAs data.[1] However, as discussed above, it is not found in most other experiments.[30, 31, 34, 35]

2.2.3 Critical Exponents Analysis

After distinguish the first order and second order transition, we still do the further investigation on the nature of the second order transitions belonging to 3D Heisenberg model, 3D Ising model or Mean-field theory. So critical exponents analysis (β, γ and δ) was used as a professional research method using various techniques such as Kouvel-Fisher plot, Arrott-Noaks plot and critical isotherm analysis. Here a list of the standard critical exponents[36, 37, 38] was shown as following: 3D Heisenberg model: β = 0.365, γ = 1.386 and δ = 4.8; 3D Ising model: β = 0.325, γ = 1.241 and δ = 4.82; Mean-field theory: β = 0.5, γ = 1.0 and δ = 3.0.

Using our experimental data, the experimental critical exponents β, γ and δ can be calculated out according to scaling hypothesis based on the following equations: [39]

$$M_S(0,T) = M_0(-\varepsilon)^{\beta},\ \varepsilon < 0 \tag{2.18}$$

$$\chi_0^{-1}(0,T) = (h_0/M_0)(\varepsilon)^{\gamma} \tag{2.19}$$

$$M(H, T_C) = A_0(H)^{1/\delta} \tag{2.20}$$

Where $\varepsilon = (T\text{-}T_C)/T_C$, M_S and χ_0^{-1} is initial susceptibility below and above T_C, M (H) is magnetic moment at T_C. M_0, h_0/M_0 and A_0 are constants of the critical amplitudes. M_S (T) and $\chi_0^{-1}(T)$ can be derived from the high field data of the Arrott plot: the positive values of x intercept and y intercept of the dash line are the values of $\chi_0^{-1}(T)$ and M_S^2 (T) respectively the red dash lines shown in Fig. 2.1.(As an example, Figs. 2.1-2.4 are all from our experimental data, which have not been published yet)

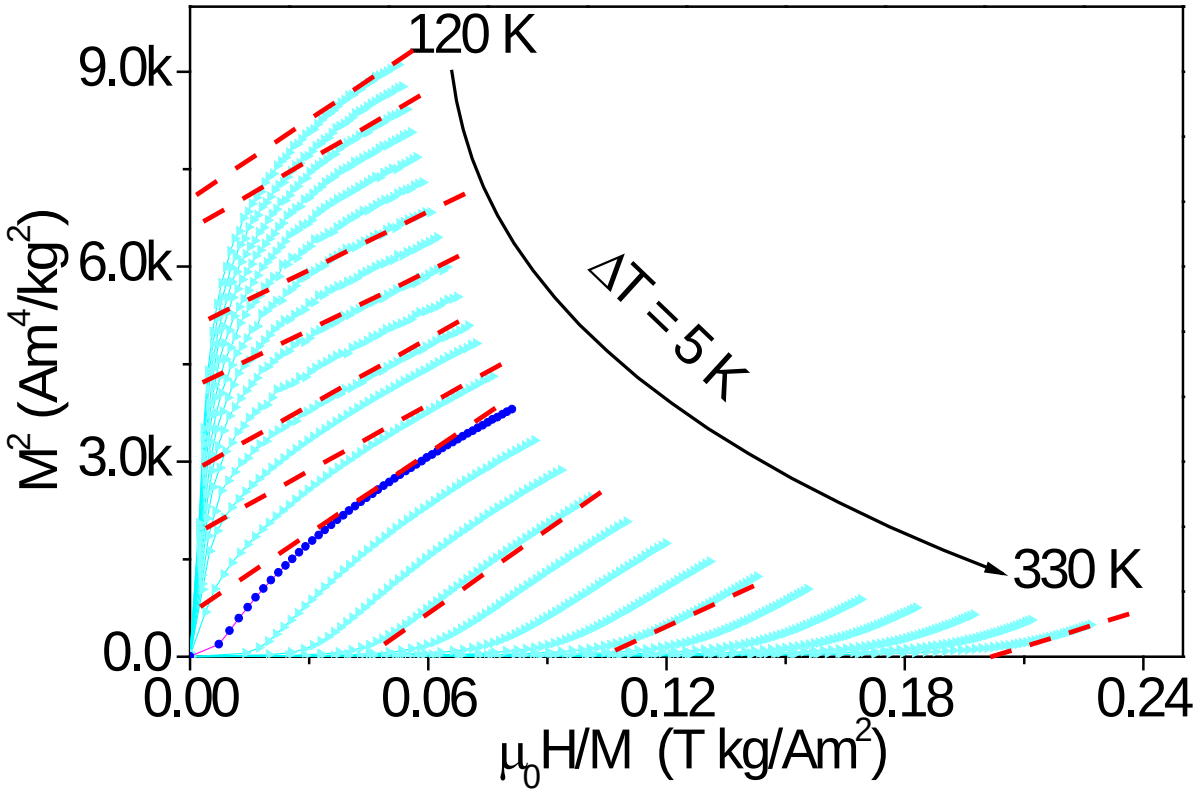

Fig. 2.1. Arrott plots: isotherms of M^2 vs H/M for decreasing field at different temperatures around T_c . The magenta curves are the Arrott plots at high field near the Curie temperature.

As for the transition belongs or approaches to the mean-field theory, it is figured out that the standard Arrott plots linear fitting lines at high field (the blue dash line) near T_C will be parallel and typically the line nearest T_C will pass through the origin[41,42] as shown in Fig. 2.1. And the critical exponent β and γ can be calculated out directly according to the Arrott plot using no-linear fitting according to Eqs. 2.18 and 2.19 as shown in Fig. 2.2(a). And we can see from Fig. 2.2 as an example from our experiment data, the obtained data is β = 0.561± 0.002 and γ = 1.055± 0.068, which are all very near the Mean-field critical exponents.

Except to the no-linear fitting method, Kouvel-Fisher method with linear fitting can be used to obtain the more precise value of β and γ according to the counterpart Eqs. 2.21 and 2.22 deduced respectively from Eqs. 2.18 and 2.19: [40]

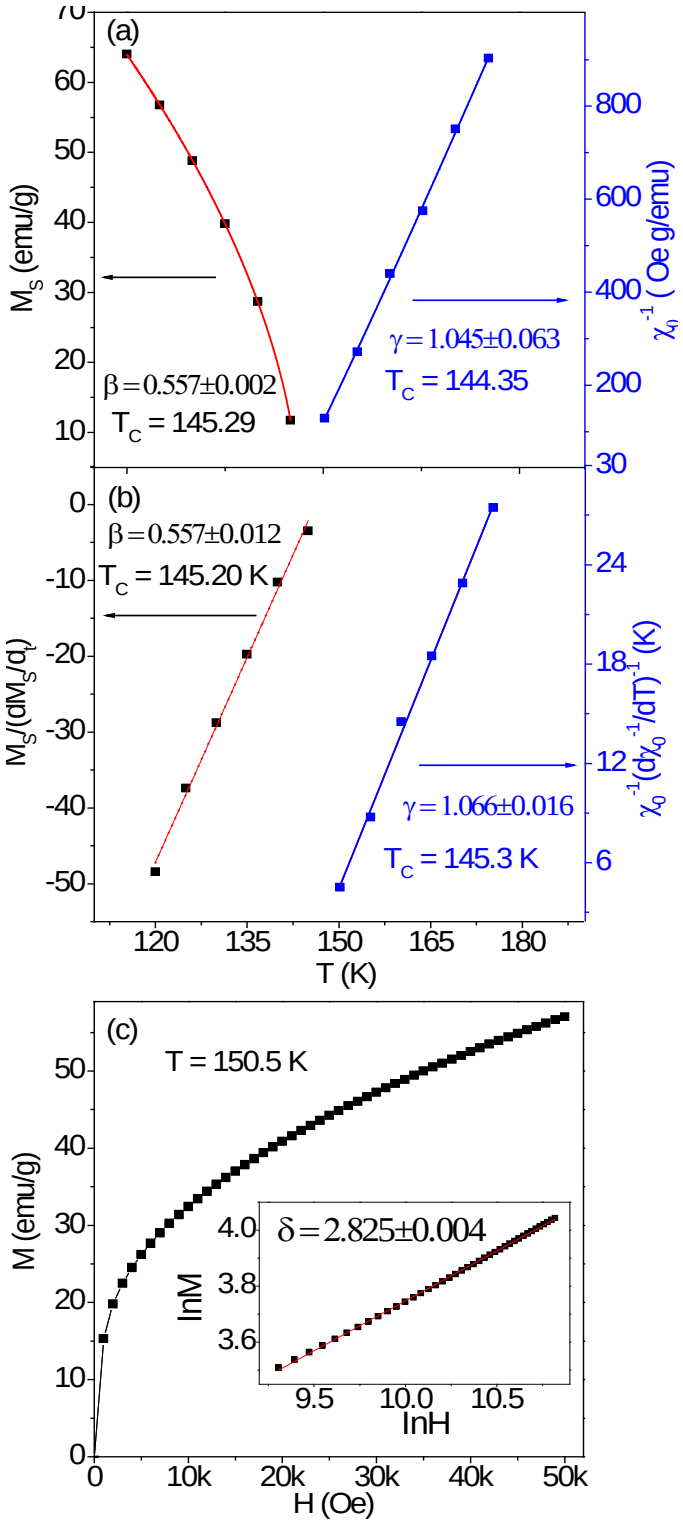

Fig. 2.2. (a) Temperature dependent spontaneous magnetization $M_S(0, T)$ and inverse initial susceptibility $\chi_0^{-1}(0, T)$ with no-linear fitting(colour solid lines) according to Eqs. 2.18 and 2.19. (b) Using Kouvel-Fisher method linear fitting according to Eqs. 2.21 and 2.22 to obtain the value of β and γ. (c) Critical isotherm of M vs H near T_C. Inset exhibits the same on log-

log scale at high field with the linear fitting according to Eq. 2.20 shown as the red straight line, whose reciprocal value of slope is the value of δ.

$$\frac{M_S(T)}{dM_S(T)/dT} = \frac{T-T_C}{\beta} \tag{2.21}$$

$$\frac{\chi_0^{-1}(T)}{d\chi_0^{-1}(T)/dT} = \frac{T-T_C}{\gamma} \tag{2.22}$$

The values of $1/\beta$, $1/\gamma$ and T_C can be obtained by linear fitting of the $M_S/(dM_S(T)/dT)$ and $\chi_0^{-1}(T)/\ (d\chi_0^{-1}(T)/dT)$ shown in Fig. 2.2(b).

Finally using Eq. 2.20 the value of δ can be obtained as shown in Fig. 2.2(c). Meanwhile, based on value of β and γ, the value of δ can also be deduced out according to the Widom scaling relation:[43]

$$\delta = 1 + \gamma/\beta \tag{2.23}$$

However, as for the transition is not belong to Mean-filed theory, Arrott plot can not be used directly to obtain the critical exponents. So modified Arrott plot should be used on the basis of Arrott-Noaks equation:[44]

$$\left(\frac{H}{M}\right)^{1/\gamma} = \frac{a(T-T_C)}{T_C} + bM^{1/\beta} \tag{2.24}$$

Where a and b is constants. To obtain the optimum fitting values of β and γ, self-consistent method[45, 46] was used: the first values of $M_S(T)$ and $\chi_0^{-1}(T)$ were derived from the high field standard Arrott plot the same as discussed Fig. 2.1. And then the calculated β and γ were used to build the new modified Arrott plot. The two processed were repeated several times until iteration converge to get the optimum final values when the high filed modified Arrott plot line near the Curei temperature come across the origin as shown in 2.3(b). The detailed process can be seen in Fig. 2.3(a) and 2.3(b).

Finally, to confirm all our calculated critical exponent and T_C are accurate and reliable, the value of β and γ were put into universal curves function $M\ (H, \varepsilon)$ according to the scaling hypothesis:[47]

$$M\ (H, \varepsilon) = \varepsilon^{\beta} f \pm H/\varepsilon^{\beta+\gamma} \tag{2.25}$$

Which collapses into two branches respectively for temperatures above and below T_C as shown in Fig. 2.4. It means that all our calculations of exponent and T_C are exact and unambiguous.

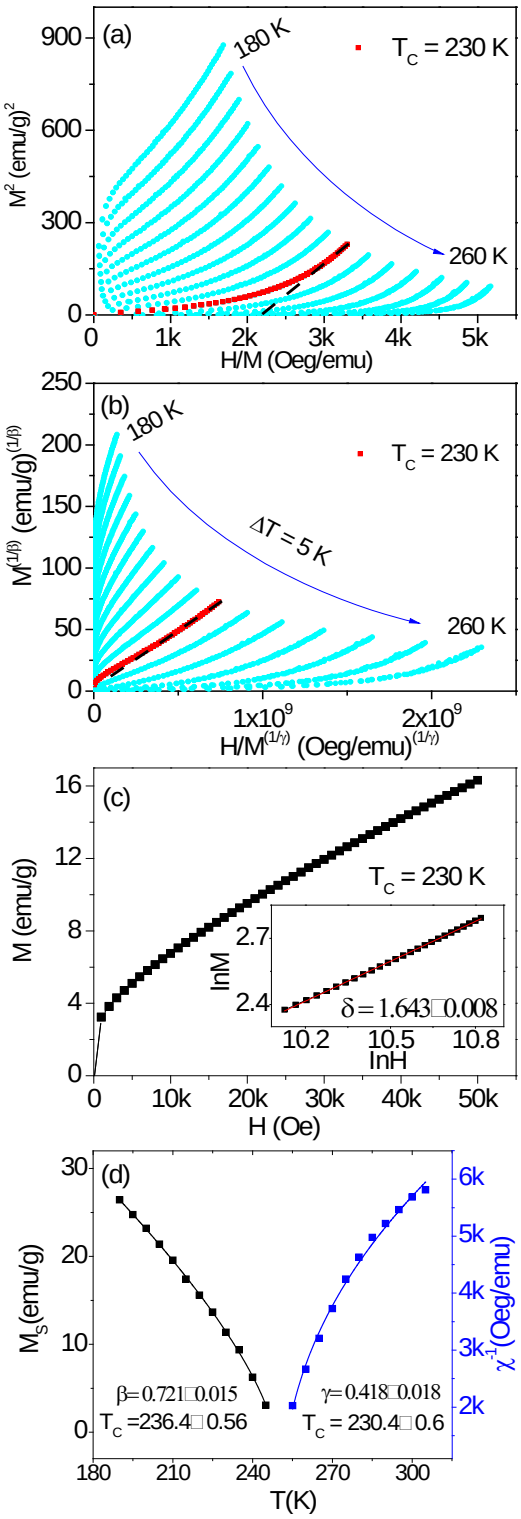

Fig. 2.3. (a) Standard Arrott and (b) Modified Arrott plot respective near T_C. The black dash lines are the high field data. (c) Critical isotherm of M vs H near T_C. Inset exhibits the same

on log-log scale at high field with the linear fitting according to Eq. 2.20 shown as the red straight line, whose reciprocal value of slope is the value of δ. (d) The final temperature dependent spontaneous magnetization $M_S(0, T)$ and inverse initial susceptibility $\chi_0^{-1}(0, T)$ with no-linear fitting (solid lines) according to Eqs. 2.18 and 2.19.

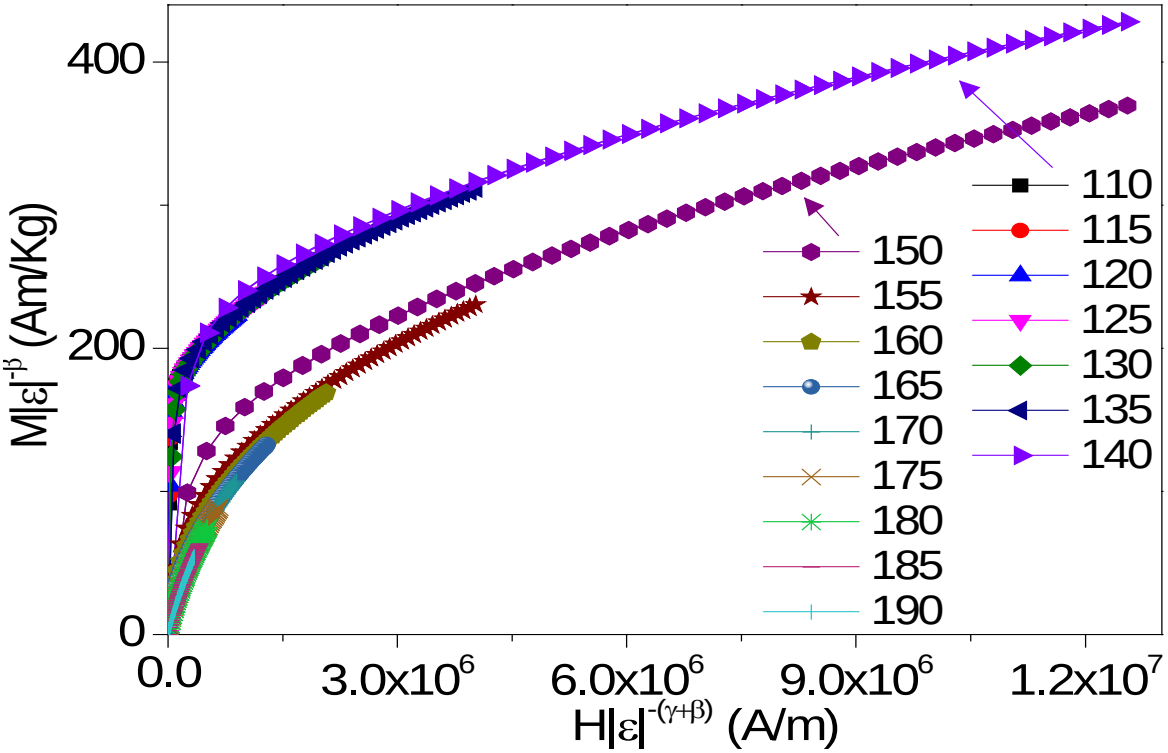

Fig. 2.4. Scaled magnetization above and below T_C according to the scale hypothesis Eq. 2.25, which indicates all the experimental M (H) curves near T_C will collapse into two branches for the temperatures above and below T_C respectively.

2.2.4 Heat Capacity

The heat capacity $C(T)$ of a metallic magnetic material can be described as the contributions from phonons, electrons and magnon:[48]

$$C(T) = C_{ph}(T)+C_{el}(T)+C_m(T) \tag{2.26}$$

where C_{ph}, C_{el} and C_m are the lattice, electronic, and magnetic contributions respectively. At low temperature with the absence of a magnetic phase transition, the heat capacity can be expressed as:[48]

$$C(T)/T = \gamma + \beta T^2 \tag{2.27}$$

Where γ and β is the electronic and phonon heat capacity coefficients respectively. Then the electronic density of states N (E_F) at the Fermi surface can be obtained by the formula:[48]

$$\gamma = \frac{k^2{}_B * \pi^2}{3} N(E_F) \tag{2.28}$$

where k_B is the Boltzmann constant. Likewise, the Debye temperature θ_D can also be deduced out by: [49]

$$\beta = \frac{12 * \pi^4 * R}{5 * \theta^3{}_D} \cong \frac{1944 * n}{\theta^3{}_D} \tag{2.29}$$

where R is the universal gas constant and n is the number of atoms.

2.3 Experimental Techniques and Measurements

2.3.1 Sample Preparation

All the $TbCo_2Mn_x$ (x = 0, 0.1, 0.2, and 0.3), $HoCo_2Mn_x$ (x = 0, 0.2, 0.5, 0.7, and 1.0), $DyCo_2Mn_x$ (x = 0.1, 0.2, 0.4, 0.6, and 1.0) and $Tb_{1-x}Y_xMn_2Ge_x$ (x = 0, 0.1, and 0.2) series compounds were prepared through standard arc melting constituent elements of 99.9 % purity under argon atmosphere, in a HV(high vacuum) Arc Melting and Single-roller Melt Spinning System. And then the prepared ingots were wrapped by tantalum foil and sealed in quartz glass tubes in vacuum circumstance to anneal: the samples were heated near 1173 K dwelling for 7 days in muffle furnace and then quenched into ice water. Then all the Mn doped samples were characterised to be pure and isostructure to parent ingots, by x-ray powder diffraction at room temperature using a PANalytical diffractometer with Cu $K\alpha$ radiation.

2.3.2 Magnetic and Heat Capacity Measurements

The dc magnetic measurements and specific heat capacity measurement were performed respectively using a Quantum Design 9 T and 14 T physical properties measurement system (PPMS). To precisely decide the magnetic transition temperature, magnetic moment versus temperature (*M*-*T*) in a magnetic field 100 Oe during the zero field cooling and field cooling were obtained. Besides, 5 K hysteresis loop and isothermal magnetization versus magnetic field (*M*-*H*) curves at a range of temperatures were obtained.

2.3.3 Neutron and Synchrotron Powder Diffraction Pattern Measurements

High resolution synchrotron and neutron diffraction pattern measurements were performed to further clarify the delicate crystal and magnetic structure transitions during the magnetic-state transition. For the neutron diffraction pattern measurements, we used high-resolution powder diffractometer collected at Echidna of OPAL facility and high-intensity powder diffractometer Wombat at the OPAL facility (Lucas Height, Australia) with a neutron wavelength of 1.6220 Å and 2.4138 Å respectively. And for the synchrotron measurement, the wavelength of 0.6884 Å or 0.7746 Å pattern was chosen in Powder diffraction pattern Unit (Synchrotron measurement centre, Melbourne). To analyse the synchrotron and neutron diffraction pattern, refinements were carried out with the Fullprof package.

2.4 Relevant Research on the RM_2Mn_x (R = rare earth, M = Ni or Co, $0 \leqslant x$) Series Compounds

2.4.1 Pioneering Research on the Pseudo-Ternary Magnetocaloric Compound $DyNi_2Mn$[50]

In 2002 Wang et al. were the first to synthesise pure $DyNi_2Mn$ compound, which is isostructural to $DyNi_2$ with the cubic $MgCu_2$-type structure, although the ratio of the initial *R* and *M* components is 1:3, as shown in Fig. 2.5. To clarify the novel structure, refinement was done. It was found that the structure of $DyNi_2Mn$ compound keeps a cubic structure with Fd3m space group with the lattice parameter a = 7.1406(2) Å. The atomic occupation rate was deduced out to be 73.8% for Dy, 21.4% for Mn, and 4.8% unoccupied at 8a sites. Furthermore, it is important that the narrow domain wall effect on the magnetohistory, the atomic exchange interaction effect on the Curie temperature, and the anisotropy effect on the coercivity were determined as a reference for later work on RT_2Mn_x (R = rare earth, T = transition metal, $x > 0$) series materials. So, this was pioneering research on the pseudo-ternary RT_2Mn compound, which inspired the synthesis and study of many similar magnetocaloric materials.

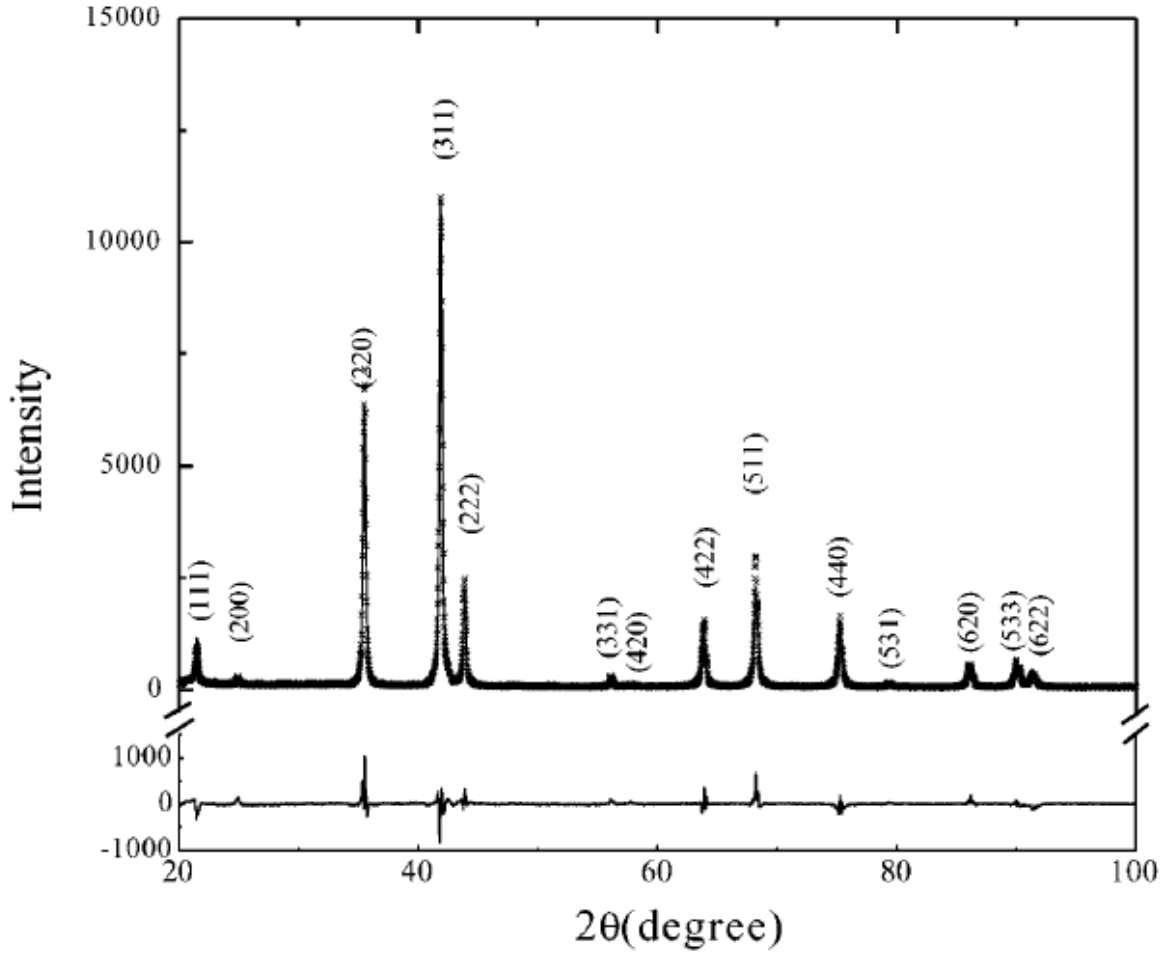

Fig. 2.5. Rietveld analysis of the XRD pattern of $DyNi_2Mn$. The black crosses are the experimental XRD data, and the red lines represent the Rietveld refined pattern. The difference between the experimental and calculated patterns is shown at the bottom by the blue solid curve. The vertical bars indicate the positions of allowed Bragg peaks.[50]

2.4.2 Extending Research on RNi_2Mn Compounds (R = Tb, Dy, Ho, and Er)[51]

Based on the pioneering research on $DyNi_2Mn$ in 2002, Wang et al. extended the research to other novel RNi_2Mn (R = Tb, Dy, Ho, and Er) compounds in 2006, which, as expected, are isostructure to RNi_2 with the cubic $MgCu_2$-type structure.[50] In this work, the magnetohistory effect was mainly further extended compared with the previous work in **Section 2.4.1**: the magnetic domains are random in the orientation after the zero field cooling (ZFC) process. So, when a small magnetic field is added at 5 K, the magnetisation is small due to the big coercivity arising from the anisotropy. When the temperature increases, the coercivity

decreases, leading to an increase in the magnetisation. In the case of the field cooling process, the domains are oriented along the applied magnetic field, with the result that the initial value of the magnetisation is much bigger than in the ZFC process. So, it was clarified that the irreversible magnetisation is due to the coercivity caused by domain orientation in the ZFC or FC processes, respectively. The magnetohistory effect is a general phenomenon that is displayed in all our current materials. Meanwhile, this work compared the magnetic properties such as the Curie temperature or coercivity among all the other RNi_2Mn compounds, as shown in Table 2.1. So, we can see that this extension of the work is not only an exploration for more RT_2Mn_x materials, but also a base study to clarify the foundational magnetic principles behind various magnetism phenomena.

Table 2.1 Structural and magnetic parameters of RNi_2Mn, RNi_2, and RMn_2 compounds. (Note that the experimental error in the lattice parameters of the RNi_2Mn is ±0.001 Å.)[51]

Compounds	a (Å)	V (Å^3)	T_C (K)
$TbNi_2Mn$	7.185	370.9	131
$DyNi_2Mn$	7.140	364.1	94
$HoNi_2Mn$	7.135	363.4	75
$ErNi_2Mn$	7.126	361.9	50
$TbNi_2$	7.16	367.1	37.5
$DyNi_2$	7.142	364.3	22
$HoNi_2$	7.136	363.4	15
$ErNi_2$	7.125	361.6	7
$TbMn_2$	7.635	445.1	54
$DyMn_2$	7.602	439.3	35
$HoMn_2$	7.592	437.6	24
$ErMn_2$	7.500	421.9	15

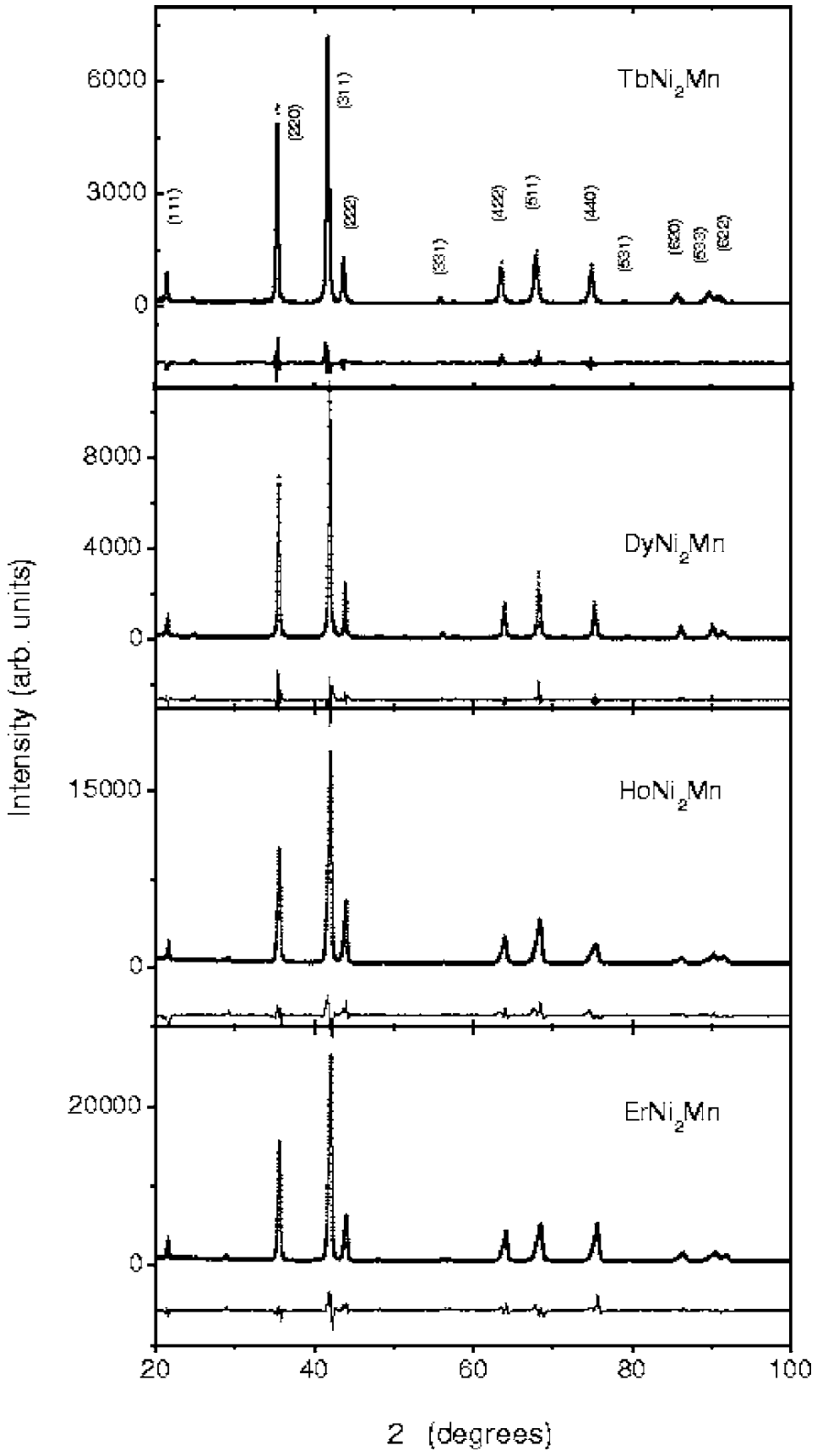

Fig. 2.6. XRD patterns of the RNi_2Mn compounds (R = Tb, Dy, Ho, and Er). Crosses indicate the observed data. The calculated profile obtained from Rietveld analysis corresponds to the

continuous curve in each panel. The lower profile is the difference between the observed and calculated intensities at each angle step.[51]

2.4.3 Research on the $GdNi_2Mn_x$ ($0 \leqslant x \leqslant 0.6$) alloys.[52]

In 2013， E. G. Gerasimov et al. systematic studied the off-stoichiometric $GdNi_2Mn_x$ ($0 \leqslant x \leqslant 0.6$) alloys. Unlike the above work by Wang's group, this work was focused on the Mn content variation and its effects on the magnetic properties. As expected, they found that the compounds were pure and isostructure to $GdNi_2$ with a cubic structure of the $MgCu_2$-type when crystallized with $0 < x < 0.4$. As the x value increases, the $PuNi_3$-type phase appears. The value of Curie temperature increases as the x value increases from 80 K for $GdNi_2$ to 190 K for the $GdNi_2Mn_{0.4}$. The spontaneous magnetization at 4 K decreases with increasing x value, meaning that there is a ferrimagnetic structure after Mn doping. In particular, the atomic magnetic moment (Gd, Ni, and Mn) are discussed in detail, assuming collinear antiparallel ordering of the magnetic moments between Gd and Mn and Ni, respectively, which is in good agreement with previous work.[53, 54, 55] The magnetic entropy change, $-\Delta S$, as an important factor for magnetic refrigeration application was also discussed in this work. The magnetic entropy changes $-\Delta S$ as a function of temperature for $GdNi_2Mn_{0.3}$ and $GdNi_2Mn_{0.4}$ were obtained according to the temperature dependent magnetization at various magnetic fields from 0.05 T to 9 T. A huge operation temperature in the $-\Delta S$ versus T curves was observed in both $GdNi_2Mn_{0.3}$ and $GdNi_2Mn_{0.4}$. This is also important for practical magnetic refrigeration applications. Finally, according to the mean-field theory, the value of the isothermal entropy change ΔS versus the $(\mu_0 \Delta H/T_C)^{2/3}$ curve was obtained, which indicated that both the magnetic transitions of $GdNi_2Mn_{0.3}$ and $GdNi_2Mn_{0.4}$ compounds belong to the second order with long-range magnetic exchange interaction. This mean-field theory analysis for the second order transition inspired us to conduct a specific study on the nature of the second order using more professional critical exponents analysis techniques such as Kouvel-Fisher plots, Arrott-Noaks plots, and critical isotherm analysis, as discussed in **Section 3.3.4**, **Section 4.3.3**, **and Section 5.3.3** respectively. So, based on a large amount of previous foundational research, this paper did pioneering research on the effect of the Mn content variation on the magnetic properties, with attention paid to more physical properties, such as the atomic magnetic moments, the magnetic entropy change, and the nature of the second order transition.

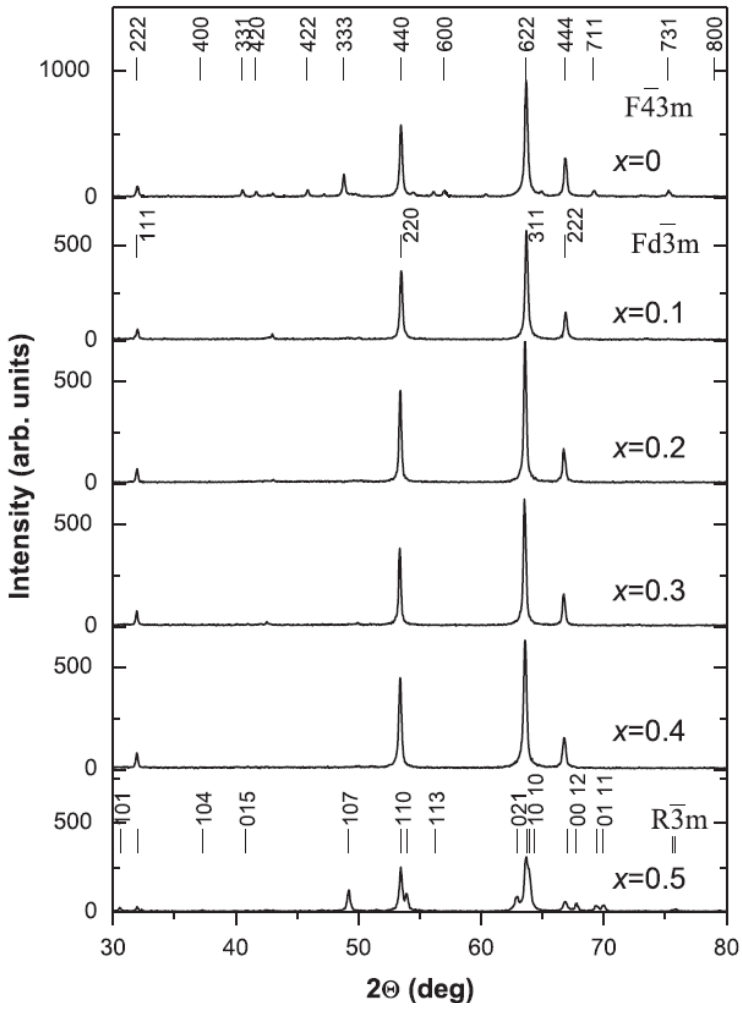

Fig. 2.7. X-ray diffraction patterns of $GdNi_2Mn_x$ alloys. Short lines show reflections of the C15 ($F\bar{4}3m$) superstructure for the alloy with x = 0, the C15 ($Fd\bar{3}m$) structure for the alloy with x = 0.1, and the rhombohedral $PuNi_3$-type (R3m) structure for the alloy with x = 0.5.[52]

2.4.4 Extending Research on RCo_2Mn Compounds (R = Ho and Er)[54]

In 2014, Bibekananda Maji et al. started to investigate the RCo_2Mn compounds with R = Ho and Er. Similarly, X-ray characterization was done for the first time, as shown in Fig. 2.7. The lattice parameters and the relative magnetic parameters were obtained as shown in Table 2.2. A big coercivity, $H_C \approx 1$ T was observed for $ErCo_2Mn$. Specially, the nomagnetic contribution was depicted based on the Debye theory using the θ_D = 250 K as shown in Fig. 2.8, where we can see that electronic and lattice(the solid red lines) mainly contribute to the

total heat capacity (black open circle), with a little gap for the magnetic contribution for both $HoCo_2Mn$ and $ErCo_2Mn$.

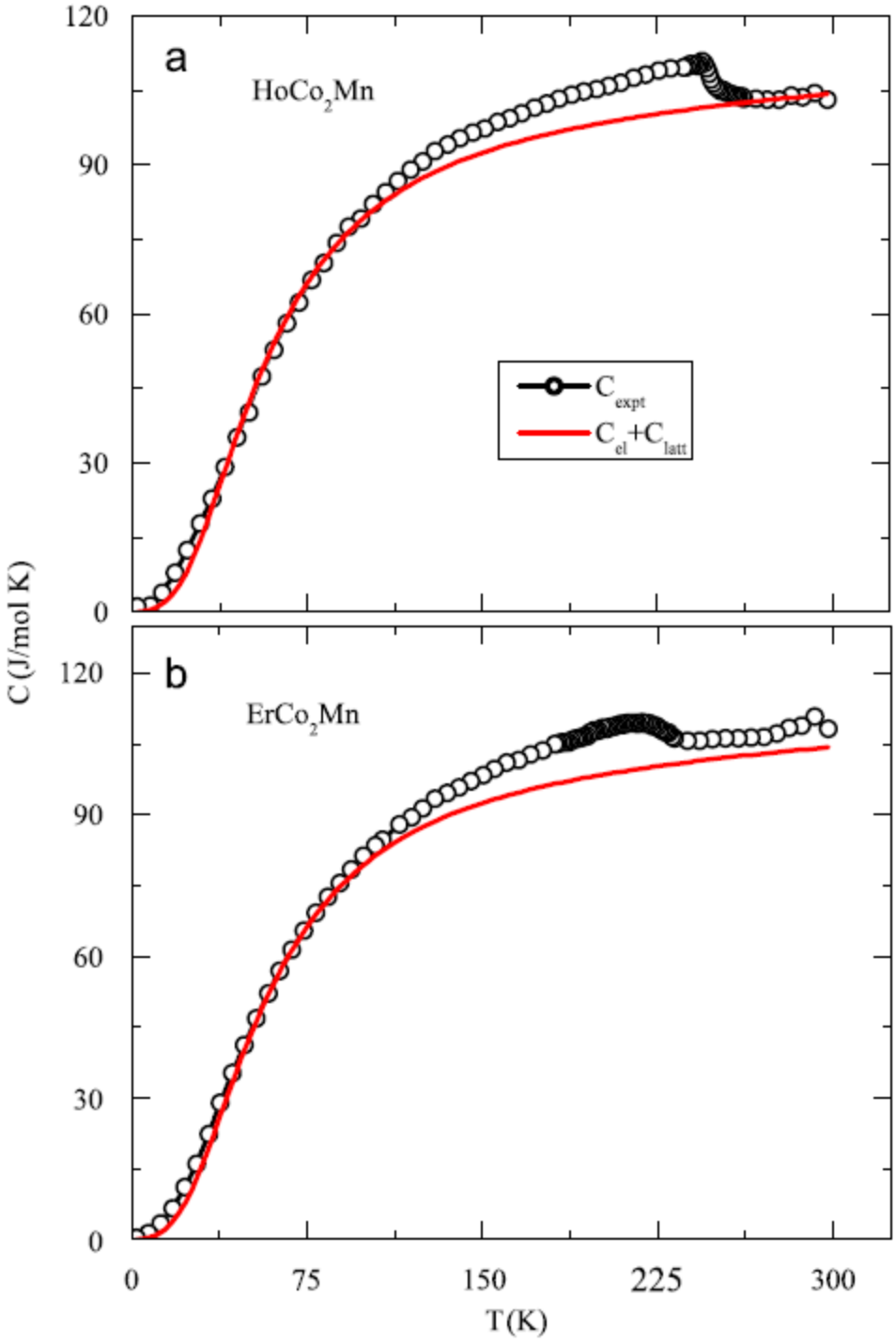

Fig. 2.8 The heat capacity for (a) $HoCo_2Mn$ and (b) $ErCo_2Mn$ as a function of temperature in zero field (open circles), while the solid lines symbolize the sum of the calculated electronic and lattice contributions (C_{el}+C_{latt}).[54]

Table 2.2 Lattice parameters, Curie temperatures, and the saturation moments of RCo_2Mn compounds (R = Ho and Er).[54]

Compound	a (Å)	T_C (K)	M_S (μ_B/f.u.)
$HoCo_2Mn$	7.166	248	6.6
$ErCo_2Mn$	7.132	222	5.2
$HoCo_2$	7.151	78	7.8
$ErCo_2$	7.153	35	6.0

2.4.5 Research on the $ErCo_2Mn_x$ ($0 \leqslant x \leqslant 1.4$) Alloys.[56]

In 2016, E. G. Gerasimov et al. extended their research on the $ErCo_2Mn_x$ ($0 \leq x \leq 1.4$) series compounds including those with x values greater than 1.0**.** A similar investigation method to that in **Section 2.4.3** ($GdNi_2Mn_x$) was used for all the $ErCo_2Mn_x$ ($0 \leq x \leq 1.4$) samples. The XRD patterns show that the alloys with $x \leq 0.8$ are pure phase with the $MgCu_2$-type structure, while Th_6Mn_{23}-type phase grows when $0.8 < x \leq 1.0$. For $0 \leq x \leq 0.6$, the exchange interactions were enhanced with more Mn doping, causing the Curie temperature to increase from 35 K for x = 0.0 to 212 K for x = 0.6. Meanwhile, the nature of the magnetic transition transforms from first order for $ErCo_2$ to second order for all the Mn doped samples. The total entropy change $-\Delta S$ was also calculated from the heat capacity measurements, and the magnetic entropy change $-\Delta S_m$ deduced from the isothermal magnetisation is specially discussed: for all the second order transitions, there was no obvious peak found in the $-\Delta S_m$ versus T curve near each Curie temperature, while the corresponding turning point near the Curie temperature is displayed in the $-\Delta S$ versus T curves, which means that the second transition is affected by the total entropy change. In addition, through the heat capacity measurements, the Debye temperature, $\theta_D \approx 240$ K for $ErCo_2Mn_x$ compounds was reported as a reference for other similar materials.

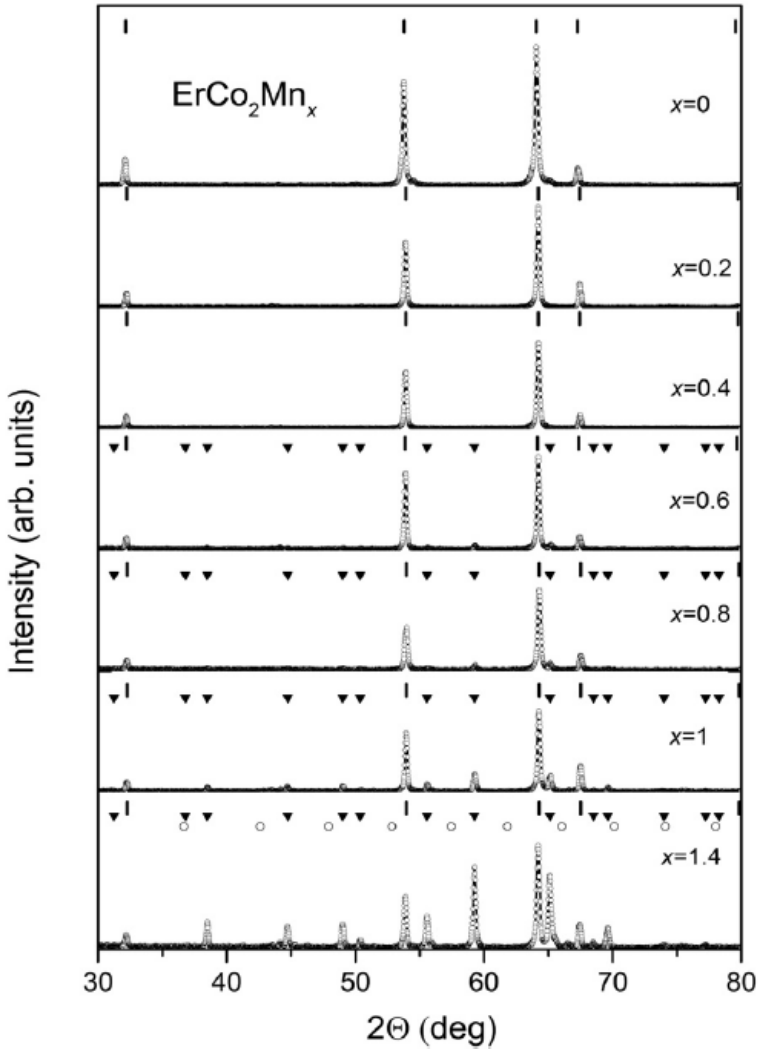

Fig. 2.9. X-ray diffraction patterns of the $ErCo_2Mn_x$ alloys with different *x*. Bragg peak positions are indicated by the markers for the $MgCu_2$-type structure (vertical bars), the Th_6Mn_{23}-type structure (solid triangles), and Mn (open circles).[56]

2.4.6 The pressure effect on the crystal and magnetic structures of $Tb_{1-x}Y_xMn_2Ge_2$ ($0 \leqslant x \leqslant 0.6$) Alloys[55]

As is well known, the crystal structure of the RT_2X_2 (T = transition metal, X = Mn, Ge) series is the body-centred tetragonal $ThCr_2Si_2$-type, with atomic layers stacked in the sequence of -R-X-T-X-R- along the *c*-axis. The rare earth elements normally exhibit a large magnetic moment with a smaller moment for transition metals and Mn, Ge. The magnetic state is complex, however, with respect to the various temperatures because both the intralayer and the adjacent interlayer Mn-Mn change interaction mainly depends on the intralayer Mn-Mn distance. Take $TbMn_2Ge_2$ as an example, it has antifrrroamgnetic structure below the Néel

temperature T_N =410 K: the Mn moments order antriferromagnetically with each other in the same Mn layer, while the ferromagnetic Mn sublayers align along c-axis in a sequence of + - +-. And below the Curie tempearature T_C = 95 K, it transforms into ferrimagnetic structure: the Tb moments couple ferromagnetically with each other, ordering antiferromagnetically with the Mn moments. For the RT_2X_2 (T = transition metal, X = Mn, Ge) series materials, a various interesting magnetic properties display through tuning the distance of the intralayer Mn-Mn. In 1998, L. Morellon et al discussed the high pressure effect on the magnetic state transition, According to the measurement result in Fig. 2.9, we can see the value of transition temperature (from ferromagnetism to antiferromagnetism) decreases linearly with the pressure increasing, $dT_{F\text{-}AF}/dp$ = -2.9±0.2 K/kbar, which is an important reference for our discussion on "Y Doping in $Tb_{1-x}Y_xMn_2Ge_2$-Chemical Pressure Effect" in **Section 6.3.3**. And here it estimated 1.2% decrease of the interatomic distance will totally block the magnetic transition from ferromagnetism to antiferromagnetism.

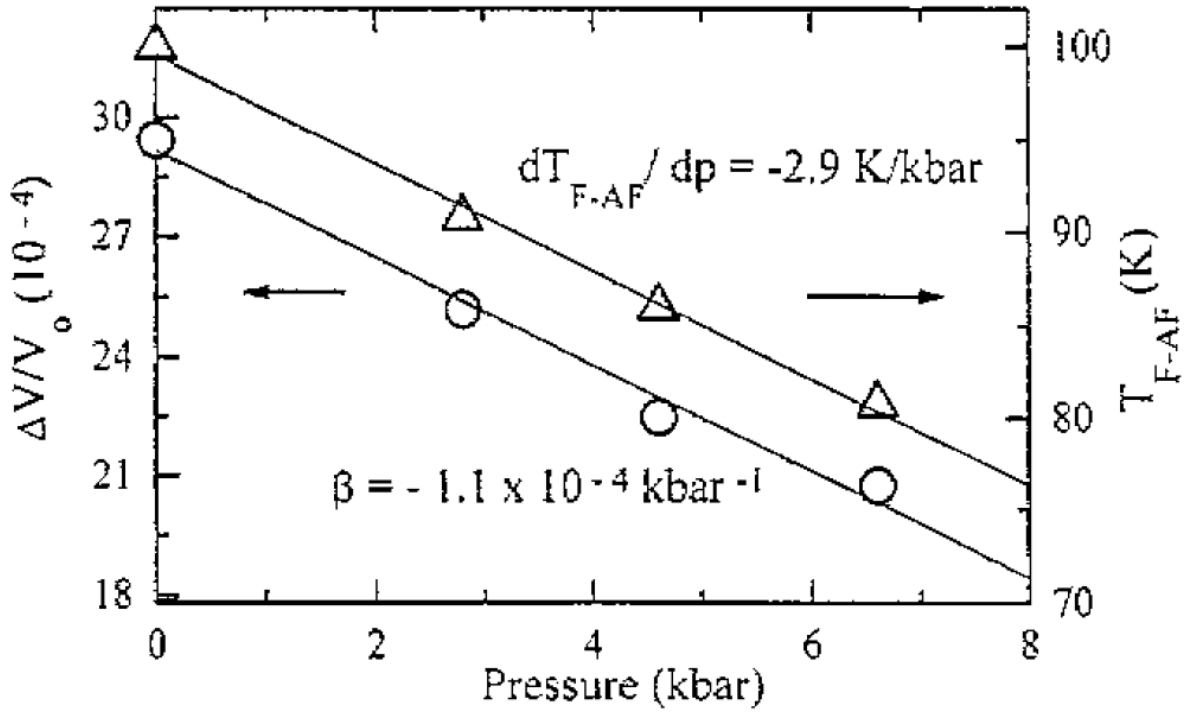

Fig. 2.10 The transition temperature $T_{F\text{-}AF}$ (from ferromagnetism to antiferromagnetism) and the volume anomaly ω as functions of various pressures.[55]

CHAPTER 3 INVESTIGATION OF $TbCo_2Mn_x$ (x = 0, 0.1, 0.2, 0.3) COMPOUNDS

3.1. Introduction

The cubic Laves phases RT_2 (R = rare earth, T = transition metal) series magnetic materials were studied intensively because of their unique electronic and magnetic structures, which lead to many novel physical properties such as giant magneto-caloric effect, magnetoresisitance,[55, 56] and hydrogen storage capacity[57]. Typical Laves phases include the cubic $C_{15}(MgCu_2)$, hexagonal $C_{14}(MgZn_2)$, and hexagonal $C_{36}(MgNi_2)$.[57] They are ideal magnetic systems in which to study the effect of atomic occupation and f-d orbital electron localization on magnetic and electronic properties.[58]

Wang et al.[59, 51] discovered novel RNi_2Mn (R = Tb, Dy, Ho, Er) compounds, which crystallize in the cubic $MgCu_2$-type structure ($Fd\bar{3}m$, space group). Recently, it was reported that RCo_2Mn with R = Ho and Er also crystallize in the cubic $MgCu_2$-type structure.[55] It was found that the introduction of Mn into RT_2 (T is 3d or 4d transition metal) compounds led to a significant modification of magnetic properties such as the Curie temperature[2, 4, 7-11] magnetic entropy change,[58] saturation moment,[2] the nature of the magnetic transition[58] and so on. It is accepted that the Curie temperature can be raised significantly with Mn doping or addition due to the enhanced 3d transition-metal ion interactions.[59, 51] It is of interest that the RT_2Mn compounds are isostructural to RT_2 with the $MgCu_2$-type structure, although the ratio of the R to T is 1:3,[52, 54, 55, 58, 60-62] and the Mn was observed to occupy both the R and T sites. All the above modified magnetic properties and crystal structure inspired more work on related series materials such as $ErCo_2Mn$,[55] $HoNi_2Mn$,[62] $DyNi_2Mn$[59, 51] and $TbNi_2Mn$.[51, 60]

However, there is little systematic research specifically on the RT_2Mn_x (x up to 1.0) series since the crystal structure is unstable when significant Mn is added. For example, $GdNi_2Mn_x$ ($0 \leq x \leq 0.6$) alloys were successfully synthesized and characterised by XRD. When the Mn concentration increases to a certain level ($x \geq 0.35$), a second phase with rhombohedral $PuNi_3$-type (R3m) structure starts to form.[10] Recently, the investigation on $ErCo_2Mn_x$ (x = 0.0 to 0.8) also found that when $x \leq 0.8$, the alloys are almost single phase ($MgCu_2$-type Laves-phase structure), while a second phase with cubic Th_6Mn_{23}-type structure appears for larger x values.[54]

Previous investigations of the $TbCo_2$ compound indicated that $TbCo_2$ has the $MgCu_2$-type structure and shows paramagnetic behaviour at room temperature. When cooled to lower temperature, it exhibits a rhombohedral distortion around the Curie temperature T_C (= 240 K) (from paramagnetism to ferrimagnetism). The Tb–Co coupling is antiferromagnetic with a large moment in Tb site and almost equal Co moments at the 3b and 9e sites. The nature of the magnetic transition (PM to FM) in $TbCo_2$ was indicated to be second order according to Arrott plots.[62, 63-66] However, relying solely on Arrott plots to decide the nature of transition is not always prudent.[67, 32]

In this thesis, we present a detailed investigation on structural and magnetic properties of $TbCo_2Mn_x$ (x = 0.0, 0.1, 0.2 and 0.3) compounds using variable temperature neutron diffraction and synchrotron x-ray diffraction. Analysis of the temperature dependent neutron diffraction data shows that the nature of magnetic transition in $TbCo_2$ is first order with a sharp volume change near T_C. However, this first order magnetic phase transition for x = 0 changes to second order after the introduction of Mn. We plotted master curves of the magnetic entropy changes[68, 69] to clearly identify the transformation from first order to second order, as well as detailed refinement of diffraction data near the magnetic phase transition temperature to verify the change in crystal structure. Finally, the critical behaviour around T_C was investigated using the Kouvel-Fisher technique to precisely analyse the nature of the second order transitions for all the $TbCo_2Mn_x$ (x = 0.1, 0.2 and 0.3) compounds.

3.2. Experimental Techniques

The polycrystalline $TbCo_2Mn_x$ compounds with x = 0.0, 0.1, 0.2 and 0.3 were prepared by arc melting the constituent elements of 99.9 % purity under argon atmosphere. The values of x referred to hereafter are these nominal ratios of the starting mixture materials. Noting 3% additional Mn was added initially to compensate non-proportionate losses of Mn during arc-melting and annealing process. We have evaluated the loss by measuring the weight of materials before and after preparation; the error in x is less than 3%. The prepared ingots were wrapped in tantalum foil and sealed in quartz glass tubes under vacuum and annealed at 1173 K for 7 days and then quenched into ice water. All the samples were checked with x-ray powder diffraction at room temperature using a PANalytical diffractometer with CuKα radiation. The dc magnetisation measurements and heat capacity were performed using a

Quantum Design physical properties measurement system (PPMS) from 5 K to 340 K, and from 2 K to 320 K, respectively. The magnetic and structural transitions were investigated via neutron diffraction experiments at the Wombat (high-intensity powder diffractometer) at the OPAL facility (Lucas Height, Australia) with a neutron wavelength of 2.4139 Å from 5 K to 400 K. The crystal structure transitions were also examined by the synchrotron x-ray powder diffraction at the Australian Synchrotron using a wavelength of 0.6884 Å at temperatures from 90 K to 400 K.

3.3. Results and Discussion

3.3.1 Crystal structure at Room Temperature

Room temperature XRD was performed to check that all the samples are single phase. The Rietveld refinement confirmed that $TbCo_2Mn_{0.1}$, $TbCo_2Mn_{0.2}$ and $TbCo_2Mn_{0.3}$ all have the same crystal structure as the parent compound $TbCo_2$ (cubic with $Fd\bar{3}m$ space group shown in Fig. 3.1(a)). We have adopted the similar refinement approach as described in references [51, 59] to assume that Mn atoms are located at both Tb and Co sites with some vacancies at the Tb site in order to make $TbCo_2Mn_x$ able to adopt the $TbCo_2$ structure. Here taking $TbCo_2Mn_{0.1}$ as an example, we have rewritten $TbCo_2Mn_{0.1}$ as $(Tb_{1+v}Mn_y)(Co_2Mn_{0.1-y})$ and let $(1+v+y)/(2+0.1-y)$ equal to 1:2 (v represent the number vacancy at the Tb site and y stands for the number of Mn atoms occupying Co sites). In the case of the $TbCo_2Mn_x$ compounds it has been found that the best refinement has been obtained when $v = 0.0$ which indicates that no vacancy exists in reality for $TbCo_2Mn_x$ compounds. The refinements of these XRD patterns at room temperature are shown in Fig. 3.1(c), Fig. 3.1(d), Fig. 3.1(e) and Fig. 3.1(f), respectively.

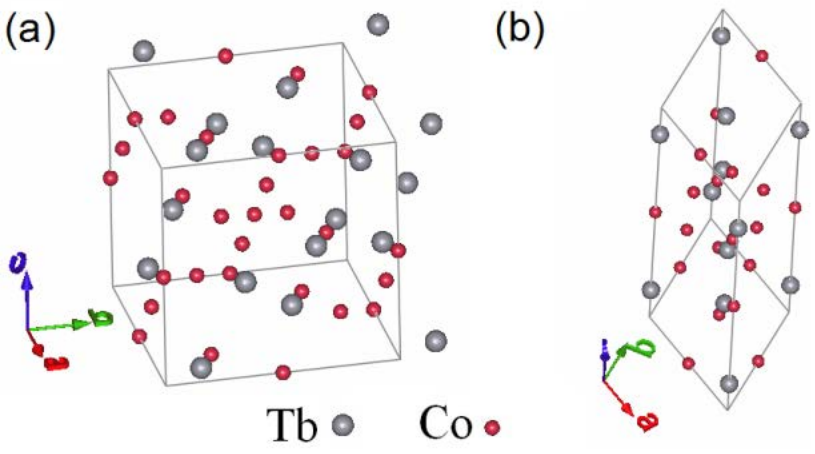

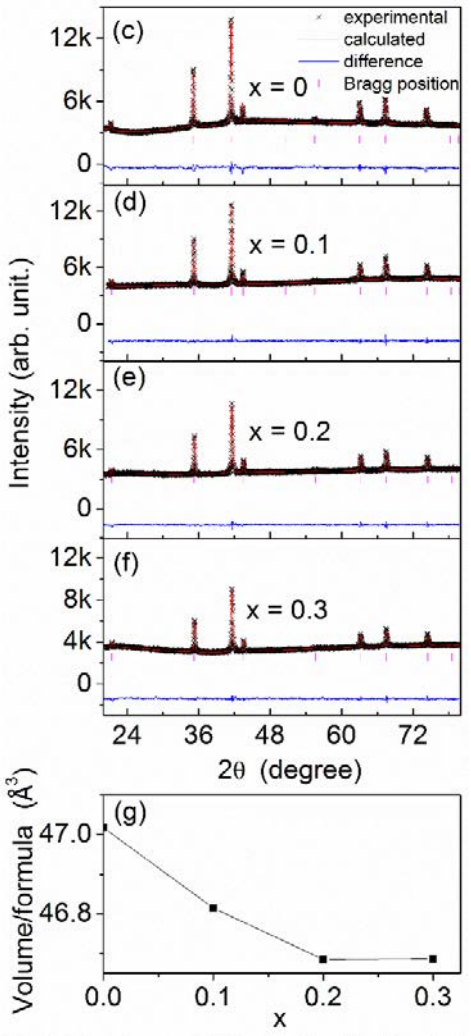

Fig. 3.1. The crystal structures with space group of (a) $Fd\bar{3}m$ and (b) $R\bar{3}m$.(c), (d,) (e) and (f) are room temperature XRD refinements of $TbCo_2Mn_x$ (x = 0, 0.1, 0.2 and 0.3), respectively.(g) is the x value dependence of the volume per chemical formula.

The dependence of unit cell volume on the x value is shown in Fig. 3.1 (g), from which it can be noted that the volume per chemical formula decreases from 47.02 Å^3 to 46.68 Å^3 as the x value increases from 0 to 0.3, which can be understand due to the enhanced atomic forces with more Mn atoms added.

3.2.2 Magnetic Phase Transition

The magnetization versus temperature curves for $TbCo_2Mn_x$ (x = 0, 0.1, 0.2 and 0.3) compounds are shown in Fig. 3.2(a), measured with field cooling and at B = 0.01 T. The Curie temperature T_C is defined as the point where the slope of the temperature dependent

dM/dT curve is a minimum. It can be seen clearly that with the x value increasing from 0 to 0.3, T_C increases from 230 K to 284 K, 320 K and 332 K, respectively, (see inset of Fig. 3.2 (a)). The increase in T_C with Mn concentration x can be ascribed to enhanced exchange interactions between the 3d transition-metals.[61, 70]

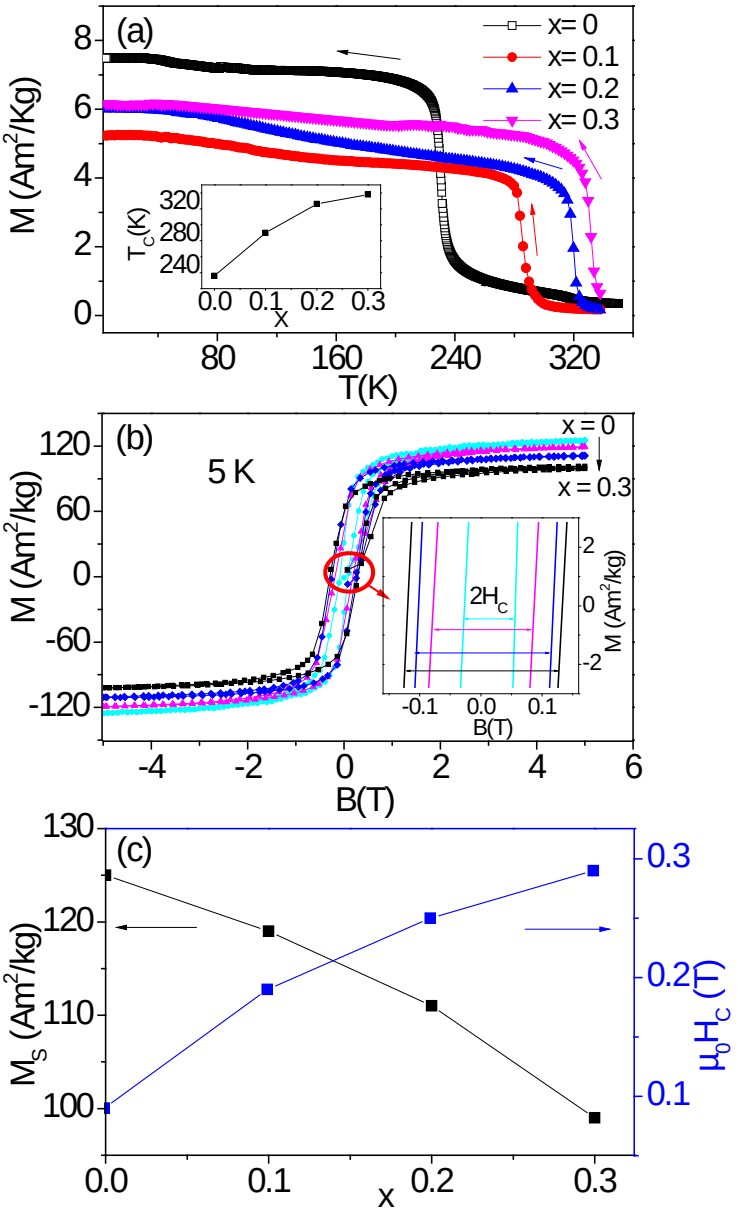

Fig. 3.2. (a) Temperature dependent magnetization with field cooling (FC at the field of B = 0.01 T for $TbCo_2Mn_x$ (x = 0, 0.1, 0.2 and 0.3). The inset shows the x value dependence of the Curie temperature T_C. (b) Hysteresis loops at 5K for $TbCo_2Mn_x$ (x = 0, 0.1, 0.2 and 0.3). The inset is an enlargement for small B and M values to show the coercivity H_C. (c) Plot of the dependence of saturation magnetization M_S and coercivity $\mu_0 H_C$ versus x at 5 K.

The magnetic hysteresis loops at 5 K for each sample are shown in Fig. 3.2(b). We can see directly that as Mn content increases the saturation magnetic moment M_S decreases with increasing x while the coercivity H_C increases. From Fig. 3.2(c), it can be seen that the M_S value decreases from 125 Am^2/kg to 119 Am^2/kg, 111Am^2/kg and 99 Am^2/kg with the value of x increasing from 0 to 0.1, 0.2 and 0.3, respectively. It is well accepted in rare earth transition metal compounds that heavy rare earth moments couple antiferromagnetically with transition metal moments. If we assume here therefore that the Tb-sublattice moments also couple in an antiparallel fashion and are constant with increasing Mn moment, than the decrease in *Ms* with increasing x indicates that Mn atoms carry a magnetic moment in line with that concluded by the neutron diffraction analysis in **Section 3.3.6**. Meanwhile, the coercive field H_C increases from 0.09 T to 0.19 T, 0.25 T and 0.29 T with x value increasing from 0 to 0.1, 0.2 and 0.3, respectively. The increased coercive fields suggest that the crystal symmetry of the compound was reduced, anisotropy being enhanced after more Mn was introduced.

3.3.3. Magnetocaloric Effect

The field dependencies of magnetization near Curie temperature are shown in Figs. 3.3(a), 3(b), 3(c) and 3(d) for x = 0, 0.1, 0.2, and 0.3, respectively. Consistent with the *M-T* curves of Fig. 3.2(a), the magnetic FM-PM transition also can be detected in the magnetization-field (*M-H*) isotherms in Figs. 3.3(a), 3(b), 3(c) and 3(d): with the temperature increasing near the Curie temperature, the *M-H* isotherms transform from curved hysteresis loops to overlapping straight lines. Moreover, it can be seen that the hysteresis loss for all the series samples (x= 0, 0.1, 0.2 and 0.3) are all negligible. The latter being desirable for increased magnetic refrigeration working efficiency for the materials.[61]

To determine the magnetic entropy changes ΔS_M from the isothermal magnetization curves, the standard Maxwell relationship was used as following:

$$\Delta S_M(T, B) = \int_0^{B^{max}} \left(\frac{\partial M(B,T)}{\partial T}\right)_B dB. \quad (3.1)$$

The calculated temperature dependent magnetic entropy changes for the $TbCo_2Mn_x$ (x = 0, 0.1, 0.2 and 0.3) samples for both ramp up and ramp down with field changes from 0 T to 5 T are shown in Figs. 3.4(a), 4(b), 4(c) and 4(d).

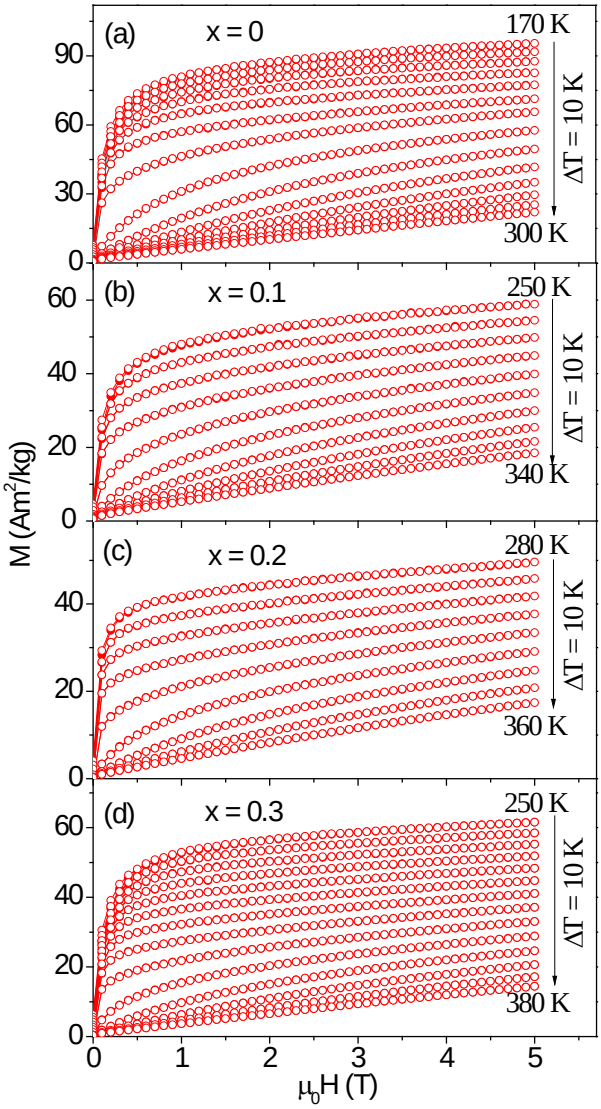

Fig. 3.3.Isothermal magnetization versus magnetic field at various temperatures in both increasing field (full red symbol) and decreasing field sweeps (hollow red symbols) for (a) $TbCo_2$, (b) $TbCo_2Mn_{0.1}$, (c) $TbCo_2Mn_{0.2}$ and (d) $TbCo_2Mn_{0.3}$.

From Fig. 3.4, it can be seen that for each sample there is a peak of magnetic entropy change $-\Delta S^{max}$ near the Curie temperature for each magnetic field change (0 T to 5 T) associated with the magnetic transition from the paramagnetic to the ferromagnetic state. Comparing the peak values, $TbCo_2$ has the largest $-\Delta S^{max}$ value of 6.0 J kg^{-1} K^{-1} compared with 3.2 J kg^{-1} K^{-1}, 2.83 J kg^{-1} K^{-1} and 2.74 J kg^{-1} K^{-1} for $TbCo_2Mn_{0.1}$, $TbCo_2Mn_{0.2}$ and $TbCo_2Mn_{0.3}$, respectively. The differences of the magnetic entropy for these compounds reflect that the type of magnetic transition has changed from the first order for $TbCo_2$ to second order for $TbCo_2Mn_x$ (x = 0.1, 0.2 and 0.3). Furthermore, as additional Mn is added the value of the

$-\Delta S^{max}$ decreases indicating that the contribution of structure entropy (i.e. magnetic volume effect) continues to weaken. The detailed volume change can be seen in the Fig. 3.11-14.

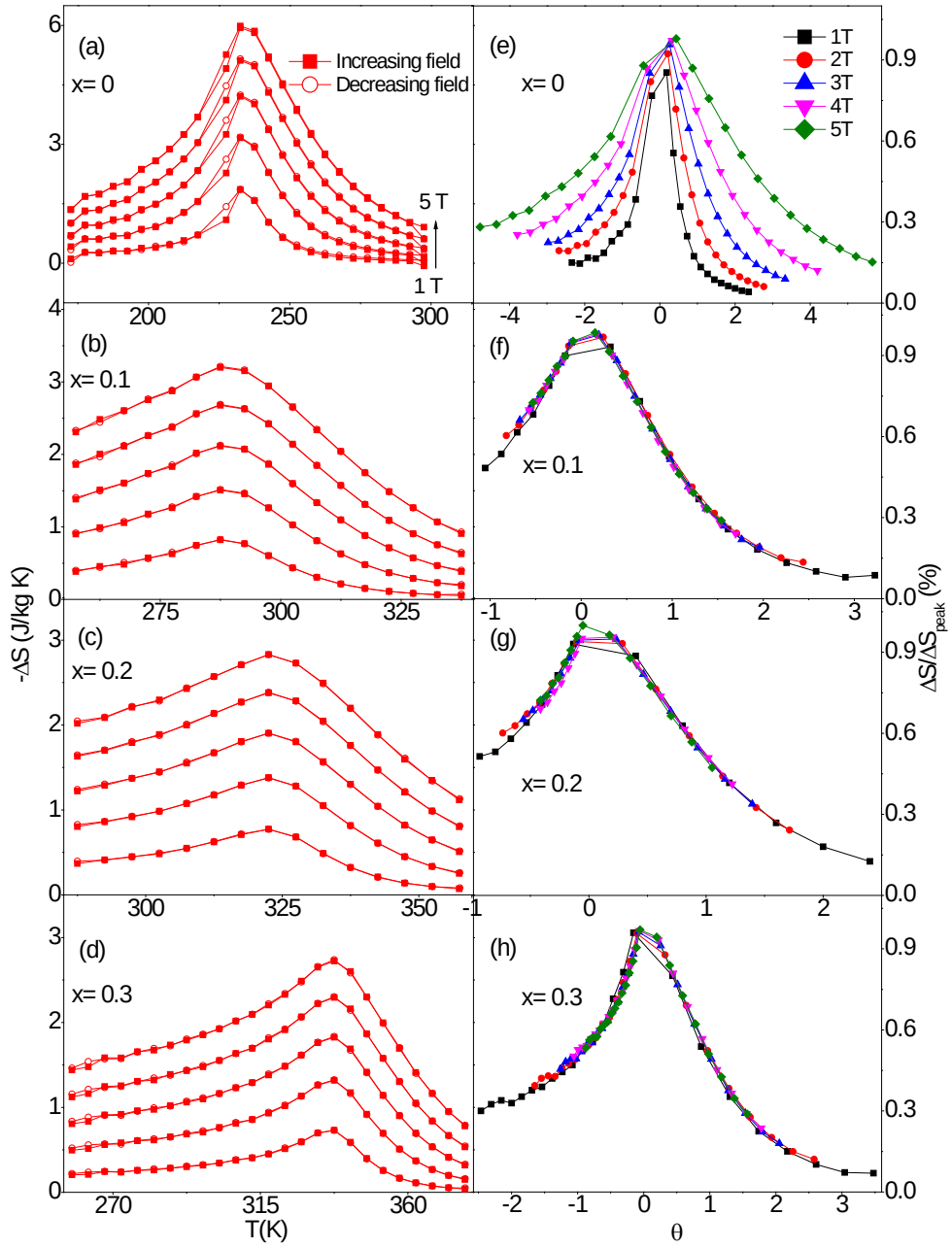

Fig. 3.4. The magnetic entropy changes for a range of temperatures and for magnetic field changes of $\mu_o \Delta H$ = 1 T to 5 T (the curves corresponding to each field change are denoted by the arrow which shows the increasing order bottom to top in (a)), of (a) $TbCo_2$ (b) $TbCo_2Mn_{0.1}$, (c) $TbCo_2Mn_{0.2}$ and (d) $TbCo_2Mn_{0.3}$. Increasing field data are represented by full red symbol and decreasing field data are open red symbols. The corresponding normalised magnetic entropy changes versus the rescaled temperature θ for (e), (f), (g) and (h) respectively.

Based on the magnetic entropy change in Fig. 3.4(a), (b), (c), (d)., normalisation of the magnetic entropy changes versus the rescaled temperature curves[68, 69] can be deduced out to decide the nature of the magnetic transition according, depicted as Fig. 3.4(e), (f), (g), (h). The normalisation of the magnetic entropy changes was defined as the value of $\Delta S/\Delta S_{peak}$ for each magnetic field change $\mu_0 \Delta H$. And the rescaled temperature θ can be specifically described as following:[68, 69]

$$\theta = \begin{cases} (T_{peak} - T)/(T_{r1} - T_{peak}) \\ (T - T_{peak})/(T_{r2} - T_{peak}) \end{cases} \quad (3.2)$$

where T_{r1} and T_{r2} is the temperature point where there is half maximum value of the peak magnetic entropy change respectively($T_{r2} < T_{peak} < T_{r1}$). From Figs 3.4 (e) to (h), it is very obvious that the entropy curves of the x = 0 sample are highly dispersed for different magnetic field changes, while all the Mn doped samples normalisation curves are overlapping for different fields. This is strong evidence suggesting the introduction of Mn does change the nature of the magnetic transition from the first order to the second order.

3.3.4 Critical Behaviour at the Magnetic Phase Transition Temperature

From Fig. 3.5(a) for $TbCo_2$, it can be found that a '*s*' shaped curve appears in the Arrott plot of M^2 *vs* B/M at 235 K, indicating that the magnetic transition of $TbCo_2$ is a first order transition. While for Fig. 3.5(b), 5(c) and 5(d), only positive slopes are present so it can be concluded that all of transitions in these compounds are second order. This observation implies that the addition of Mn into the $TbCo_2$ compound leads to the change of magnetic transition order from first order to second order. In order to get a better understanding of the critical behaviors around the transition temperatures in these compounds with second order transitions, we carried out an analysis of critical exponents using the Kouvel-Fisher (KF) method. The KF method can be described as following: [40]

$$\frac{M_S(T)}{dM_S(T)/dT} = \frac{T - T_C}{\beta} \quad (3.3)$$

$$\frac{\chi_0^{-1}(T)}{d\chi_0^{-1}(T)/dT} = \frac{T - T_C}{\gamma} \quad (3.4)$$

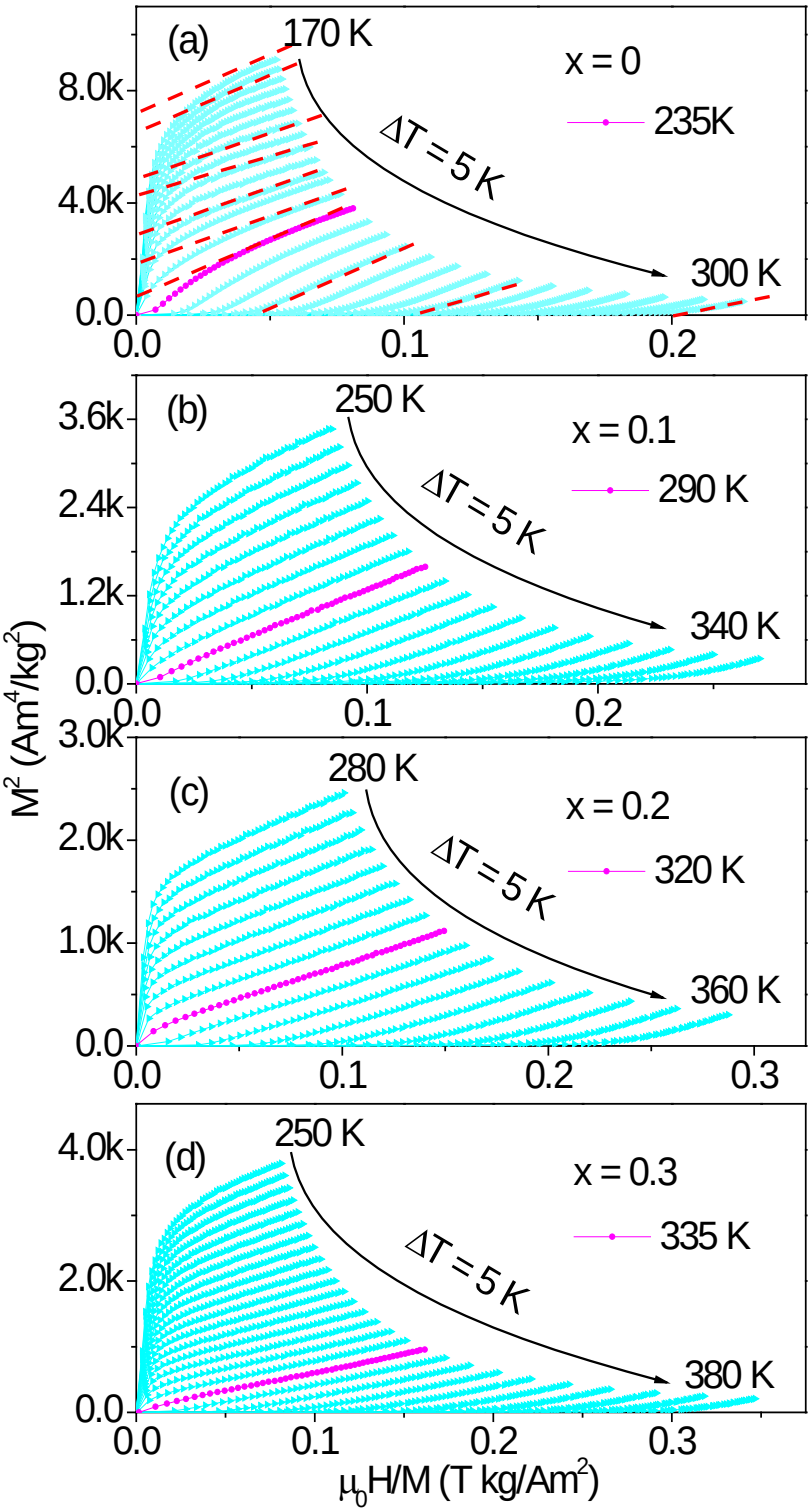

Fig. 3.5 Arrott plots: isotherms of M^2 vs H/M for decreasing field at different temperatures around T_c of (a) $TbCo_2$, (b) $TbCo_2Mn_{0.1}$, (c) $TbCo_2Mn_{0.2}$ and (d) $TbCo_2Mn_{0.3}$. The magenta curves are the Arrott plots near the Curie temperature for each sample.

where $M_S(T)$ *and* $\chi_0^{-1}(T)$ can be derived from the high field data of the Arrott plot as shown the dashed lines in Fig. 3.5(a)： the positive value of x-intercept and y-intercept of the dash

line is the value of $\chi_0^{-1}(T)$ and $M^2{}_s(T)$ respective.Based on the Eqs. 3.3 and 3.4, one can derive the corresponding values of slopes $1/\beta$, $1/\gamma$ and T_C using the linear fitting of the $M_S/(dM_S(T)/dT)$ and $\chi_0^{-1}(T)/\ (d\chi_0^{-1}(T)/dT)$. The fitted T_C values match well with the ones obtained from the M-T curves in Fig. 3.2(a). Moreover, for all the samples the derived values are close to $\beta = 0.5\ and\ \ \gamma = 1.0$ as shown in Fig. 3.6(a), Fig. 3.7(a) and Fig. 3.8(a).

The value of δ can be obtained by linear fitting of the higher field plots *ln(M)* vs *ln(B)* at T_C as shown in the insets in Fig. 3.6(b), Fig. 3.7(b) and Fig. 3.8(b), according to the following equation:[46]

$$M\,(B, T_c) = A_0\,(B)^{1/\delta} \tag{3.5}$$

where A_0 are the critical amplitudes. The values of δ for $TbCo_2Mn_{0.1}$, $TbCo_2Mn_{0.2}$ and $TbCo_2Mn_{0.3}$ are derived to be 3.07, 3.20, and 2.99 respectively.

In addition, the value of δ can also be deduced using the Widom scaling relation:[61, 70]

$$\delta\ =\ 1 + \gamma/\beta \tag{3.6}$$

All of the values derived for the critical exponents β, γ and δ have been listed in the Table 3.1. One can conclude that for all the second order transitions of these three samples, the values of β, γ and δ are close to 0.5, 1.0 and 3.0 within allowable experimental error, respectively. This indicates that the magnetic interactions in these compounds have long range order.

Finally, using the scaling theory in the critical region, the reliability of exponents β and γ can be confirmed by the equation following:[40]

$$M(H, \varepsilon) = \varepsilon^{\beta} f \pm (H/\varepsilon^{\beta+\gamma}) \tag{3.7}$$

Where ε is the reduced temperature $(T - T_C)/T_C$, f_+ and f_- are regular analytical functions above and below T_C respectively. The values of β and γ obtained through the Kouvel–Fisher method, shown in Fig. 3.6(a), Fig. 3.7(a) and Fig. 3.8(a), can then be used to obtain the M/ε^{β} versus $H/\varepsilon^{(\beta+\gamma)}$ curves as shown in Fig. 3.6(c), Fig. 3.7(c) and Fig. 3.8(c) wherein there are two universal curves, one for temperatures above T_C and the other one for temperatures below T_C. From the nature of the plots it can be concluded that all the calculated exponents β and γ and the corresponding T_C are reliable for each sample.

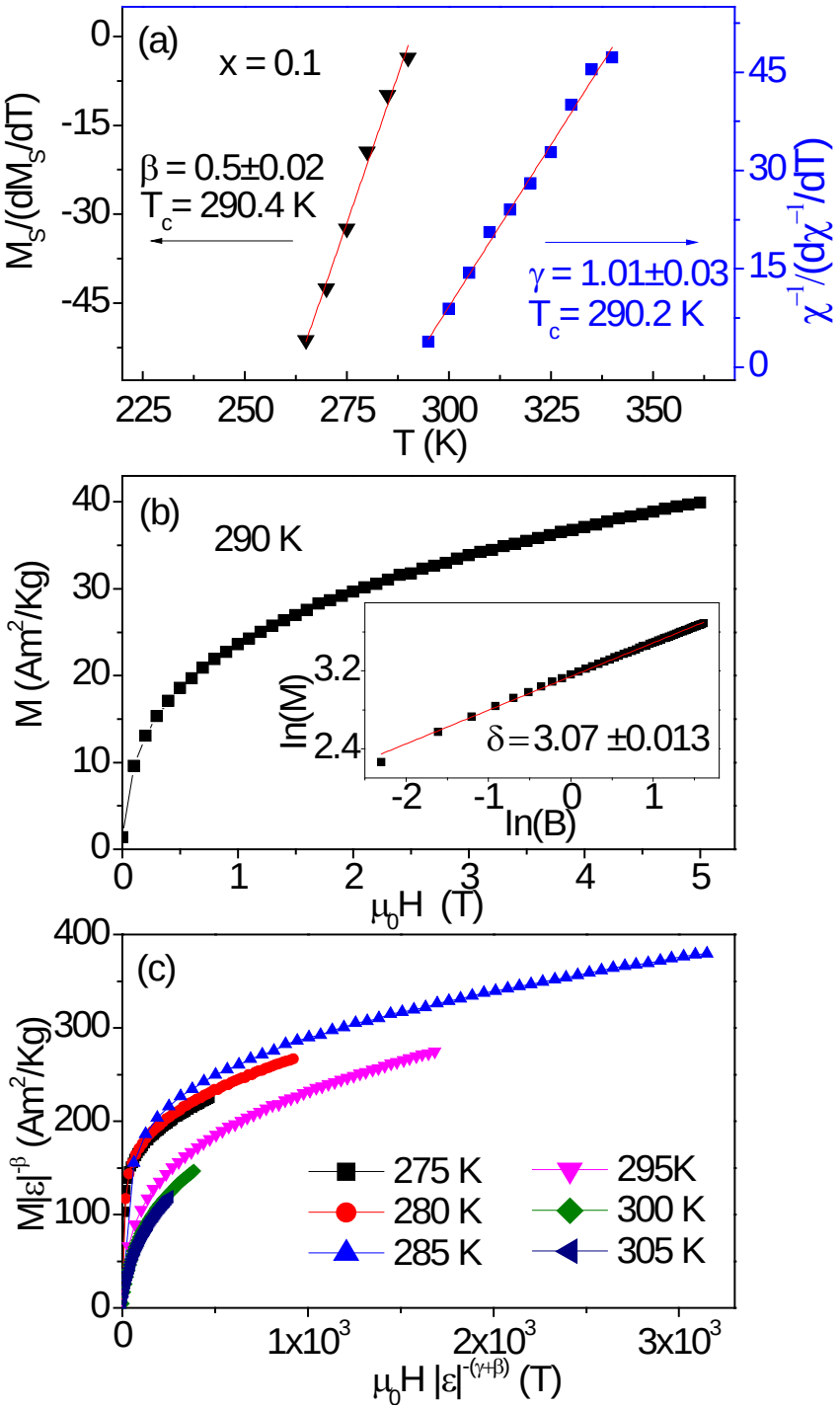

Fig. 3.6. Critical exponent analysis of $TbCo_2Mn_{0.1}$ for (a) Kouvel–Fisher plot for the spontaneous magnetization $M_S(T)$ and the inverse initial susceptibility χ^{-1}(solid lines are fitted to Eqs. 3.3 and 3.4, (b) (Color online)Critical isotherm of M vs H close to the Curie temperature T_C = 290 K. Inset shows the same on log-log scale and the straight line is the linear fit following Eq. 3.5. The critical exponent δ is obtained from the slope of the linear fit. (c) Scaling plots indicating universal curves below and above T_C.

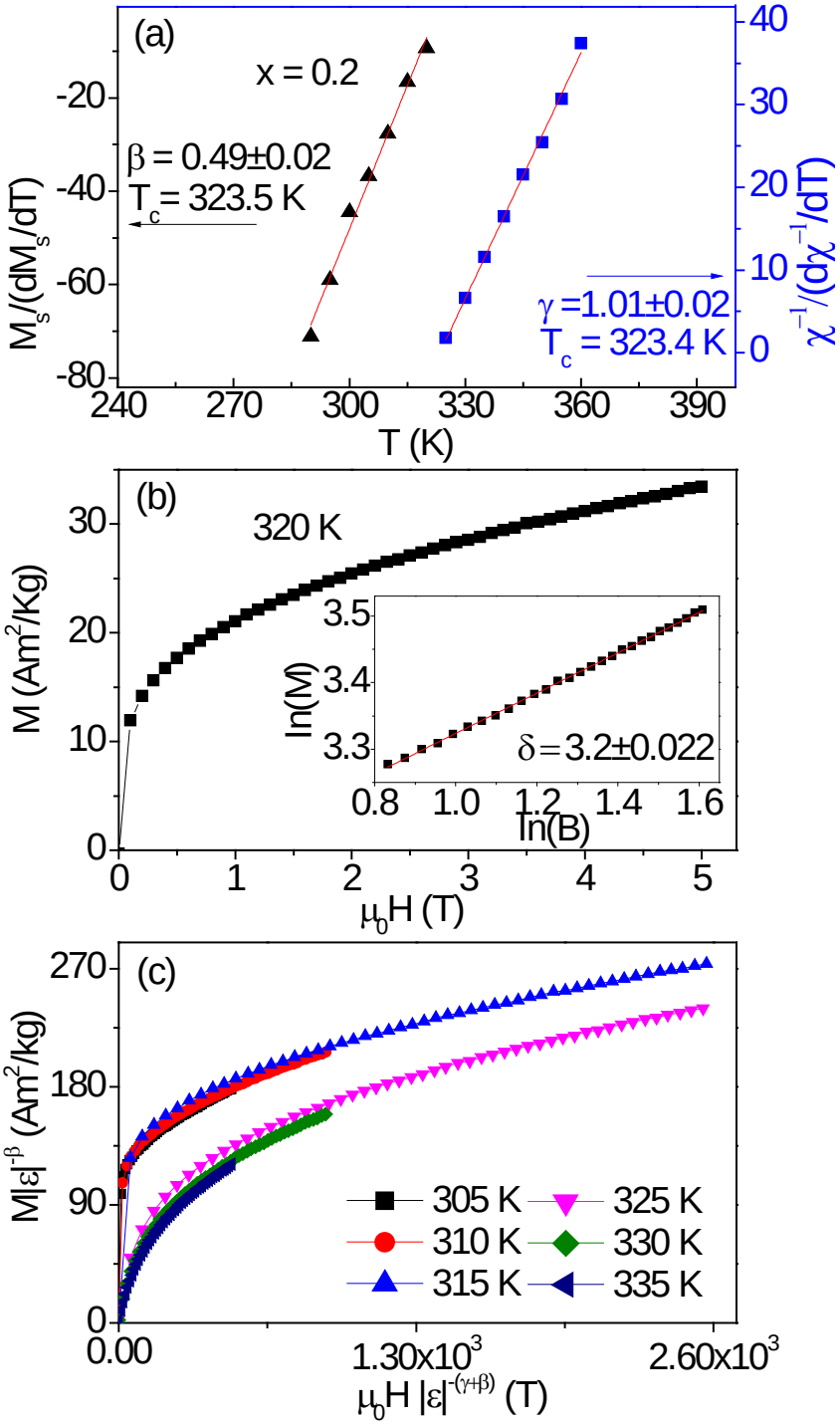

Fig. 3.7. Critical exponent analysis of $TbCo_2Mn_{0.2}$ for (a) Kouvel–Fisher plot for the spontaneous magnetization M_S (T) and the inverse initial susceptibility χ^{-1}(solid lines are fitted to Eqs. 3.3 and 3.4, (b) (Color online) Critical isotherm of M vs H close to the Curie temperature T_C = 320 K. Inset shows the same on log-log scale and the straight line is the linear fit following Eq. 3.5. The critical exponent δ is obtained from the slope of the linear fit. (c) Scaling plots indicating universal curves below and above T_C.

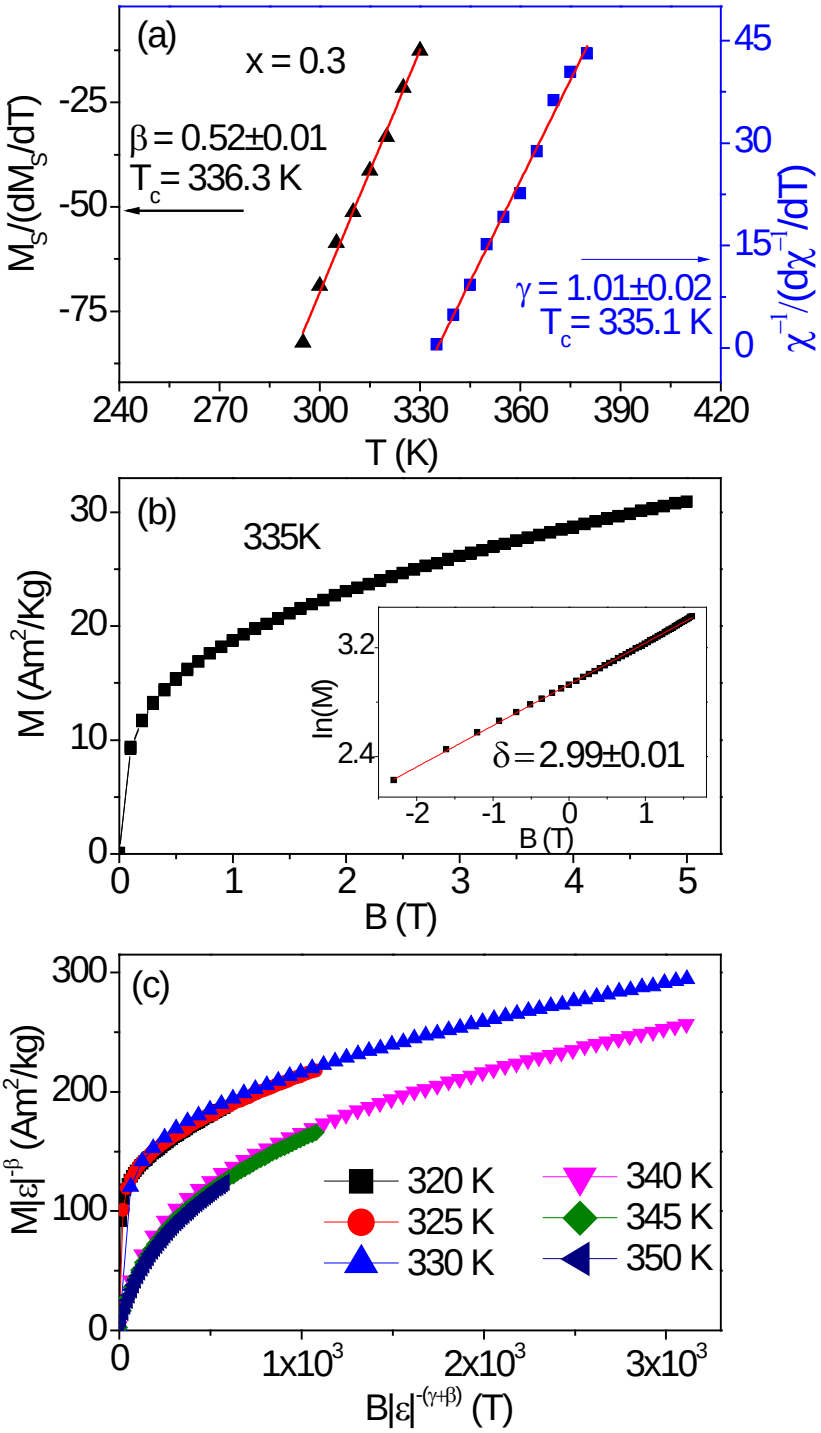

Fig. 3.8. Critical exponent analysis of $TbCo_2Mn_{0.3}$ for (a) Kouvel–Fisher plot for the spontaneous magnetization M_S (T) and the inverse initial susceptibility χ^{-1}(solid lines are fitted to Eqs. 3.3 and 3.4,(b) Color online Critical isotherm of M vs H close to the Curie temperature T_C = 335 K. Inset shows the same on log-log scale and the straight line is the linear fit following Eq. 3.5. The critical exponent δ is obtained from the slope of the linear fit. (c) Scaling plots indicating universal curves below and above T_C.

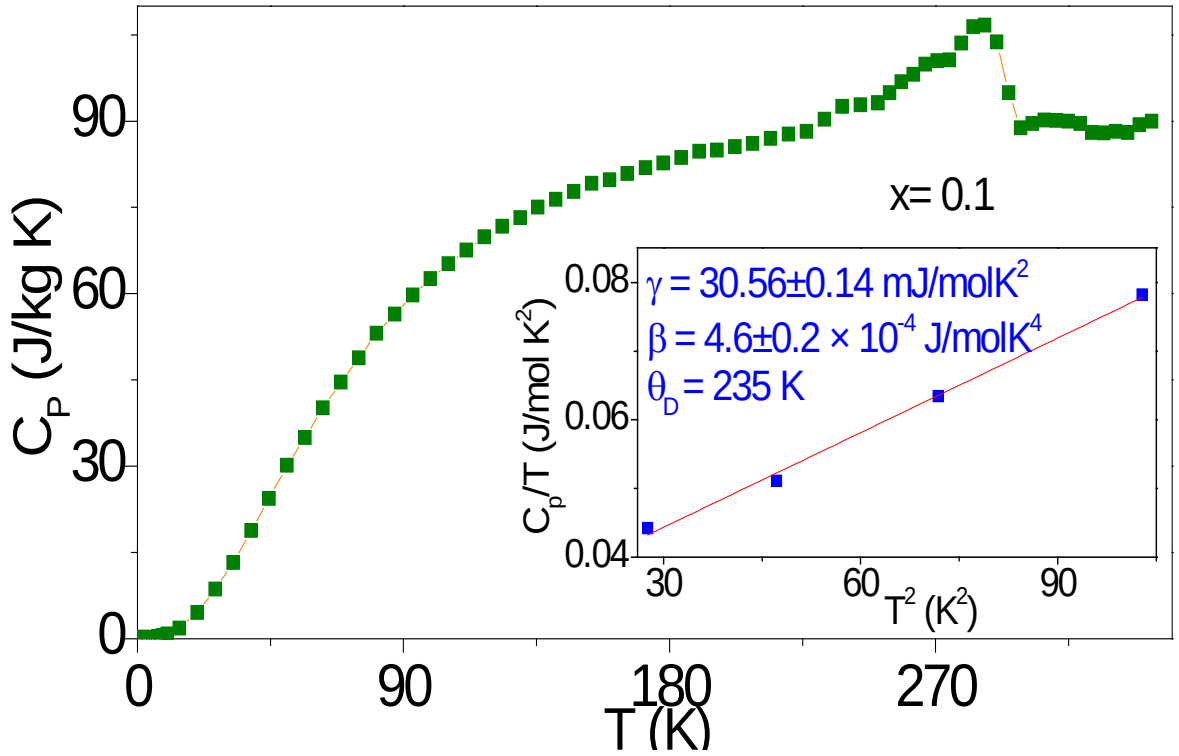

Fig. 3.9. Heat capacity vs temperature curve of $TbCo_2Mn_{0.1}$ at B = 0 T and inset shows C_p/T *vs* T^2 *(*K^2*)* straight line with linear fitting.

3.3.5 Heat Capacity

The temperature dependent heat capacity for $TbCo_2Mn_{0.1}$ at B = 0 T is shown in Fig. 3.9. An obvious peak appears at 284 K which is ascribed to the Curie temperature of $TbCo_2Mn_{0.1}$. The total heat capacity $C(T)$ of a metallic magnetic material can described as the sum of various contributions from phonons, electrons and magnon. The detailed deviation can be seen in **Chapter 2.2.4**, so applying a linear fitting approach to the low temperature specific heat at of $TbCo_2Mn_{0.1}$, one can obtain the values of $\gamma = 30.5\ \mathrm{mJ/molK^2}$ and $\beta = 4.6 \times 10^{-4}\ \mathrm{J/molK^4}$. And the N ($E_F$) can be calculated to be 3.04 state/eV atom compared with 2.0 state/eV for similar material $TbNi_2$.[72] Finally, the Debye temperature θ_D can also be deduced to be 235 K for $TbCo_2Mn_{0.1}$, which is close to the value reported for $TbNi_2Mn$ (θ_D = 200 K).[70]

3.3.6 Magneto-elastic Coupling: Synchrotron and Neutron Diffraction

The x-ray diffraction patterns (synchrotron radiation) along with the Rietveld refined results at T = 90 K (magnetic state) and T = 300 K (paramagnetic state) for $TbCo_2Mn_{0.1}$ are shown in Fig. 3.10(a) and 10(b), respectively. In this case of $TbCo_2Mn_{0.1}$ for synchrotron x-ray diffraction at 300 K, the pattern factor, *Rp*, the weighted pattern factor, *Rwp* and the expected pattern factor R_{exp} are found to be 5.41%, 6.79%, and 2.66%, respectively. For the pattern at 90 K, the values of R_p, R_{wp} and R_{exp} are 5.91, 7.54 and 2.97, respectively.

From refinements of XRD patterns at variable temperatures, we found that for the all $TbCo_2Mn_x$ compounds that the structure exhibits a rhombohedral distortion below T_C. This transformation from the cubic to the rhombohedral structure is illustrated by a magnified plot in Fig. 3.10(c).It can be seen that the peak [220] at 300 K for the cubic structure ($Fd\bar{3}m$ space group) is replaced by two peaks [110] and [104] of the rhombohedral structure (space group $R\bar{3}m$) at 90 K. Many details of the structural features around T_C can be observed from our high resolution X-ray powder diffraction study. For example, the temperature dependence of the synchrotron diffraction patterns near the room temperature cubic [220] peaks are shown in Fig. 3.11(a),

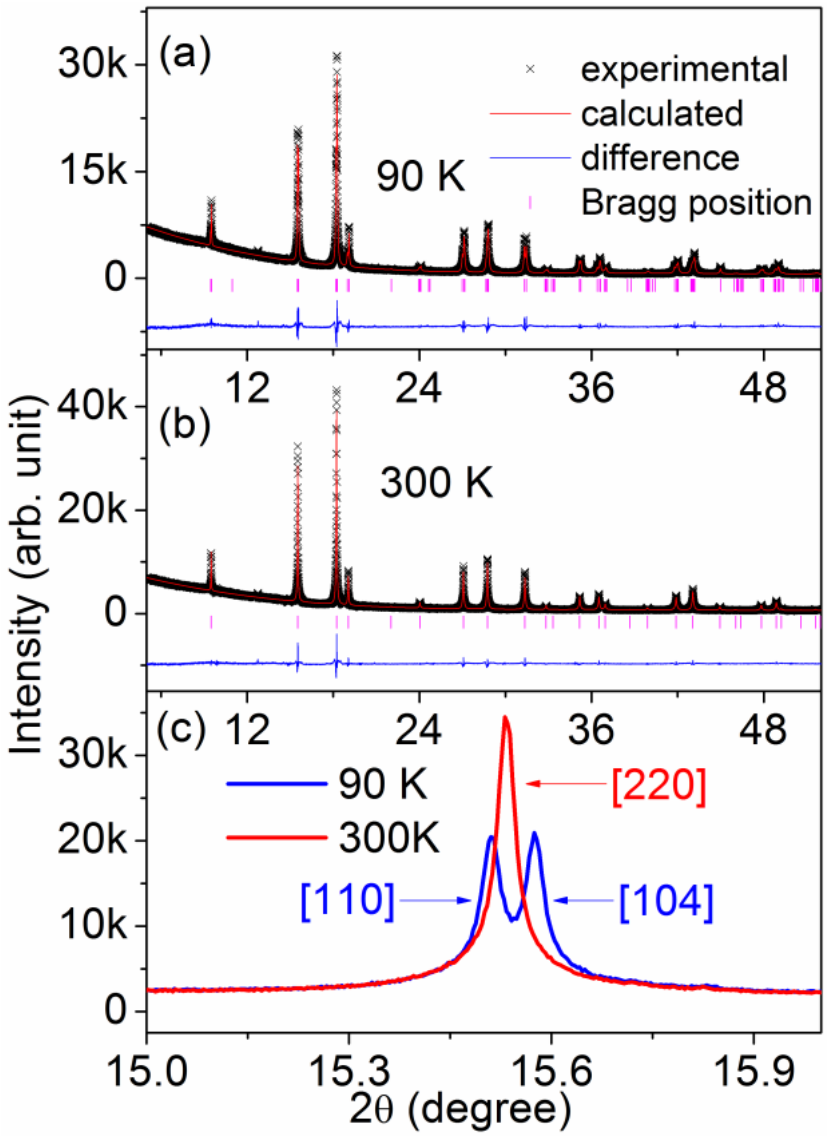

Fig. 3.10. X-ray diffraction patterns (synchrotron radiation) of $TbCo_2Mn_{0.1}$ at (a) 90 K and (b) 300 K; (c) is a magnified plot showing the (cubic) [220] peak replaced by two rhombohedral peaks, [110] and [104], with cooling.

11(b) and 11(c). It can be seen that below the Curie temperature T_C (marked by the white horizontal line), the [220] peak transforms into two smaller separated peaks as the temperature is lowered following a period of distortion. The peak transformation can be observed more clearly in the plot of temperature dependent peak widths shown in Fig. 3.11(d). The solid symbols within each plot mark the Curie temperature for $TbCo_2$, $TbCo_2Mn_{0.1}$ and $TbCo_2Mn_{0.2}$, respectively, and also the onset of the [220] peak distortion with further cooling. When the width as plotted becomes much broader compared with the [220] peak above T_C, it reflects that the peak has transformed into the two new peaks as shown in Figs. 3.11(a), 11(b) and 11(c). Clearly we can conclude that there is a structural transition, cubic to rhombohedral,

concurrent with the magnetic state change from paramagnetic to ferromagnetic. However, it cannot be definitively determined from current data whether this transformation proceeds via a rhombohedral distortion process or a period of phase coexistence.

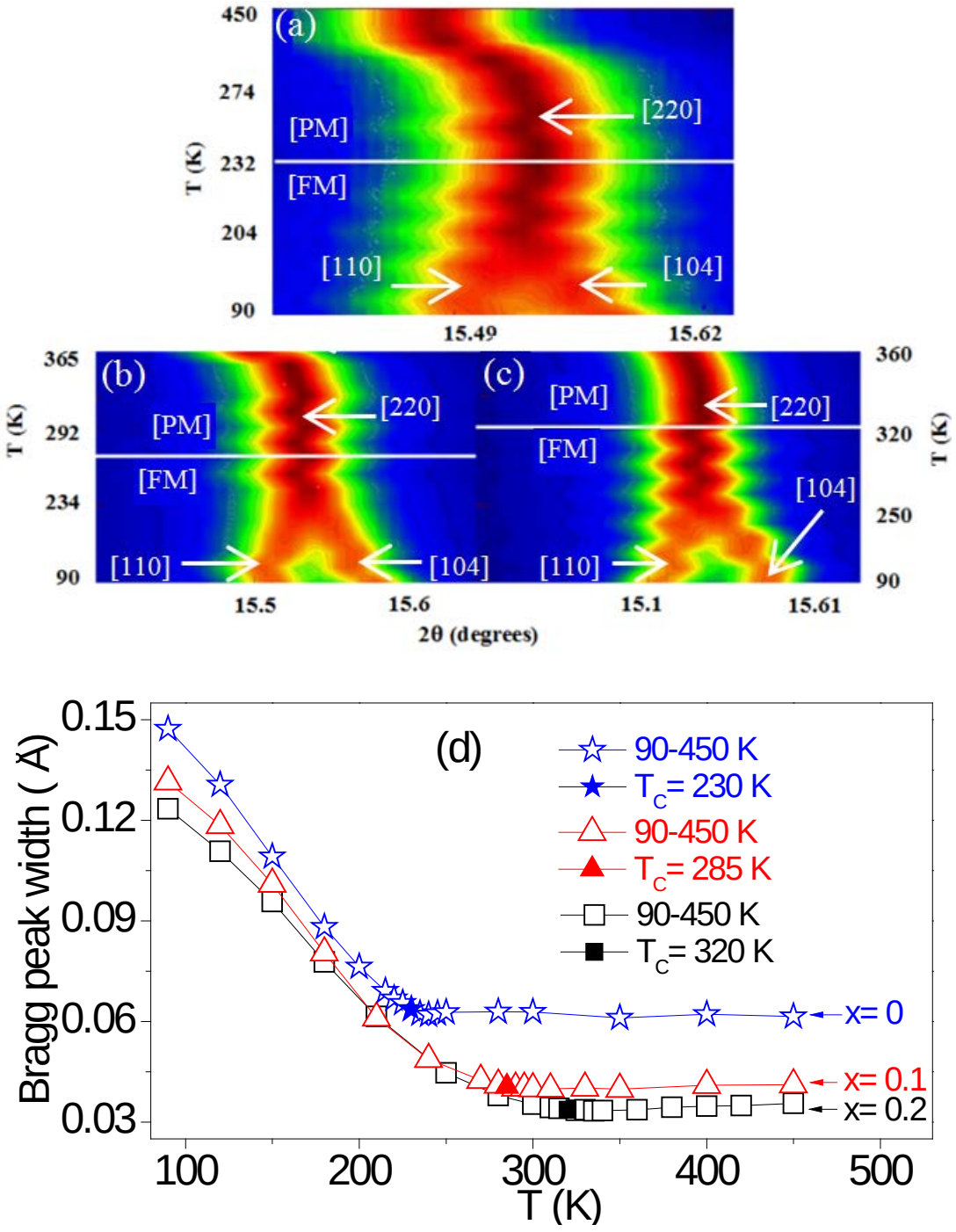

Fig. 3.11. Synchrotron x-ray Bragg at various temperatures from 90 K to 450 K showing the [220] peak transforming into two small peaks ([110], [104]) after cooling to below T_C for (a) $TbCo_2$, (b) $TbCo_2Mn_{0.1}$, (c) $TbCo_2Mn_{0.2}$ and, (d) combined peak widths (Full Width at Half Maximum) from 90 K to 450 K.

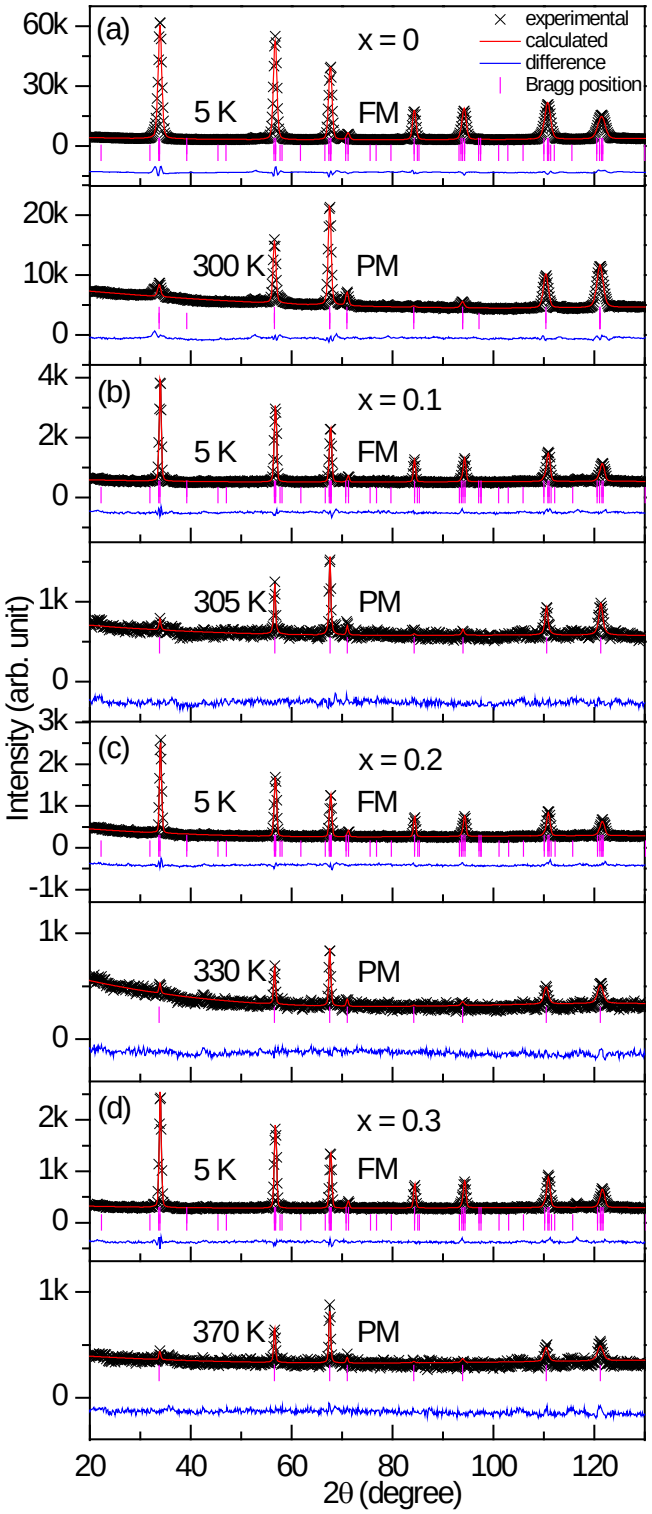

Fig. 3.12. Neutron-diffraction patterns of $TbCo_2Mn_x$ (x = 0.1, 0.2 and 0.3) at 5 K (magnetic state) and higher temperature (paramagnetic state). The black crosses are the experimental Neutron-diffraction data and the red lines represent the Rietveld refined pattern. The difference between the experimental and calculated patterns is shown at the bottom by the blue solid curves. The vertical bars indicate the position of allowed Bragg peaks.

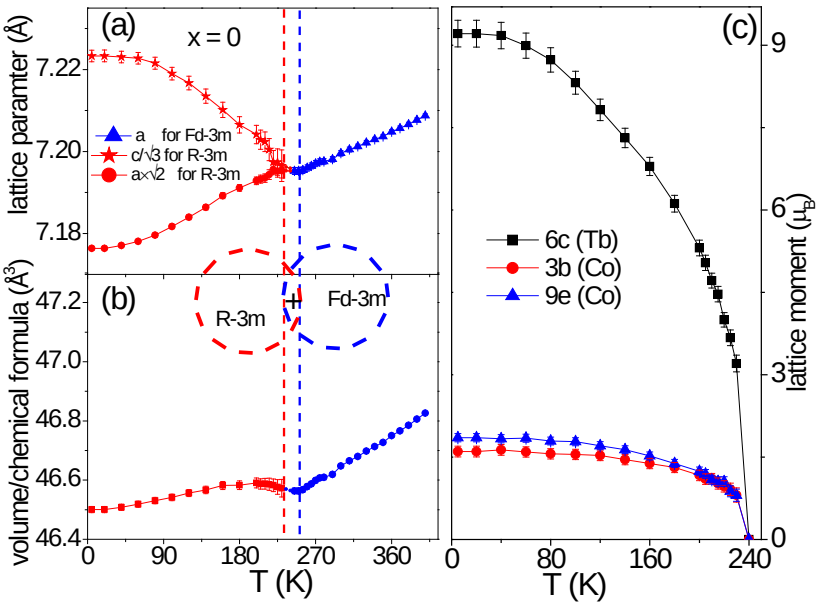

Fig. 3.13. Temperature dependence in $TbCo_2$ of (a) lattice parameters, (b) volume per chemical formula and, (c) ordered magnetic moment in each site (6c, 3b and 16d). Between the two vertical dashed lines is the phase transition region with possible both rhombohedral and cubic structure apparently present.

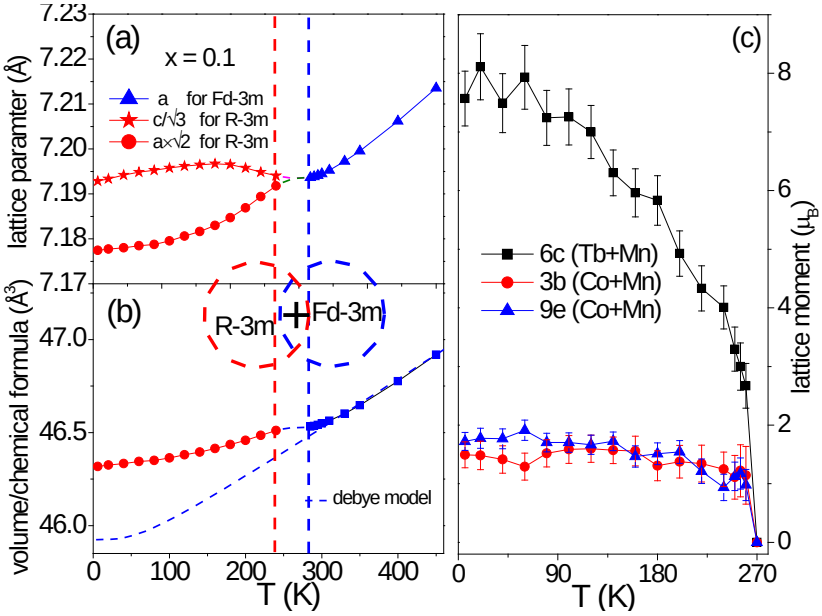

Fig. 3.14. Temperature dependence for $TbCo_2Mn_{0.1}$ of (a), lattice parameters, (b) volume per chemical formula and, (c) ordered magnetic moment in each site (6c, 3b and 16d). Between the two vertical dashed lines is the phase transition region with possible both rhombohedral and cubic structure apparently present.

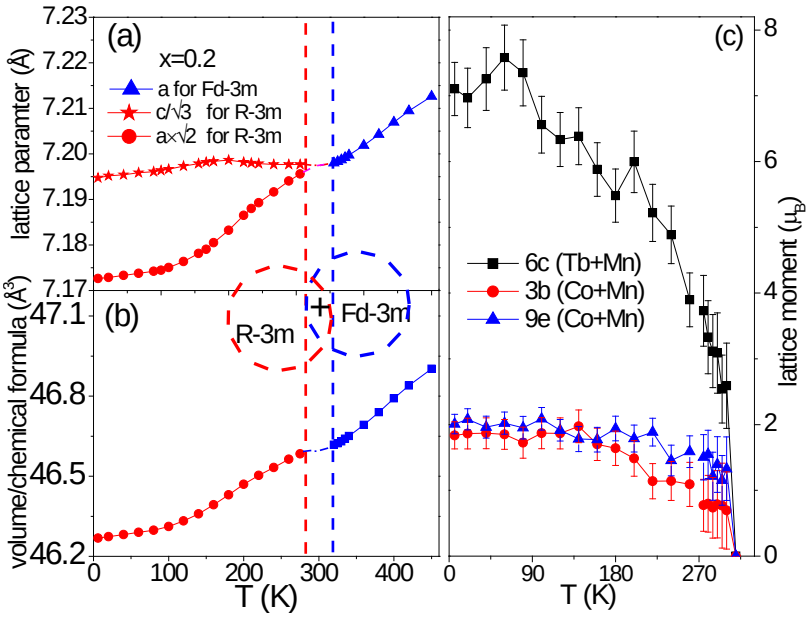

Fig. 3.15. Temperature dependence for $TbCo_2Mn_{0.2}$ of (a) lattice parameters, (b) volume per chemical formula and, (c) ordered magnetic moment of each site (6c, 3b and 16d). Between the two vertical dashed lines is the phase transition region with possible both rhombohedral and cubic structure apparently present.

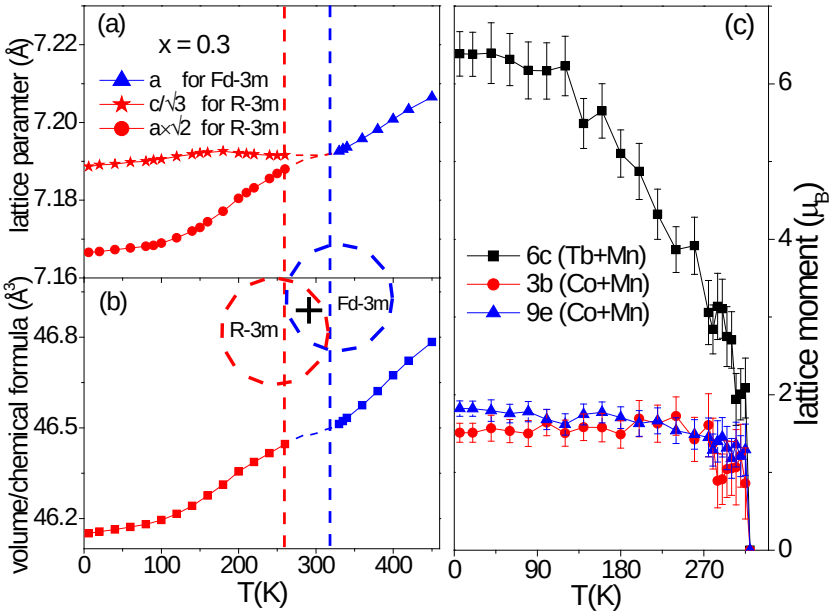

Fig. 3.16. Temperature dependence for $TbCo_2Mn_{0.3}$ of (a), lattice parameters, (b) volume per chemical formula and, (c) ordered magnetic moment in each site (6c, 3b and 16d). Between the two vertical dashed lines is the phase transition region with possible both rhombohedral and cubic structure apparently present.

In order to determine the magnetic structure and derive magnetic information, we carried out a variable temperature neutron diffraction study (5 K−400 K). This neutron diffraction data, including refinements carried out with the Fullprof package, are shown in Fig. 3.13 to Fig. 3.16 for x = 0, 0.1, 0.2 and 0.3, respectively and main results are listed in Table 3.2. The results of the atomic occupancies (Tb, Co and Mn) in both the cubic and rhombohedral structures estimated via the refinements are listed in Table 3.3. In order to compare directly between the lattice parameters of the cubic structure ($Fd\bar{3}m$) and the rhombohedral structure ($R\bar{3}m$) at the transition, we modify the rhombohedral lattice parameters of using $a \times \sqrt{2}$ and $c/\sqrt{3}$. The results for x = 0 are shown in Fig. 3.13. The variation in lattice parameters of $a \times \sqrt{2}$ and $c/\sqrt{3}$ with temperature below T_C displays strong anisotropy: the lattice parameter $a \times \sqrt{2}$ (red solid circles) increases monotonically while $c/\sqrt{3}$ (red solid stars) decreases with increasing temperature. At T_C the crystal structure transforms from rhombohedral to cubic above which a increases monotonically with temperature. The temperature dependence of the cell volume (Fig. 3.13(b)) exhibits behaviour typical of a first order transition with a noticeable drop near T_C. In contrast with $TbCo_2$, in the Mn doped compounds, the temperature variation of the lattice parameter $a \times \sqrt{2}$ tends to become less pronounced while $c/\sqrt{3}$ still increases monotonically. The combined effect therefore is a more pronounced change in volume in the Mn doped cases. In addition and using the Debye temperature θ_D obtained from data of Fig. 3.9, a theoretical estimate based on Debye theory (dash lines) is also plotted for the x = 0.1 case in Fig. 3.14(b). The spontaneous volume magnetostriction ω_s (= $\Delta V_m/V$) at 5 K for x = 0.1 is calculated to be 8.5×10^{-3}. In our refinement, it is assumed that the moments of the magnetic atoms in the compound have a collinear alignment similar the model described in the investigation for $TbCo_2$.[73] The Tb moment is derived to be 9.21μ_B at 5 K while the Co moments at 3b site and 9e site are 1.85 μ_B to and 1.60 μ_B, respectively. Since the limitation of data resolution would not support the increased number of refinement parameters for the compounds containing Mn, we derive only the average moment for each site as shown in Figs. 3.14-16

As an example, the parameters resulting from refinement of the neutron diffraction patterns at 5 K, and near T_C for all the $TbCo_2Mn_x$ compounds are listed in Table 3.2. It can be seen that the average moment at the rare earth site decreases with increasing Mn content which indicates that some Mn atoms substitute onto this site and carry a magnetic moment that couples in an antiparallel alignment with the Tb.

3.4. Conclusion

Novel compounds $TbCo_2Mn_x$ (x = 0.1, 0.2 and 0.3) with Cubic $MgCu_2$-type structure at 300 K have been successfully synthesized. Our study of the magnetic properties in the series indicates that magnetic phase transition for the $TbCo_2$ compound is first order, but the addition of Mn changes the nature to second order. Furthermore the addition of Mn into $TbCo_2$ compounds leads to a significant increase in T_C but an obvious reduction of spontaneous magnetization. A detailed analysis of critical exponent of the magnetic behaviour around T_C shows that these systems indeed undergo a second order phase transition and that the magnetic exchange interaction is long range. Our high resolution x-ray powder diffraction study confirms that all compounds crystallize in the cubic Laves phase C15 structure above their Curie temperature T_C and transform to a rhombohedral phase (space group $R\bar{3}m$) below T_C. Magnetic structure and magnetic moments below T_C have been determined through a variable temperature neutron diffraction investigation.

Table 3.1 Deduced critical exponents β, γ and δ for $TbCo_2Mn_x$ (x =0.1, 0.2 and 0.3) compounds along with standard critical exponents of three standard theories: 3D Heisenberg model, Mean field (MF) Theory and 3D Ising Model

Composition		Technique	β	γ	δ
$TbCo_2Mn_x$	x = 0.1	Kouvel-Fisher method	0. 50±0.02	1.01±0.03	3.07±0.01
	x = 0.2		0.49±0.02	1.01±0.02	3.20±0.02
	x = 0.3		0.52±0.01	1.01±0.02	2.99±0.01
3D Heisenberg model		Theory	0.365	1.386	4.80
Mean field (MF) Theory		Theory	0.500	1.000	3.00
3D Ising Model		Theory	0.325	1.241	4.82

Table 3.2 Structure parameters and atomic moments of $TbCo_2Mn_x$ (x = 0.1, 0.2 and 0.3) compounds at 5 K and temperature near T_C. The uncertainties are shown for the $TbCo_2$ data as an example.

Parameter	x = 0		x = 0.1		x = 0.2		x = 0.3	
T (K)	5	230	5	260	5	300	5	315
a× $\sqrt{2}$ (Å)	7.176(1)	7.195(5)	7.177	7.192	7.173	7.198	7.167	7.191
$c/\sqrt{3}$ (Å)	7.223(4)	7.197(1)	7.193	7.194	7.195	7.198	7.189	7.192
V (Å^3)	46.50(3)	46.57(9)	46.31	46.51	46.27	46.59	46.15	46.49
6c (μ_B)	9.21(60)	3.20(31)	7.57	2.67	7.10	2.59	6.39	2.10
3b (μ_B)	1.60(30)	0.81(21)	1.50	1.14	1.84	0.69	1.51	0.80
9e (μ_B)	1.85(21)	0.81(31)	1.72	0.98	2.01	1.33	1.82	1.20
M_{total} (μ_B)	5.76(61)	1.58(31)	4.35	0.55	3.25	0.57	3.06	0.00

Table 3.3 Atomic (Tb, Co and Mn) occupancy in cubic and rhombohedral structure respectively.

x	Cubic $Fd\bar{3}m$				Rhombohedral $R\bar{3}m$					
	8a		16d		6c		3b		9e	
	Tb	Mn	Co	Mn	Tb	Mn	Co	Mn	Co	Mn
0	100.00%	0.00 %	100.00 %	0.00 %	100.00 %	0.00 %	100.00 %	0.00 %	100.00 %	0.00 %
0.1	96.77 %	3.23 %	96.77%	3.23 %	96.77%	3.23 %	96.77%	3.23 %	96.77%	3.23 %
0.2	93.76 %	6.24 %	93.76%	6.24 %	93.76%	6.24 %	93.76%	6.24 %	93.76%	6.24 %
0.3	90.93 %	9.07 %	90.93%	9.07 %	90.93%	9.07 %	90.93%	9.07 %	90.93%	9.07 %

CHAPTER 4 INVESTIGATION ON THE $HoCo_2Mn_x$ (x = 0.0, 0.2, 0.5, 0.7, 1.0) COMPOUNDS

4.1. Introduction

Magnetic refrigeration based on the magnetocaloric effect (MCE) of magnetic materials has attracted great interest in recent years.[74] RCo_2 (R = rare earth) compounds with cubic laves phase series have been considered to be promising magnetic materials used for the magnetic refrigeration because of their large magnetic entropy change $-\Delta S_M$ and the tunable temperature of the magnetic-state transition.[65] For example, $DyCo_2$, $HoCo_2$ and $ErCo_2$ were reported to exhibit huge magnetic entropy change $-\Delta S_{max}$ = 14.5 J kg^{-1} K^{-1}, 22.0 J kg^{-1} K^{-1} and 28.0 J kg^{-1} K^{-1} with the field change 0 T-7 T at their transition temperatures T_C = 140 K, 84 K and 42 K respectively.[9] However, all the above materials are only suitable for the low temperature refrigeration due to their low ordering temperatures. In order to raise the Curie temperature T_C and thus for higher refrigeration operation temperature, other elements were chosen to dope into the compound. For example, 20% element ratio Ga was doped into $DyCo_2$ resulting in T_C sharply increased from 143 K to 196 K (for $DyCo_{1.8}Ga_{0.2}$), although with a significant decrease of magnetic entropy change $-\Delta S_M$ from 8.24 J kg^{-1} K^{-1} to 3.51 J kg^{-1} K^{-1}.[3] Besides the Curie temperature and magnetic entropy change, operational temperature is also an important factor for the magnetic refrigeration application due to its contribution to the refrigeration capability (RC).[75-78] For instance, $La_{0.7}Sr_{0.3}MnO_3$ bulk has 30 K operational temperature (from 340 K to 270 K), while $La_{0.7}Sr_{0.3}MnO_3$ nanotube arrays has much broader operational temperature from 190 K to 270 K, which means $La_{0.7}Sr_{0.3}MnO_3$ nanotube arrays can refrigerate efficiently at a wider temperature range.[79] RCo_2 compounds with heavy rare earth element (such as Tb, Dy, Ho and Er) have been proved to exhibit collinear-ferrimagnetic structure where Co-sublattice moments antiparallel couple with R-sublattice moment below the Curie temperature T_C. And reflected on the various interesting magnetic and electronic properties of RCo_2 (R = rare earth) compounds, the crystal and magnetic structure is the key point to clarify the physics principle behind.[61]

$HoCo_2$ compound was thought to be a unique magnetic material not only due to its huge magnetic entropy change but also its spin reorientation at low temperature (around 16 K) (its easy magnetization direction changes from [100] to [110] during cooling process). Thus

many works had been carried out on $HoCo_2$ in order to clarify its magnetic properties.[80] Recently, a sharp increase in the heat capacity below 1 K was found in $HoCo_2$, which can be an ideal property for the ultra-low temperature refrigeration application.[81] Meanwhile, $HoCo_2$ was also thought to be a potential material for application as sensor due to its first order magnetic transition which is sensible to the external magnetic field and hydrostatic pressure.[82-85] To improve the magnetic properties of $HoCo_2$, other element with proportion (0.0-1.0) had been doped to replace Co (for example, in $Ho(Co_{1-x}Si_x)_2$ Compounds[84]) or Ho (such as, Tb[84] and Gd[85]). It was found that the Curie temperature was raised from T_C = 81 K (for $HoCo_2$) to T_C = 103 K (for $HoCo_{1.9}Si_{0.1}$), T_C = 149 K (for $Ho_{0.6}Tb_{0.4}Co_2$) and T_C = 300 K (for $Ho_{0.4}Gd_{0.6}Co_2$) with drastic magnetic entropy change decreasing. Moreover, thermal expansion properties of materials are of fundamental interest and control of thermal expansion is important for practical applications but can be difficult to achieve. Negative thermal expansion materials have attracted much attention due to their potential application.[86-89] It is reported that RCo_2 related compounds exhibit strong magneto-elastic coupling[51, 81] Recently, magneto-structural coupling has been found to play a critical role in many useful multifunctional properties, namely, giant magnetoresistance, magnetocaloric effect, and magnetostriction.[90-93] A few different models have been formulated to describe the negative thermal expansion phenomenon in certain alloys (invar effect).[94] The strong magnetovolume effects present in RCo_2 compounds are considered to be connected with a magnetic instability of the Co-sublattice[95]and can be well described within the conventional s-d (d-f) model.[96, 97]

Novel RNi_2Mn (R = Tb, Dy, Ho, Er) compounds were synthesized and investigated by Wang et al.,[59, 56] reporting that all the RNi_2Mn samples exhibit the cubic $MgCu_2$-type structure ($Fd\bar{3}m$, space group), the same as RNi_2. Recently, similar materials RCo_2Mn (with R = Ho and Er) compounds were reported and the introduction of Mn brought a significant increase of T_C from 78 K for $HoCo_2$ to 248 K for $HoCo_2Mn$.[56] However, so far no systematic work on $HoCo_2Mn_x$ was done to investigate the effect of proportional (x = 0.0-1.0) element addition on structural and magnetic properties.

In this work, series of $HoCo_2Mn_x$ compounds with x = 0.0, 0.2, 0.5, 0.7 and 1.0 were successfully synthesised. All the samples were characterised by x-ray diffraction (XRD) at room temperature, which shows that all compounds are pure phase with $MgCu_2$-type crystal structure same as $HoCo_2$. Through the magnetic and the specific heat capacity

measurements, it was found that, with more Mn doped from x = 0.0 to 1.0, T_C increase efficiently from 88 K to 253 K while M_S decreases from 160 emu/g to 102 emu/g with a sharp value decrease of the peak magnetic entropy change $-\Delta S_{max}$ from 12.87 J kg^{-1} K^{-1} to 1.25 J kg^{-1} K^{-1} (with a magnetic field change from 0 Oe to 50 kOe). Spin orientation with EMD changing from [100] to [110] was also found at T_{Spin}. Compared with the report about the nature of spin orientation in $HoCo_2$,[98, 99] the neutron diffraction patterns analysis here confirmed that both magnetic-state transitions at T_C and T_{sin} in $HoCo_2$ belong to the first order transitions and with Mn doped the order of magnetic phase transition at T_C transform into the second order. Meanwhile with Mn doping level increasing, a huge increasing refrigeration temperature range of PM-FM transition was observed: from range of 80-120 K for $HoCo_2$ to 40-280 K for $HoCo_2Mn$. The Debye temperature θ_D and the density of energy state $N(E_F)$ were calculated based on the heat capacity measurement.

4.2. Experimental Techniques

The polycrystalline $HoCo_2Mn_x$ (with x = 0.0, 0.2, 0.5, 0.7 and 1.0) compounds were prepared by standard arc melting constituent elements of 99.9 % purity under argon atmosphere. Considering the non-proportionate losses of Mn during arc-melting and annealing process, 3% additional Mn was added initially. Then the prepared ingots were wrapped with tantalum foil and sealed in quartz glass tubes in vacuum circumstance to anneal. The samples were heated to 1173 K dwelling for 7 days in muffle furnace and then quenched into ice water. Magnetic measurements were performed respectively using a Quantum Design 9 T and 14 T physical properties measurement system (PPMS). The magnetic phase transition behaviour was investigated over the range from 5 K to 300 K in a magnetic field of 100 Oe. Magnetization-field loops were obtained at selected temperatures near the Curie temperature of each sample with magnetic fields varying from 0 T to 5 T. The heat capacity measurements C_P were carried out from 2 K to 300 K using 9 T PPMS at UNSW at Canberra. Both the crystal and magnetic structure transitions were clarified by refinement (using Fullprof package) of neutron diffraction pattern measured on the high-intensity powder diffractometer Wombat at the OPAL facility (Lucas Height, Australia) with a neutron wavelength of 2.4139 Å from 5 K to 400 K.

4.3 Results and Discussion

4.3.1 Magnetic Phase Transition

Temperature dependence of magnetizations from 300 K to 5 K for all the samples in a field of 100 Oe are shown in Fig. 4.1(a). It can be seen that an abrupt rise near the Curie temperature T_C in each *M-T* curve can be detected obviously which reflects a magnetic transition from paramagnetic state (PM) to ferrimagnetic state (FM). With the *x* value increasing from 0.0 to 0.2, 0.5, 0.7 and 1.0, the Curie temperature T_C increases sharply from 88 K to 149 K, 225 K, 251 K and 253 K respectively. The visible tendency of T_C in dependence on the *x* value is depicted in the right top corner inset in Fig. 4.1(a). Previous study indicated that one spin reorientation in $HoCo_2$ occurs near 16 K with the easy magnetization direction from [110] to [100].[80] Here we also can see the similar spin reorientation transition peaks appearing in each *M-T* curve of each sample as shown in Fig. 4.1(a). (Note the values of the spin orientation transition temperature T_{sr} and the Curie temperature T_C are defined as the places where the absolute values of *dM/dT* are maximum).[100] The composition dependence of T_C and T_{sr} is shown in the inset of Fig. 4.1(a).

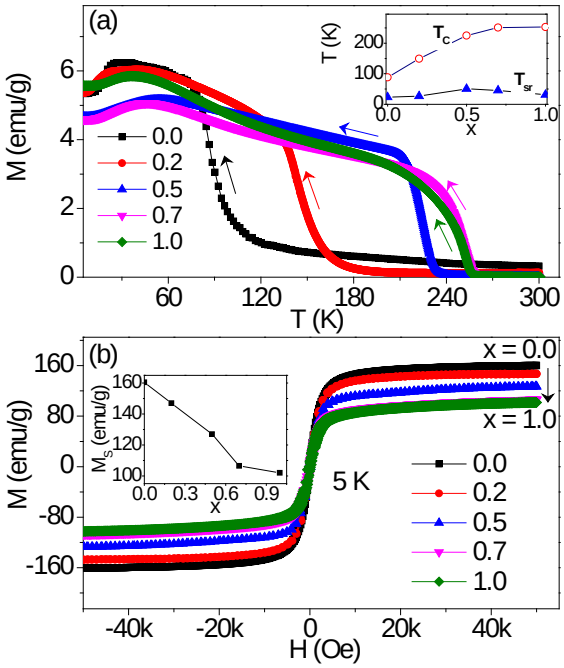

Fig. 4.1. (a) Temperature dependence of magnetic moment from 300 K to 5 K after field cooling with 100 Oe for $HoCo_2Mn_x$ (*x* = 0.0, 0.2, 0.5, 0.7 and 1.0) series compounds. The inset shows the value of T_C and T_{sr} variation with the x value. (b) 5 K hysteresis loop for $HoCo_2Mn_x$ (*x* = 0.0, 0.2, 0.5,0.7 and 1.0) and the inset shows the spontaneous magnetic moment M_S dependence on the *x* value.

Fig. 4.1(b) shows the hysteresis loop at 5 K for each sample. As the black arrow directs on the right top corner, the spontaneous magnetic moment M_S decreases from 160 emu/g to 102 eum/g with the x value increasing from 0.0 to 1.0. The composition dependence of M_S at 5 K is shown in the inset of Fig. 4.1(b). It can be concluded that the addition of Mn can efficiently raise the value of T_C while with a significant decrease in M_S. The origin of the increased T_C can be ascribed to the enhanced exchange interactions between the 3d transition-metal[102] after Mn introduction. It is well accepted that in the rare earth (R) transition metal (T) compounds the indirect exchange interaction between the 3d spins of the T elements and the 4f spins of the heavy R element (more than half-full 4f shell) exhibits ferrimagnetic or antiferromagnetic coupling. The decreased M_S can be understood in the term of the presence of Mn element whose sub-lattice moment is antiparallelly coupled to Ho-sublattice, which will be further discussed based on neutron diffraction refinement results in **Section 4.3.5**.

Magnetization isotherms at selected temperatures around T_C were obtained for the samples $HoCo_2Mn_x$ compounds. The *M-H* curves for the compound with x = 0.0, 0.2 and 1.0 are shown in Figs. 4.2(a), 4.2(b) and 4.2(c), respectively, as typical examples. Corresponding to the abrupt change in magnetization around magnetic phase transition temperature (PM-FM) in the *M-T* curve in Fig. 1(a), the order of this transition can also be reflected from the isothermal curves shape transformation: from straight line symbolizing paramagnetism to curve line indicating ferrimagnetism shown in Figs. 4.2(a), 4.2(b) and 4.2(c). Meanwhile, it is well accepted that the magnetization isotherms overlap between the field decreasing and increasing processes stands for the negligible hysteresis loss. The corresponding Arrott plots (M^2-H/M) for the related samples (as shown in Fig. 4.3.) are derived based on the isotherms magnetization curves. According to the shape of Arrott plots near T_C, the nature of the magnetic phase transition can be deduced: the S-shape curve with negative slope for x = 0.0 is indicative of first order transition while the L-shape curves (solid blue line depicts in Fig. 4. 3(c) as a typical example) with positive slope for x = 0.2 and 1.0 indicate second order transition.[65, 102] So it can be concluded that with the Mn addition, the nature of the magnetic transition transforms from first order to second order for the parent $HoCo_2$ to $HoCo_2Mn_x$. The verdict can be further confirmed in **Section 4.3.5** by Neutron diffraction pattern refinement analysis.

4.3.2 Magnetocaloric Effect

Based on the magnetization isotherms shown in Fig. 4.2., the magnetic entropy changes $-\Delta S_M$ in function of temperatures can be deduced out using the standard Maxwell relationship:

$$\Delta S_M(T,H) = \int_0^{H^{max}} \left(\frac{\partial M(H,T)}{\partial T}\right)_H dH \quad (4.1)$$

The entropy changes as a function of temperature are shown in Fig. 4.4(a), (b) and (e) for x = 0.0, 0.2 and 1.0. As an example to illustrate in Fig. 4.4(a) for $HoCo_2$, we can see obviously that two peaks appear in each curve with five different magnetic field changes (from ΔH = 0 kOe -10 kOe to 0 kOe -50 kOe): the peak at lower temperature corresponds to the spin reorientation while the other peak at lower temperature (around T_C) corresponds to the PM-FM transition. However, compared with the parent compound $HoCo_2$ (see Fig. 4.3(a), it can be seen from Fig. 4.3(b) and Fig. 4.3(c) for the $HoCo_2Mn_x$ compounds that the values of these two peaks become smaller with more Mn doped. This can be partly ascribed to the weakness of magneto-volume effects which will be discussed in details below and shown by the neutron data analysis in **Section 4.3.5.** Meanwhile, we can see with the more Mn content added, the PM-FM transition peak (in Figs. 4.3(a) and 4.3(b)) become more flat while with a broad operation temperature range appearing compared with Fig. 4.3(a). The value of $-\Delta S_{max}$ around T_C and T_{sr} decreases from 12.8 J kg^{-1} K^{-1} and 5.0 J kg^{-1} K^{-1} for x = 0.0 to 1.3 J kg^{-1} K^{-1} and 1.8 J kg^{-1} K^{-1} for x = 1.0, respectively. So through the peak transformation affected by the volume effect, we also can track the clue to the nature of the magnetic transition change (from first order to second order) discussed in Fig. 4.2. A large operation temperature span is an essential factor for the active magnetic refrigeration (AMR) due to the direct relation with the total magnetic refrigeration capacity.[79]

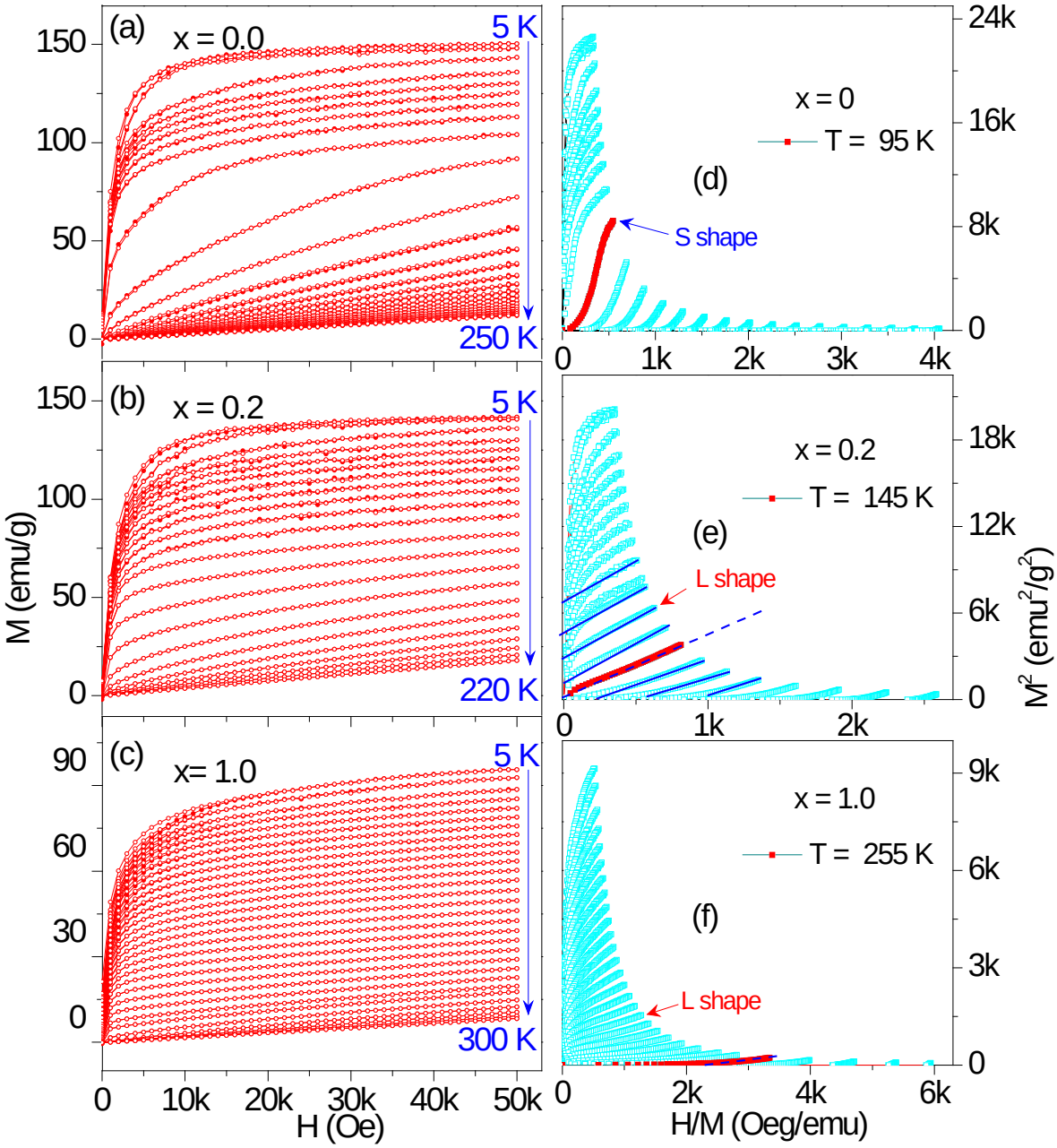

Fig. 4.2. Magnetization isotherms of (a) $HoCo_2$, (b) $HoCo_2Mn_{0.2}$ and (c) $HoCo_2Mn$. Solid circles represent increasing field process while the hollow squares symbolize for the decreasing field process. (Here we just choose the isothermal 10 K interval to make the curves clearly displayed. Actually the full temperature interval is 5 K). (d), (e) and (f) represent the Arrott plots corresponding to the magnetization isotherms in the decreasing field process in Figs. 4.2(a), (b) and (c).

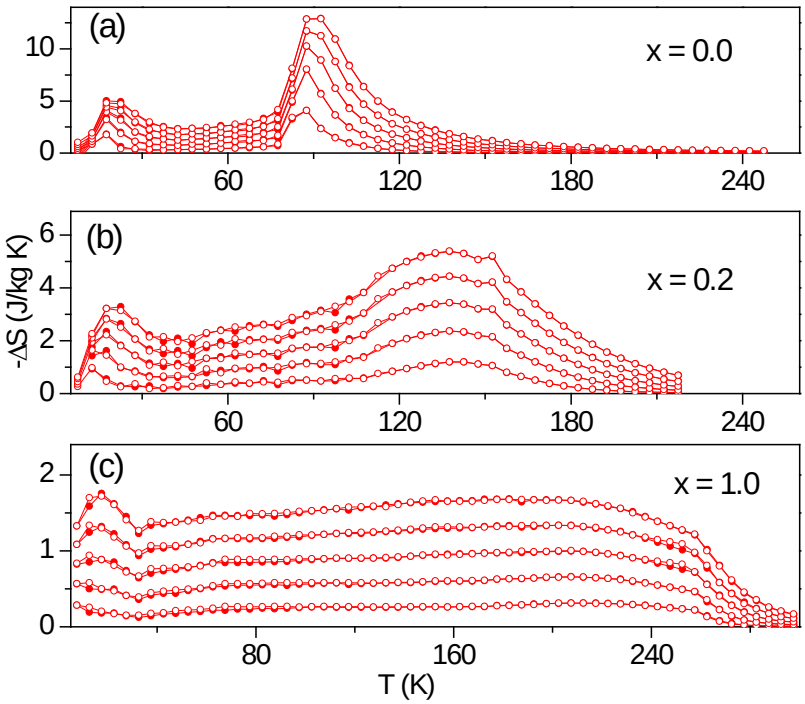

Fig. 4.3. The magnetic entropy changes $-\Delta S$ at series temperatures under five different magnetic fields changes (0 kOe -10 kOe, 0 kOe -20 kOe, 0 kOe -30 kOe, 0 kOe -40k Oe and 0 kOe -50 kOe) corresponding to each curve from bottom to top for (a) $HoCo_2$, (b) $HoCo_2Mn_{0.2}$ and (c) $HoCo_2Mn$ (red solid icons for increasing field while the hollow ones for the decreasing field).

4.3.3 Critical Exponents Analysis

The critical exponents β, γ and δ are the criterions do decide the nature of the second order transition (3D Heisenberg model, Mean-field theory or 3D Ising model).[103, 104] According to scaling hypothesis, β, γ and δ can be calculated out based on the following equations:[105]

$$M_S(0,T) = M_0(-\varepsilon)^{\beta}, \ \varepsilon < 0, \tag{4.2}$$

$$\chi_0^{-1}(0,T) = (h_0/M_0)(\varepsilon)^{\gamma} \tag{4.3}$$

$$M(H, T_C) = A_0(H)^{1/\delta} \tag{4.4}$$

Where $\varepsilon = (T\text{-}T_C)/T_C$, M_S is spontaneous magnetization below T_C, χ_0^{-1} is initial susceptibility above T_C and $M(H)$ is magnetic moment at T_C. M_0, h_0/M_0 and A_0 are constants of the critical amplitudes. $M_S\ (T)\ and\ \chi_0^{-1}\ (T)$ can be derived from the high field data of the Arrott plot shown in Fig. 4.3(b) as an example. (solid blue lines).[106]

Furthermore, deduced respectively from Eqs. (4.2) and (4.3), the Kouvel-Fisher use the counterpart equations: [106]

$$\frac{M_S(T)}{dM_S(T)/dT} = \frac{T-T_C}{\beta} \tag{4.5}$$

$$\frac{\chi_0^{-1}(T)}{d\chi_0^{-1}(T)/dT} = \frac{T-T_C}{\gamma} \tag{4.6}$$

So the values of slopes $1/\beta$, $1/\gamma$ and T_C can be obtained by linear fitting of the $M_S/(dM_S(T)/dT)$ and $\chi_0^{-1}(T)/\ (d\chi_0^{-1}(T)/dT)$ shown in Fig. 4.5(b).

As discussed in Fig. 4.3, only $HoCo_2Mn_{0.2}$ belongs to mean-filed theory, which can be directly calculated out the specific values of β, γ using the standard Arrott plot. Here for comparison, two methods were used to calculated out the value of β and γ: one is $M_S(0, T)$ and $\chi_0^{-1}(0, T)$ no-linear fittings according to Eqs. (4.2) and (4.3) shown in Fig. 4.5(a); the other is a more precise Kouvel-Fisher technique using linear fitting according to Eqs. (4.5) and (4.6) shown in Fig. 4.5(b). We found for both methods, the values of β and γ are consistent well with each other, which means both methods are reliable. Meanwhile the value of δ = 2.807±0.007 according to Eq.(4.4) shown in Fig. 4.5(c), compared with the value of δ= 2.959±0.085 according to the Widom scaling relation[107]

$$\delta = 1 + \gamma/\beta \tag{4.7}$$

Finally, to confirm all our calculated critical exponent and T_C are accurate and reliable, the value of β and γ were put into universal curves function $M(H, \varepsilon)$ according to the scaling hypothesis:[47]

$$M(H, \varepsilon) = \varepsilon^{\beta} f \pm (H/\varepsilon^{\beta+\gamma}) \tag{4.8}$$

Which collapse into two branches respectively for temperatures above and below T_C as shown in Fig. 4.5. It means that all our calculations of exponent and T_C are exact and unambiguous.

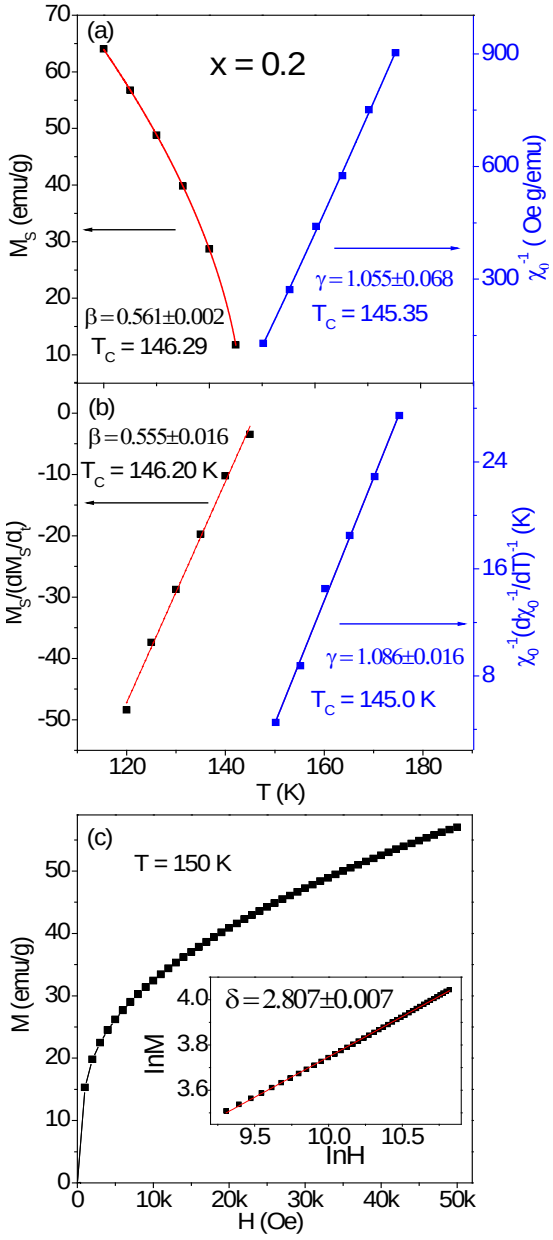

Fig. 4.4. (a)Temperature dependent spontaneous magnetization $M_S(0, T)$ and inverse initial susceptibility $\chi_0^{-1}(0, T)$ with no-linear fitting(colour solid lines) according to Eqs. (4.2) and (4.3). (b) Using Kouvel-Fisher method linear fitting according to Eqs. (4.5) and (4.6) to obtain the value of β and γ.(c) Critical isotherm of M vs H near T_C = 149 K. Inset exhibits the same on log-log scale at high field with the linear fitting according to Eq.(4.4) shown as the red straight line, whose reciprocal value of slope is the value of δ.

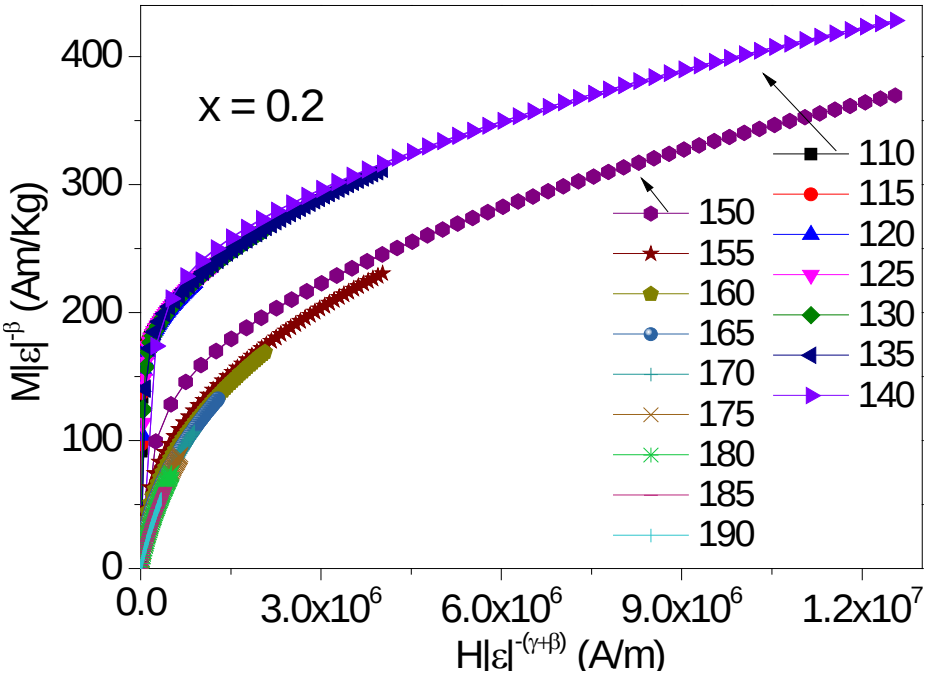

Fig. 4.5 Scaled magnetization of $HoCo_2Mn_{0.2}$ above and below T_C according to the scale hypothesis Eq. (4.8), which indicates all the experimental *M (H)* curves near T_C will collapse into two branches for the temperatures above and below T_C respectively.

4.3.4 Heat Capacity

The temperature dependent heat capacity at $\mu_0 H$ = 0 T and 2 T respectively for $HoCo_2Mn_{0.2}$, $HoCo_2Mn_{0.5}$ and $HoCo_2Mn$ were shown in Fig. 4.13(a), (b) and (c). We can find that there is no obvious peak in each curve at the Curie temperature for each sample, which proves further that the magnetic transition at T_C for Mn added samples belong to second order.[25] It is well accepted that the heat capacity *C (T)* of a metallic magnetic material can be described as the contributions from phonons, electrons and magnon:[48]

$$C(T) = C_{ph}(T) + C_{el}(T) + C_m(T) \tag{4.9}$$

where C_{ph}, C_{el} and C_m are the lattice, electronic, and magnetic contributions respectively. At low temperature with the absence of a magnetic phase transition, the heat capacity can be expressed as:[46]

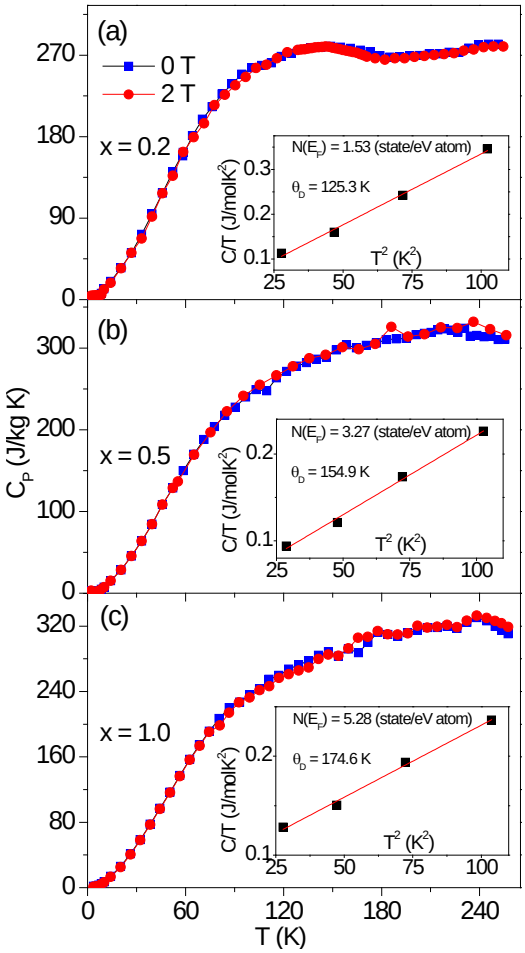

Fig. 4.6. Temperature dependence of the heat capacity in the field of 0 T and 2 T for (a) $HoCo_2Mn_{0.2}$ (b) $HoCo_2Mn_{0.5}$ and (c) $HoCo_2Mn$. Inset in each figure is fitting of *C/T* versus T^2.

$$C\,(T)/T = \gamma + \beta T^2 \tag{4.10}$$

where γ and β are the electronic and phonon heat capacity coefficients, respectively. So at low temperatures $T \leq 10$ K, the specific heat of $HoCo_2Mn$ C_p/T versus T^2 straight line can be linear fitted as show in the insets in Fig. 4.13 to obtain the value of γ and β. Following, the electronic density of states $N\,(E_F)$ at the Fermi surface can be obtained by the formula:[48]

$$\gamma = \frac{k^2{}_B{}^*\pi^2}{3} N(E_F) \tag{4.11}$$

where k_B is the Boltzmann constant.

Likewise, the Debye temperature θ_D can also be deduced out by:[49]

$$\beta = \frac{12*\pi^4*R}{5*\theta^3{}_D} \cong \frac{1944*n}{\theta^3{}_D} \quad (4.12)$$

where R is the universal gas constant and the number of atoms n = 3.2, 3.5 and 4.0 for $HoCo_2Mn_{0.2}$, $HoCo_2Mn_{0.5}$ and $HoCo_2Mn$, respectively. It was found that with the x value increasing, both the value of $N(E_F)$ and Debye temperature θ_D increases (from 1.53 state/eV atom and 125.3 K for $HoCo_2Mn_{0.2}$ to 5.28 state/eV atom and 174.6 K for $HoCo_2Mn$). It was explained that the Curie temperature was risen by the increased values of $N(E_F)$ at the Fermi level and splitting energies of the 3d subbands.[110, 111] Besides, our experimental result is reasonable compared with values from the similar materials: $N(E_F)$ = 3.04 state/eV atom[112] and 2.00 state/eV atom[31] respective for $TbCo_2Mn$ and $TbNi_2$. And the value θ_D = 174.6 K for $HoCo_2Mn$ is close to $HoNi_2Mn$ θ_D = 190.0 $\pm$ 20.0 K.[113]

4.3.5 Neutron Diffraction Pattern Analysis

Neutron powder diffraction measurement for all $HoCo_2Mn_x$ compounds were carried out over 5 K – 400 K in order to obtain detailed information around the phase transitions. Neutron image are shown in Fig. 4.14 (left) with the region around the (111) peak position re-drawn in the right side. In order to draw the details clearer, the representative neutron diffraction patterns for $HoCo_2$ is shown in Fig. 4.15(a) and temperature dependence of the peak height for selected peaks are plotted in Fig. 4.15(b) with the peak (220) centre position being shown as an inset.

Rietveld refinements of the room temperature neutron diffraction patterns above T_C (in the paramagnetic state) indicate that all of the samples crystallize in the $MgCu_2$ structure (with space group of $Fd\bar{3}m$). No new peaks across their magnetic phase transition temperatures appear, indicating that below the T_{spin} and T_C the samples keeps cubic structure. However, it can be seen clearly that strong magnetic contribution to peak intensity is well detected and around these two magnetic phase transition temperatures T_{sr} and T_C, the unit cell is significantly distorted (contraction at T_{sr} and expansion at T_C) during cooling process.

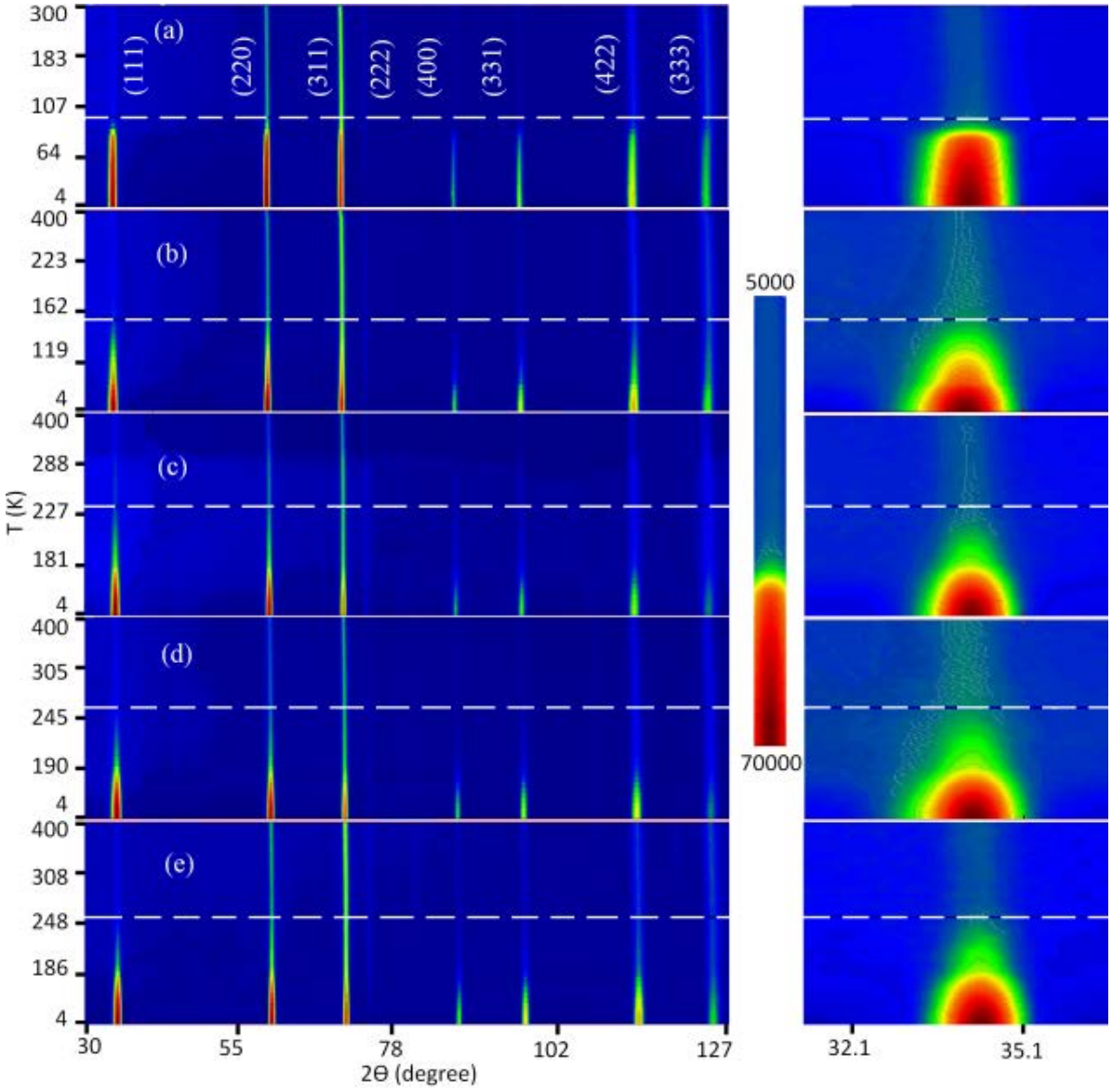

Fig. 4.7. Thermal contour plot of neutron diffraction measurements over 5 K−400 K for $HoCo_2Mn_x$ with x = 0.0 (a), 0.2 (b), 0.5 (c), 0.7 (d) and 1.0 (e).

The similar refinement approach as described in [86, 87] has been used. We take $HoCo_2Mn_{0.5}$ as an example and it is assumed that Mn atoms are located at both Ho (8a) and Co (16d) sites with some vacancies present at the Ho site in order to make $HoCo_2Mn_x$ able to adapt the original $HoCo_2$ structure and satisfy the atomic site ratio $(Ho_{1+v}Mn_y) : (Co_2Mn_{0.5-y})$ to be equal to 1:2, where *v and y* symbolize the number of vacancy and Mn atoms at the Ho site. It was found that the best refinement results can be achieved only when *v = 0.0* indicating that no vacancy exists in $HoCo_2Mn_x$ compounds. The results of the atomic occupancies (Ho, Co and Mn) are listed in Table 4.1. The selected refinement patterns at different magnetic

states are shown in Figs 4.16, 4.17 and 4.18 for $HoCo_2$, $HoCo_2Mn_{0.2}$ and $HoCo_2Mn_{0.7}$ respectively.

Based on the neutron diffraction pattern refinement, the obtained parameters such as lattice volume V and magnetic moment (at 8a and 16d site) as a function of temperature were shown in Fig. 4.19 and Fig. 4.20. It can be seen that in $HoCo_2$ compound due to the first order transitions at both T_{Spin} and T_C, there is an abrupt drop of volume, leading to significant magneto-volume effects, this may make a significant contribution to the total entropy change $-\Delta S_M$ shown in Fig. 4.13 (a). With decreasing temperature, strong negative thermal expansion is detected for x = 0.0 and 0.2 samples below T_C. While for the samples with x = 0.7 and 1.0 thermal expansion goes normally as standard solid with positive thermal expansion. For the sample $HoCo_2Mn_{0.5}$ it can be seen that almost zero thermal expansion below T_C is achieved.

Table 4.1. Atomic (Ho, Co and Mn) occupancy in $HoCo_2Mn_x$ compounds.

x	Cubic $Fd\bar{3}m$			
	8a		16d	
	Ho	Mn	Co	Mn
0.0	100.00%	0.00%	100.00%	0.00%
0.2	93.76%	6.24%	93.76%	6.24%
0.5	85.72%	14.29%	85.72%	14.29%
0.7	81.08%	18.92%	81.08%	18.92%
1.0	74.99%	25.01%	74.99%	25.01%

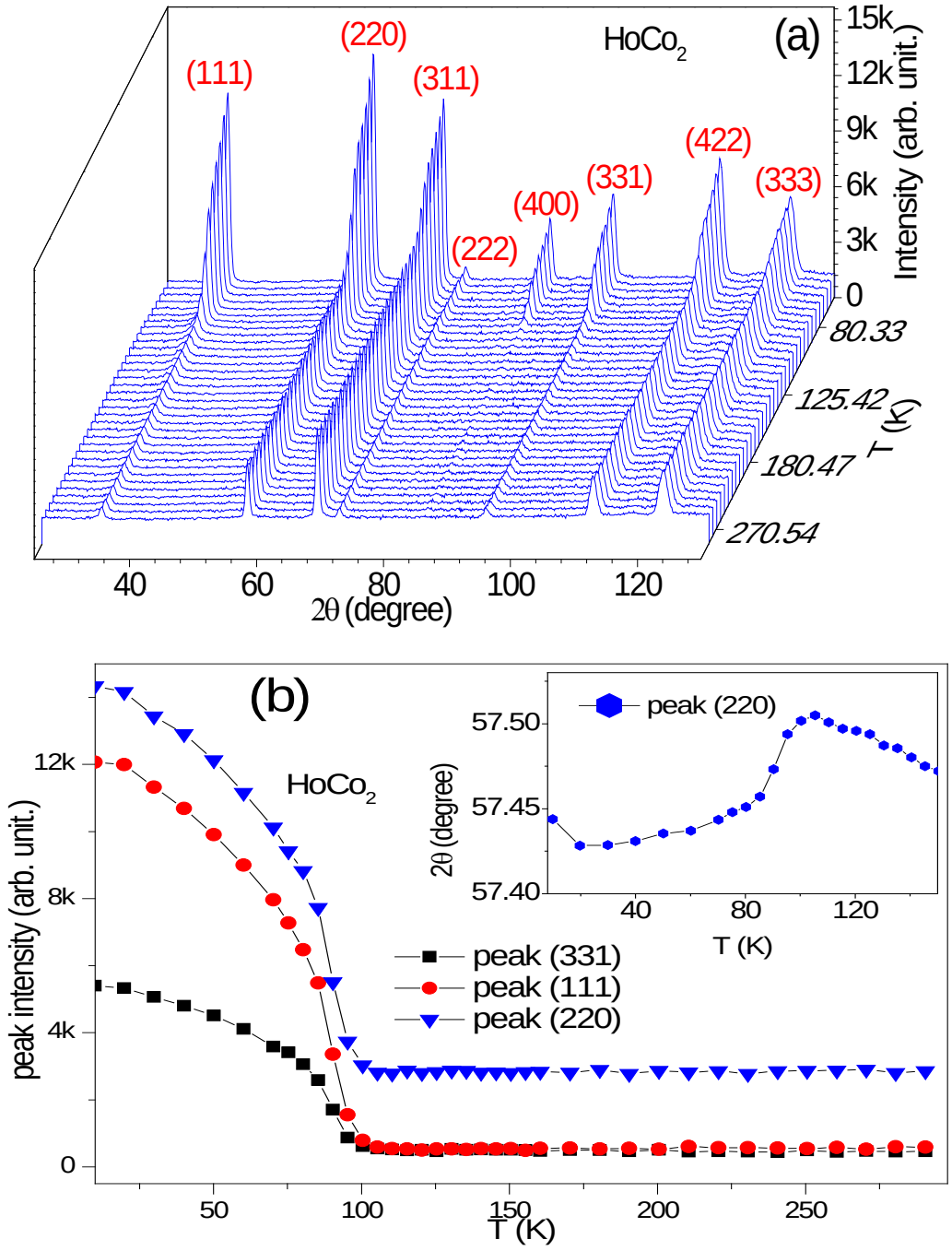

Fig. 4.8. (a) Representative neutron diffraction patterns for $HoCo_2$ over the temperature range 5–300 K at 10 K; (b) Temperature dependence of selected peaks height. Insert of (b) draws the peak (220) centre position as a function of temperature.

It is accepted that the measured thermal expansion of magnetic materials includes two parts of contribution: non-magnetic part ((lattice thermal contribution)) and magnetic part. Nonmagnetic part can be well described through the Grüneisen relation.[89] Using the Debye temperature θ_D obtained from the heat capacity measurement in Fig. 4.14, a theoretical estimation of lattice thermal expansion based on Debye theory (dash lines) can be derived

and has been fitted to the experimental results in the paramagnetic regime. This lattice contribution can be extrapolated from the paramagnetic to ferromagnetic range as drawn by a dashed line. We have calculated the spontaneous magnetostriction by subtracting the lattice thermal expansion from the measured thermal expansion. The spontaneous volume magnetostriction ω_s (= $\Delta V_m/V$) at 5 K for x = 0.2 and 0.5 is calculated to be 7.16×10^{-3} and 8.38×10^{-3} respectively. It is worthy to note that the compounds with $x < 0.7$ have strong magneto-elastic coupling accompanying their magnetic transitions around both Curie temperature T_C and spin reorientation temperature T_{sr}. Unusual transformation from strong negative to positive thermal expansion in $HoCo_2Mn_x$ compounds has been detected. Almost zero thermal expansion over a wide temperature range (over 200 K) can be achieved in the compound $HoCo_2Mn_{0.5}$.

The sub-lattice moments versus temperature are shown in Fig. 4.20. for different compositions. In our refinement, it is assumed that the moments of the magnetic atoms in the compound have a collinear alignment similar to the model described in the investigation for $HoCo_2$.[88] So finally, Ho moment (8a site) is derived to be 6.50 μ_B at 5 K with the reverse Co moment (16d site) being 0.85 μ_B respectively for $HoCo_2$. However, for the Mn doped samples, we only obtained the average moment at 8a site and 16d site (shown in Fig. 4.20) due to the limitation of data resolution.

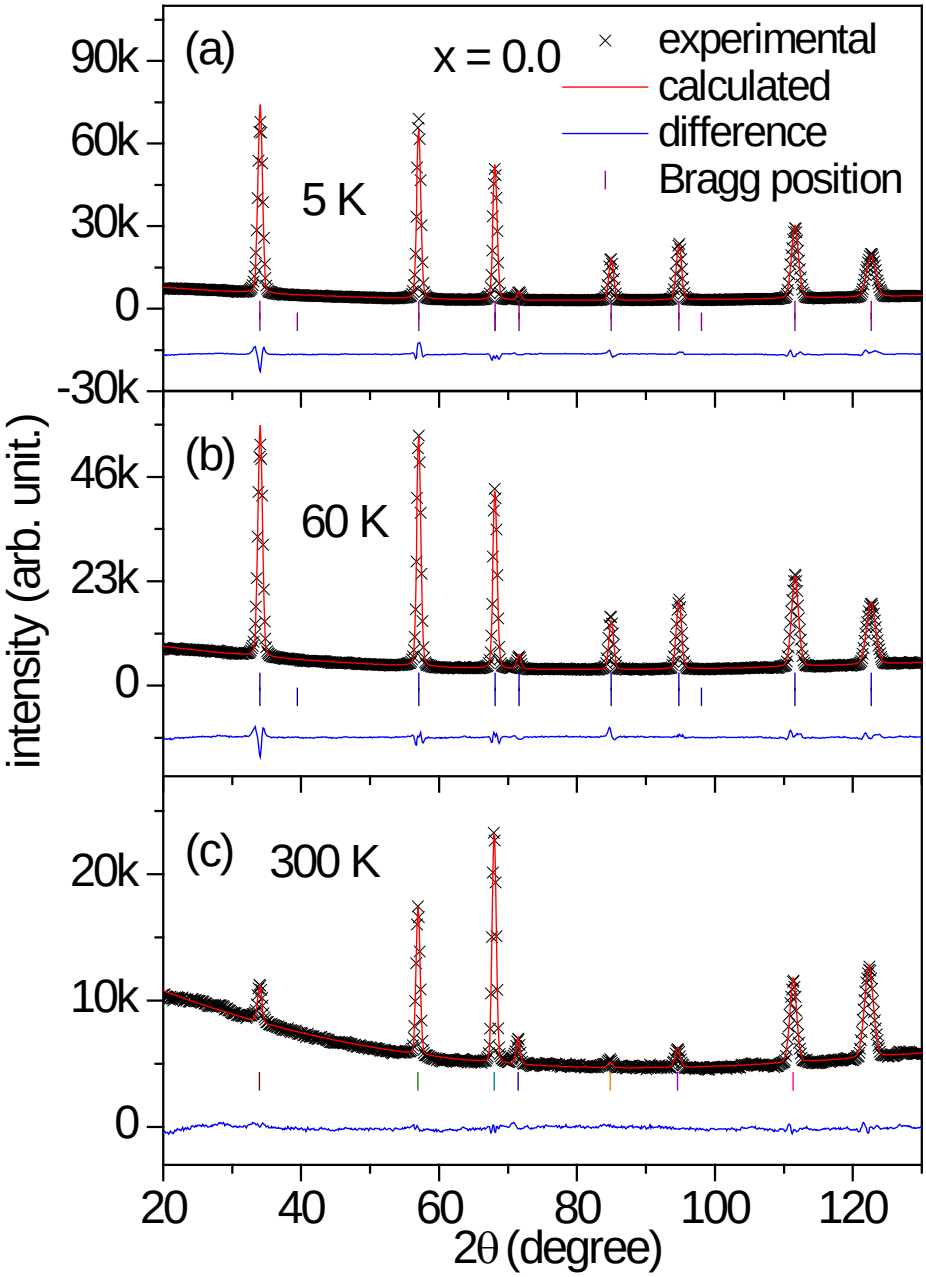

Fig. 4.9. Neutron diffraction patterns of $HoCo_2$ at 5 K below T_{Spin}, 60 K below T_C and paramagnetic-state at 300 K. The black crosses are the experimental Neutron-diffraction data and the red lines represent the Rietveld refined pattern. The difference between the experimental and calculated patterns is shown at the bottom by the blue solid curves. The vertical bars indicate the position of allowed Bragg peaks.

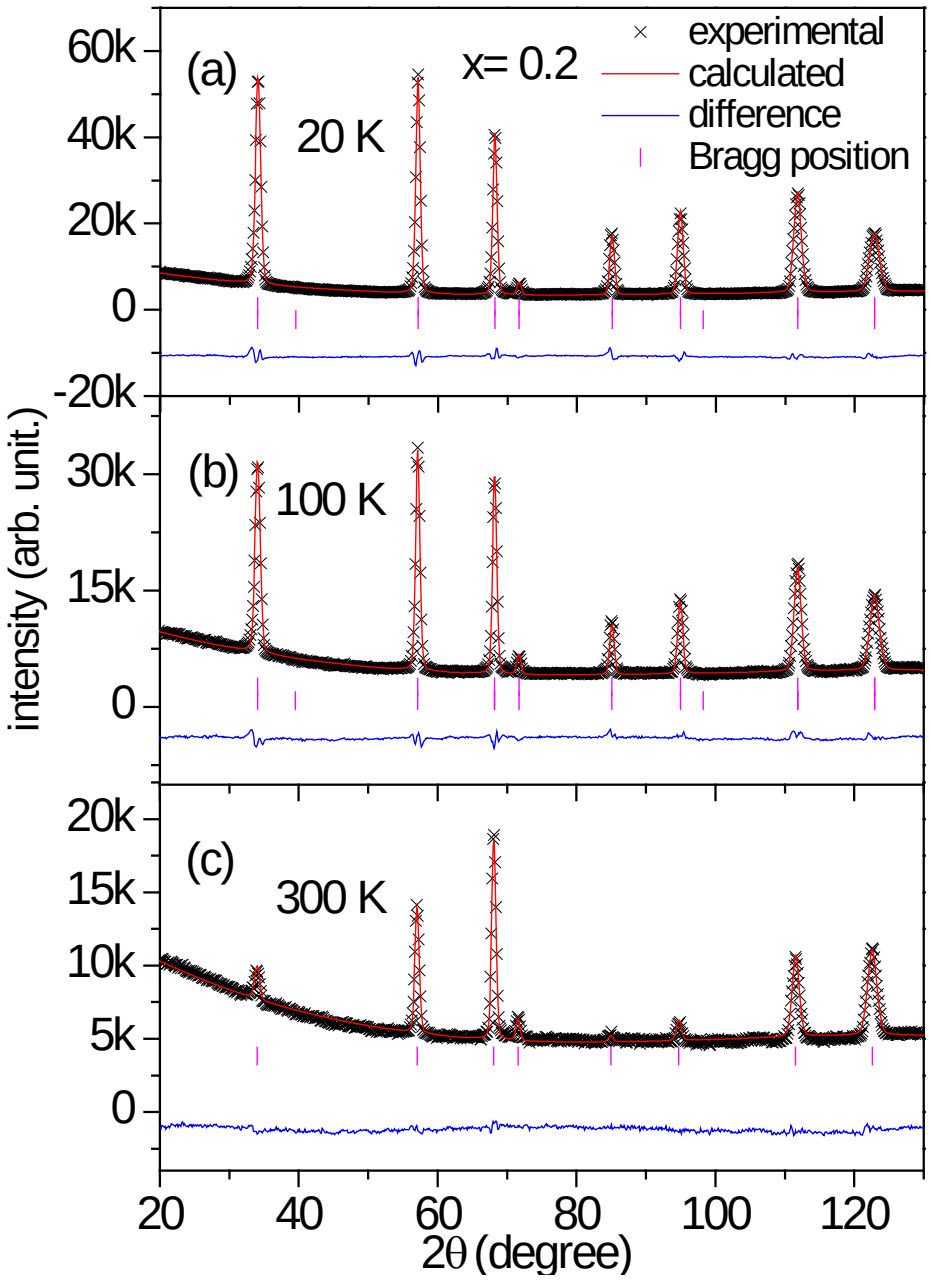

Fig. 4.10. Neutron diffraction patterns of $HoCo_2Mn_{0.2}$ at 5 K below T_{Spin}, 100 K below T_C and paramagnetic-state at 300 K. The black crosses are the experimental Neutron-diffraction data and the red lines represent the Rietveld refined pattern. The difference between the experimental and calculated patterns is shown at the bottom by the blue solid curves. The vertical bars indicate the position of allowed Bragg peaks.

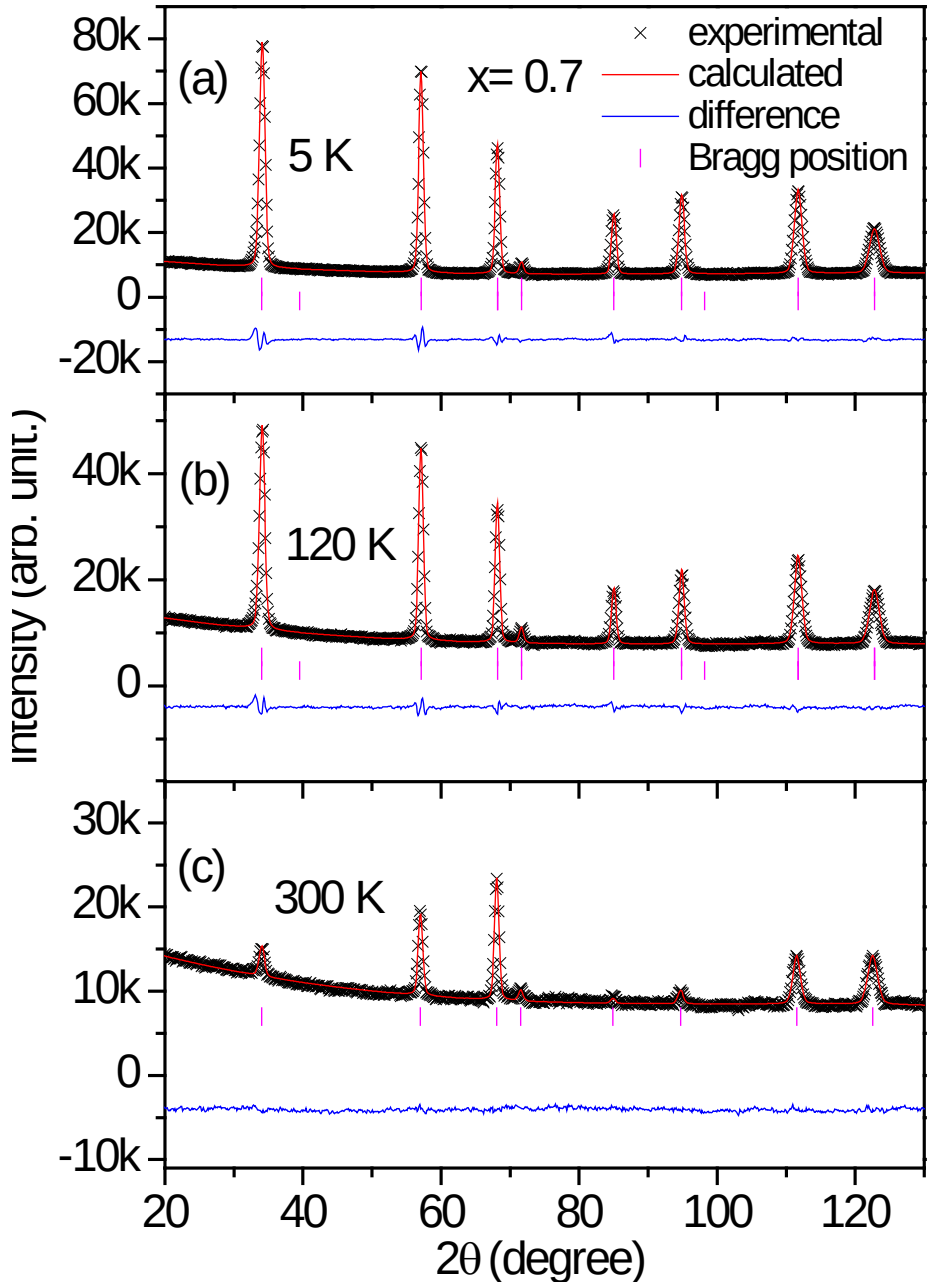

Fig. 4.11. Neutron diffraction patterns of $HoCo_2Mn_{0.7}$ at 5 K below T_{Spin}, 120 K below T_C and paramagnetic-state at 300 K. The black crosses are the experimental Neutron-diffraction data and the red lines represent the Rietveld refined pattern. The difference between the experimental and calculated patterns is shown at the bottom by the blue solid curves. The vertical bars indicate the position of allowed Bragg peaks.

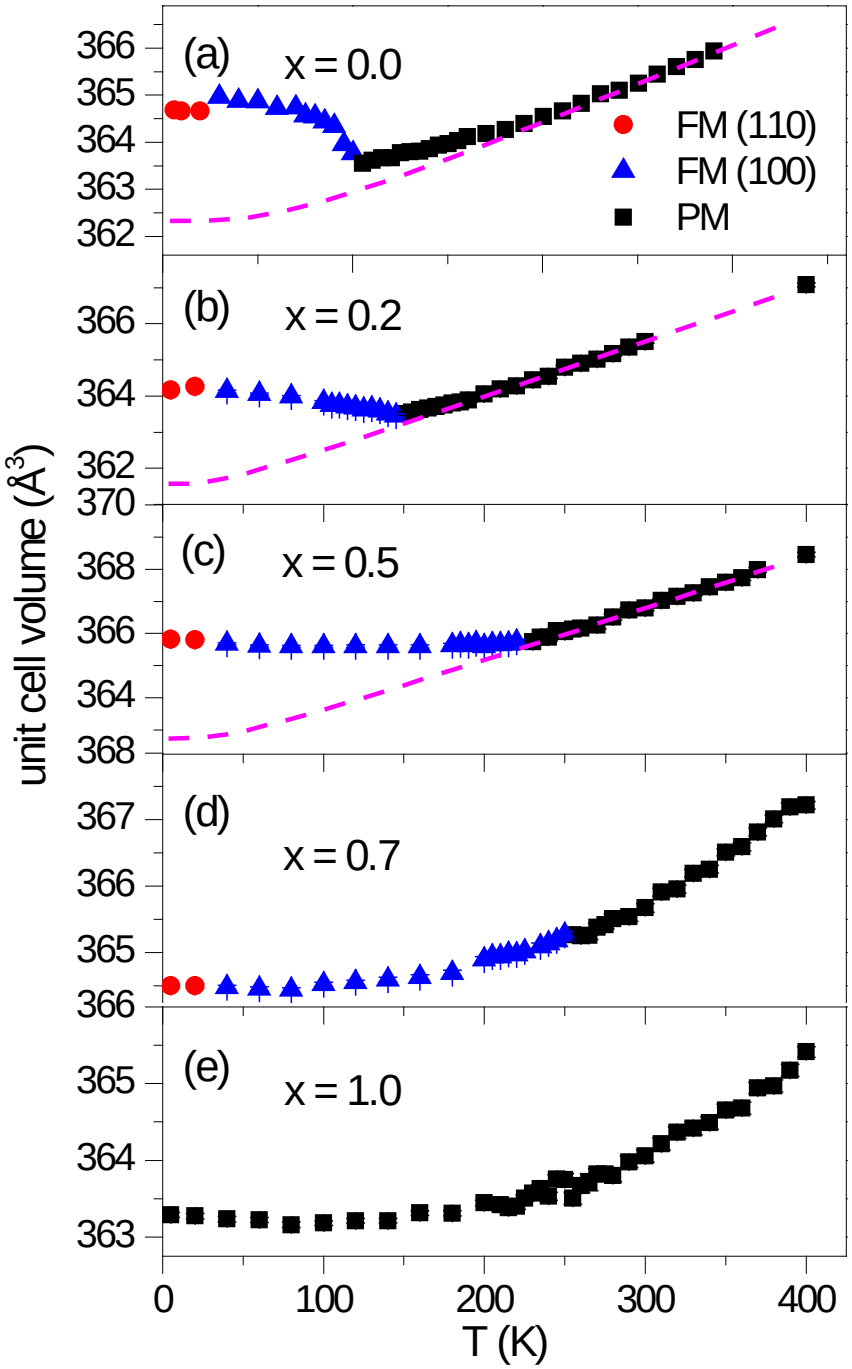

Fig. 4.12. Temperature dependence of unit cell volume for $HoCo_2Mn_x$ compounds with blue dash line estimate based the Debye theory for (b) and the calculated sub-lattice moments at 8a, 16 sites with the total magnetic moment for (c).

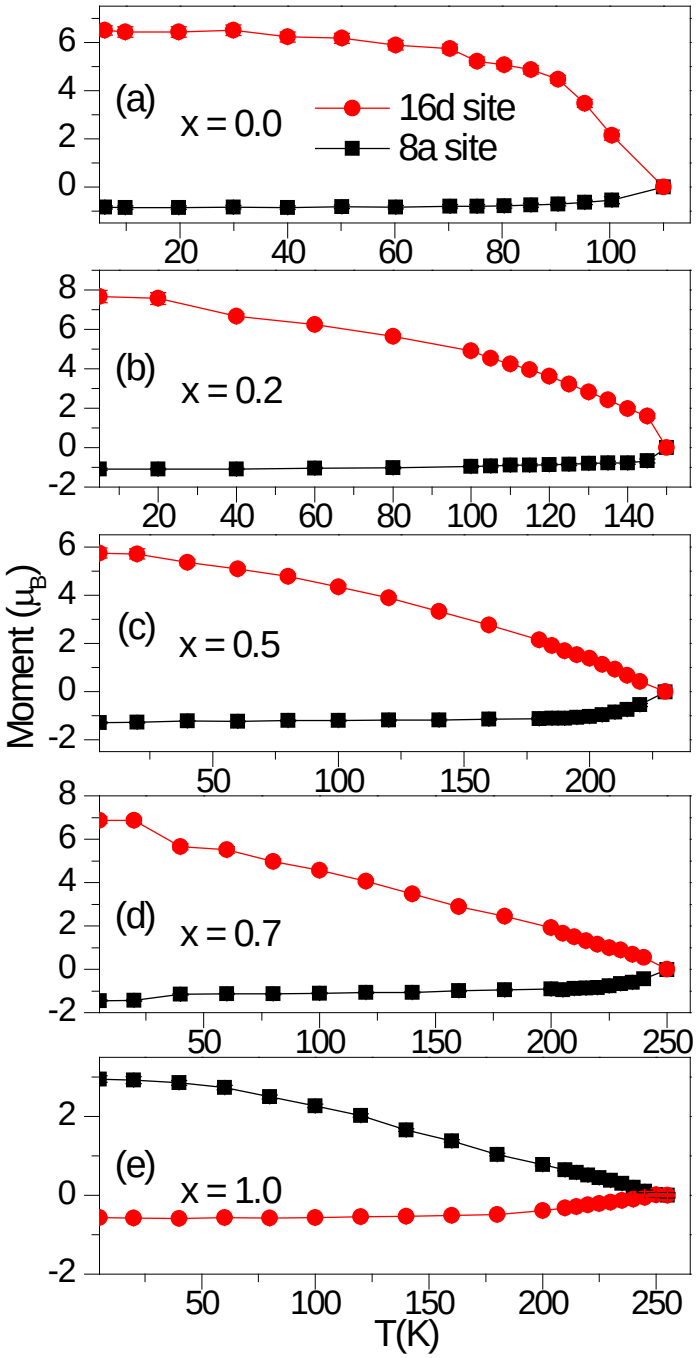

Fig. 4.13. Temperature dependence of the sub-lattice moments at 8a, 16 sites respectively.

4.4 Conclusion

In this work we did a systematic investigation of Mn doping effect on magnetic properties such as magnetic phase transition temperature, saturation magnetization M_S, magnetic entropy change $-\Delta S_M$ and so on. It was found that doping shifted the magnetic phase transition from the first order to the second order which can practically reduce loss in the

refrigeration application. Furthermore with x value increasing from 0.0 to 1.0, T_C increases sharply from 88 K to 253 K while the saturation moment M_S (5 K), coercivity H_C and magnetic entropy change $-\Delta S_M$ decrease. Electronic and phonon contributions to the heat capacity were investigated with density of energy state $N(E_F)$ and Debye temperature θ_D calculated out for x = 0.2, 0.5 and 1.0 respectively. And then detailed critical exponents analysis was done for all the second order transitions, which show the transition of $HoCo_2Mn_{0.2}$ approachs Mean-field theory, while with a little deviation for $HoCo_2Mn_{0.5}$, $HoCo_2Mn_{0.7}$ and $HoCo_2Mn$. Neutron powder diffraction at various temperature shows that doping of Mn reduce the volume effect accompanying PM-FM transition for undoped sample, which is in accordance well with Arrot Plot analysis result. In addition, the refinement results of diffraction pattern show Mn goes to both Co and Ho position in crystal structure. Unusual transformation from strong negative to positive thermal expansion in $HoCo_2Mn_x$ compounds has been detected. Almost zero thermal expansion over a wide temperature range (over 200 K) can be achieved in the compound $HoCo_2Mn_{0.5}$.

CHAPTER 5 INVESTIGATION ON $DyCo_2Mn_x$ (x = 0.1, 0.2, 0.4, 0.6, 1.0) COMPOUNDS

5.1. Introduction

RCo_2 (R = rare earth) series magnetocaloric materials were investigated intensively before due to their various magnetic properties. Normally, at paramagnetic state they display cubic structure with $Fd\bar{3}m$ space group while transform into various structures below Curie temperature T_C depending on the rare earth.[114-116] Co magnetic moment couples parallel or antiparallel respectively with light or heavy rare element moment.[117] The RCo_2 compounds with R = heavy rare earth always exhibit large magnetic entropy change due to their first order transition nature.[118] For example, $ErCo_2$ was reported to have the biggest magnetic entropy $-\Delta S_{max}$ = 38 J kg^{-1} K^{-1} (magnetic field change from 0Oe to 50kOe) followed by $HoCo_2$ (23.2 J kg^{-1} K^{-1})[84], $DyCo_2$ (11.0 J kg^{-1} K^{-1}) and $TbCo_2$ (6.5 J kg^{-1} K^{-1}).[65]

The magnetic property of $DyCo_2$ compound was simply investigated on temperature dependent magnetic moment (M−T) after zero field cooling (ZFC) and field cooling (FC) in 1996.[117] With the high resolution synchrotron development, a tiny crystal structure transformation from cubic to tetragonal structure was found during the magnetic transition from paramagnetism to ferrimagnetism.[13] Except to the research on $DyCo_2$ compound itself, various methods were tried to tune its magnetic properties such as adding external magnetic filed11[9], mechanical pressure,[118] or doping other element such as Ga ($DyCo_{2-x}Ga_x$ (x = 0.0−2.0) series compounds)[11] and so on.

Element doping is a popular method to modify the physical property of the magnetocaloric materials.[61, 84, 120, 121] In this way, rare earth element or transition metal was substituted by other elements so that the magnetic property such as Curie temperature T_C, spontaneous magnetic moment M_S, magnetic entropy change $-\Delta S$ can be tuned through the element doping. In 2002, Wang et al.[59] found a novel Mn doping fashion without substituting either rare earth and transition metal atomics, to form pseudo-ternary compound RNi_2Mn which is isostructure to RNi_2 with $MgCu_2$-type structure ($Fd\bar{3}m$, space group). Subsequently, series pseudo-ternary compounds with different rare earth RNi_2Mn (R = Tb, Dy, Ho, Er) compounds were reported.[51, 70, 113] These work not only exploited a new and efficient method to tune the magnetic property of the RM_2 (M = transition metal) compounds, but also

observed a new and novel structure where Mn elements were added into both rare earth and transition metal elements sites without kicking out the original atomics. Recently, a specific and systematic research on pseudo-ternary series compounds $TbCo_2Mn_x$ (x = 0.0, 0.2 and 0.3) was reported.[112]

So here, we continue the research thinking to investigate $DyCo_2Mn_x$ (x = 0.0, 0.2, 0.4, 0.6 and 1.0) series compounds. As expectation, the Mn doped compounds are pure phase and isostructure to $DyCo_2$ with cubic structure ($Fd\bar{3}m$, space group). A detailed Mn element doping effect on the magnetic property was studied: with Mn doped more from x = 0.0 to 0.6, the Curie temperature increases from 141 K to 295 K while deceases to 268 K for x = 1.0. The values of spontaneous magnetic moment M_S, entropy change $-\Delta S$ decreased monotonously with x value increasing. Abnormally, a huge coercivity H_C = 21170 Oe was observed in $DyCo_2Mn$ compound. The nature of the magnetic transition transforms from first order for $DyCo_2$ to second order after Mn doped. Furthermore, all the second orders were proved approach to Mean field (MF) Theory with critical exponents $\beta \approx 0.5$, $\gamma \approx 1.0$, and $\delta \approx 3.3$ calculated out by Kouvel-Fisher plot, critical isotherm analysis and Arrott-Noaks plot methods. Synchrotron measurements at various temperatures were finally performed to find that the structure transfer from cubic to tetragonal for $DyCo_2$ and $DyCo_2Mn_{0.2}$, while there is no obvious structure transition near the Curie temperature for $DyCo_2Mn_{0.4}$, $DyCo_2Mn_{0.6}$ and $DyCo_2Mn$.

5.2. Experimental Techniques

The polycrystalline $DyCo_2Mn_x$ compounds with x = 0.0, 0.2, 0.4, 0.6 and 1.0 were prepared by arc melting the constituent elements of 99.9 % purity under argon atmosphere. The prepared ingots were wrapped in tantalum foil and sealed in quartz glass tubes under vacuum and annealed at 1173 K for 7 days and then quenched into ice water. All the samples were checked with x-ray powder diffraction at room temperature using a PANalytical diffractometer with CuKα radiation. The dc magnetisation measurements were performed using a Quantum Design physical properties measurement system (PPMS) from 5 K to 350 K. The crystal structure transitions were also examined by the synchrotron x-ray powder diffraction at the Australian Synchrotron using a wavelength of 0.7746 Å at temperatures from 90 K to 450 K.

5.3. Results and Discussion

5.3.1 Magnetic Phase Transition

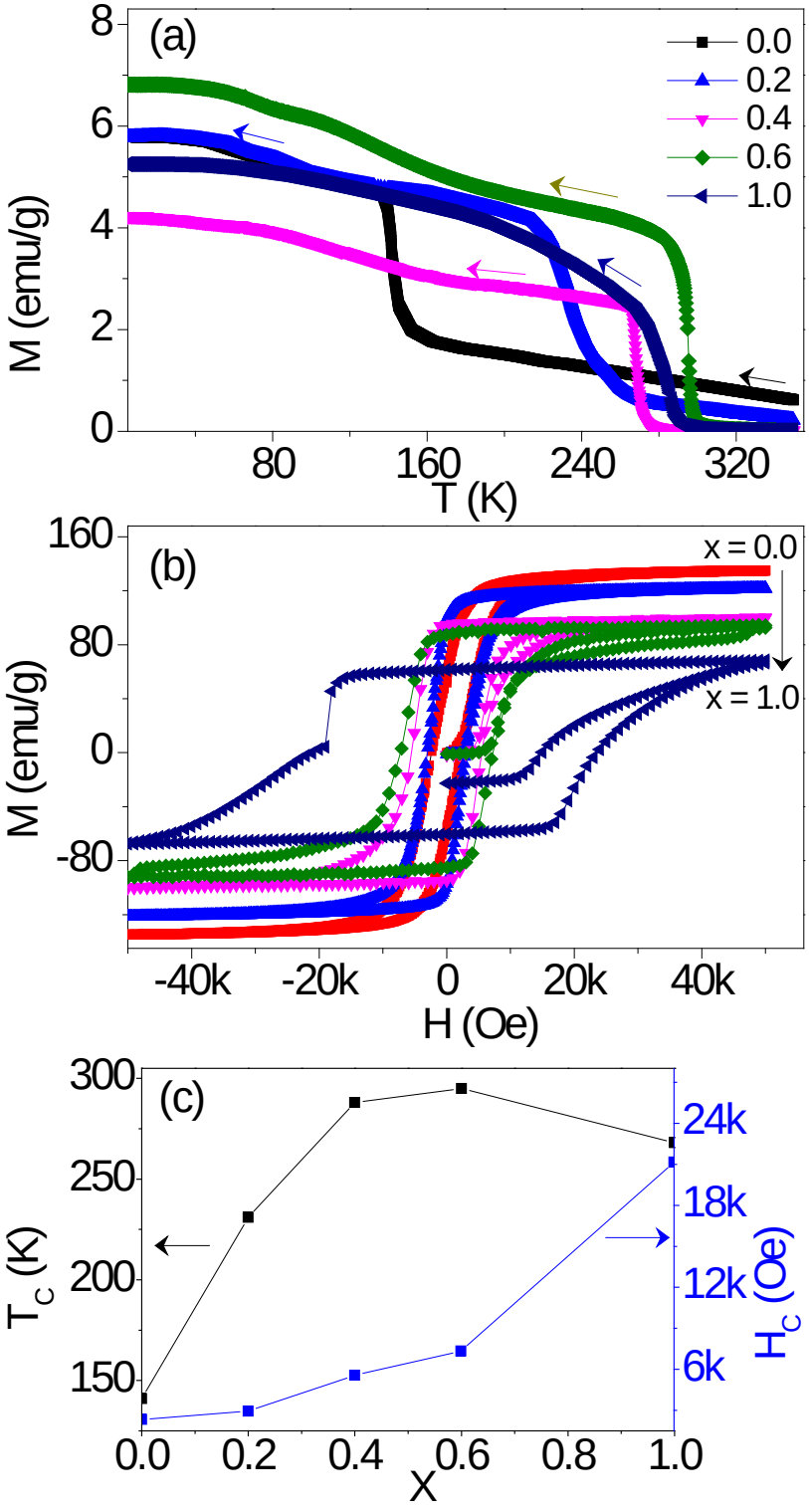

Fig. 5.1. (a) Temperature dependent magnetization after field cooling at the field of H = 100 Oe for $DyCo_2Mn_x$ (x = 0.0, 0.2, 0.4, 0.6 and 1.0). The inset shows the Curie temperature T_C in dependence on the x value. (b) Hysteresis loops at 5 K for each sample. (c) The tendency of the T_C and H_C at 5 K in dependence on the x value.

The magnetization moment versus temperature (M-T) curve for each sample is shown in Fig. 5.1(a). It can be seen that there is a sharp drop near each Curie temperature T_C during the magnetic-state transition from Ferrimagnetism to Paramagnetism (FM-PM). The visible tendency of T_C depending on the x value can be seen in Fig. 5.1(c), where T_C value increases from 141 K to 295 K with x value increases from 0.0 to 0.6, while deceases to 268 K for x = 1.0. Abnormally, an extreme huge coercivity H_C = 21170 Oe is detected for $DyCo_2Mn$ shown in Fig. 5.1(b), after a monotone increasing of H_C value from H_C = 2344 Oe for $DyCo_2$. It can be understood that with the more Mn doped, the anisotropy of the compound being enhanced reflecting in the increased coercivity value. Besides, as marked by the arrow in the right corner in Fig. 5.1(b), the spontaneous magnetic moment M_S decreases with the increasing x value: from 136 emu/g for x = 0.0 to 67 emu/g for x = 1.0. The decrease value of M_S can be explained that Mn atoms carry magnetic moment which antiferromagnetically couple with Dy-subblattice moment.[117]

The magnetization-field isotherms for each sample are shown in Fig. 5.2. The gradual transformation from curve line to straight line near T_C indicates the FM-PM transition process, corresponding to the sharp drop point in $M-T$ curves in Fig. 5.1(a). Meanwhile, the isotherms line during the field increasing and decreasing processes are almost overlap, which means hysteresis loss for each sample is negligible, which is favourable to magneto refrigerant performance. According to the isotherms in Fig. 5.2, the Arrott Plot can be deduced out as shown in Fig. 5.3. Based on the Banerjee theory,[28] the S-shape curve of the Arrott Plot for $DyCo_2$ is expected a negative contribution from the higher order term in Landau free energy expansion,[122] which means that the magnetic phase transition belongs to first order. While, the L-shape of the isotherms indicates second order transition for the Mn doped samples as shown in Figs. 5.3(b), 3(c), 3(d), 3(e), and 3(f). The further critical exponent analysis on the nature (3D Heisenberg model, Mean field (MF) Theory or 3D Ising Model) of all the second order transitions will be expanded in **Sec. 5.3.3**. Here, through the standard Arrott Plot we can elementarily conclude that the nature of magnetic transition in $DyCo_2Mn_{0.2}$, $DyCo_2Mn_{0.4}$ and $DyCo_2Mn_{0.6}$ approach to Mean-Field theory because of the

consecutive parallel lined of the M^2 *vs H/M* and high field Arrott Plot line near T_C almost across through the origin.[123, 46] So for these samples, the critical exponents β, γ and δ can be calculated out directly using standard Arrott Plot based on the Eqs. 5.2, 5.3, and 5.4 respectively. While for $DyCo_2Mn$ as shown in Fig. 5.3(f), it is obvious that the high field Arrott Plot line near T_C is a little deviation to the origin, which means Mean-field theory is not suitable.[46] So modified Arrott plot using self-consistent method will be performed according to Eq. 5.8, which will be specifically discussed in **Sec. 5.3.3**.

5.3.2 Magnetocaloric Effect

To determine the magnetic refrigeration efficient in these compounds, magnetic entropy changes $-\Delta S_M$ is a key parameter, which can be calculated out according to magnetization-field isotherms at various temperatures based on the standard Maxwell relationship:

$$\Delta S_M(T,H) = \int_0^{H^{max}} \left(\frac{\partial M(H,T)}{\partial T}\right)_H dH \tag{5.1}$$

The result of the magnetic entropy change in dependence on the various temperatures are shown in Fig. 5.4 for each sample. It can be seen that all the peaks $-\Delta S_{max}$ exist near the Curie temperature T_C for each compound after respectively experiences five different magnetic field changes (0 Oe−10 kOe, 0 Oe−20 kOe, 0 Oe−30 kOe, 0 Oe−40 kOe and 0 Oe−50 kOe). The *x* dependent value of $-\Delta S_{max}$ is depicted by Fig. 5.4(f): with the *x* value increasing, the total tendency of the $-\Delta S_{max}$ value is decreasing from 8.85 J kg^{-1} K^{-1} for $DyCo_2$ to 1.57 J kg^{-1} K^{-1} for $DyCo_2Mn$, while with a small fluctuation from 2.39 J kg^{-1} K^{-1} for $DyCo_2Mn_{0.4}$ to 2.50 J kg^{-1} K^{-1} for $DyCo_2Mn_{0.6}$. Besides, a broad operation temperature range displays in Fig. 5.4(e) for $DyCo_2Mn$. The specific tendency line is drawn in Fig. 5.4(f): the operation temperature T_{ope} increases sharply from 110 K-170 K for $DyCo_2$ to 140 K-307 K for $DyCo_2Mn$. Here we define the operational temperature T_{ope} as the middle range between two points where the value of *dS/dT* is close to zero below and above Curie temperature.

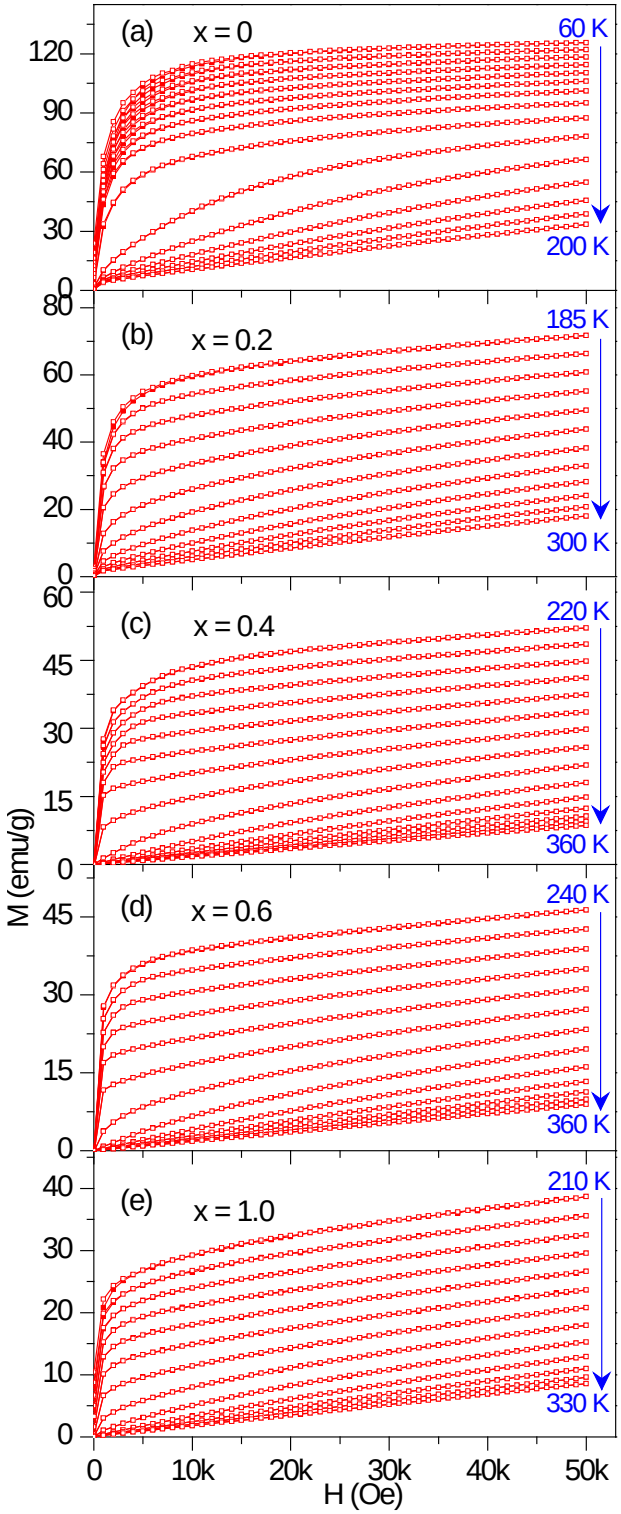

Fig. 5.2. Isothermal magnetization versus magnetic field at a range of temperatures (ΔT = 10 K) near T_C in both increasing field (solid red symbol) and decreasing field sweeps (hollow red symbols) for (a) $DyCo_2$, (b) $DyCo_2Mn_{0.2}$, (c) $DyCo_2Mn_{0.4}$, (d) $DyCo_2Mn_{0.6}$ and (e) $DyCo_2Mn$.

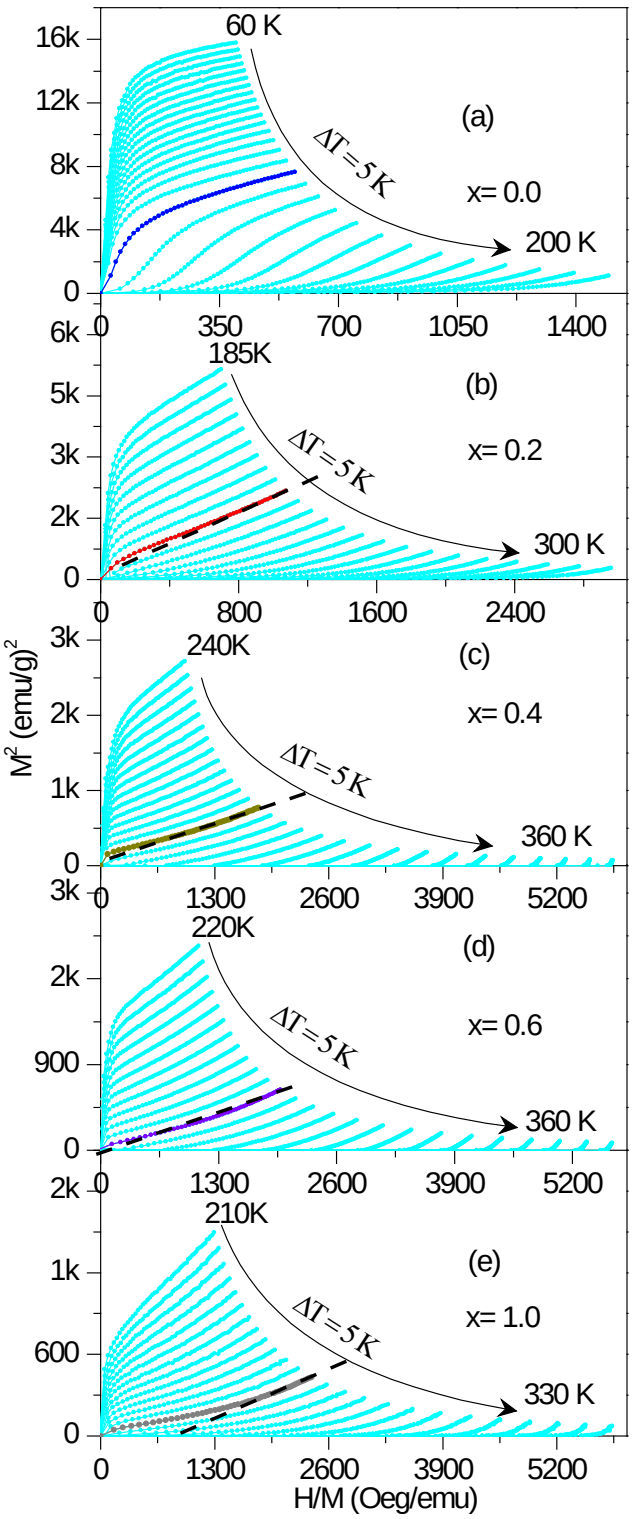

Fig. 5.3. Arrott plots: isotherms of M^2 *vs* H/M for decreasing field at various temperatures around T_C of for (a) $DyCo_2$, (b) $DyCo_2Mn_{0.2}$, (c) $DyCo_2Mn_{0.4}$, (d) $DyCo_2Mn_{0.6}$ and (e) $DyCo_2Mn$. The dash lines at T_C is the high field data lines.

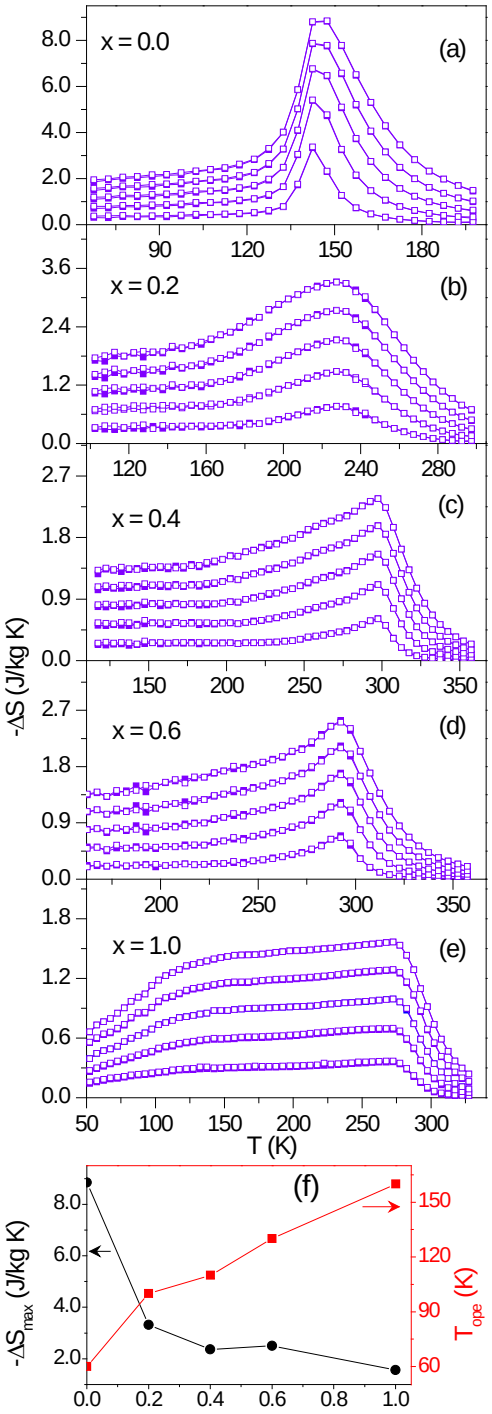

Fig. 5.4 The magnetic entropy changes $-\Delta S$ in dependent on various temperatures under five different magnetic fields changes 0-10kOe, 0-20kOe, 0-30kOe, 0-40k Oe and 0-50kOe respectively corresponding to each curve from bottom to top, for (a) $DyCo_2$, (b) $DyCo_2Mn_{0.2}$, (c) $DyCo_2Mn_{0.4}$, (d) $DyCo_2Mn_{0.6}$ and (e) $DyCo_2Mn$. (valid solid icons for increasing field while the hollow ones for the decreasing field,) (f) x value dependent maximum magnetic entropy changes $-\Delta S_{max}$ for a change of 0-50kOe and operation temperature T_{ope} respectively during FM-PM transition.

5.3.3 Critical Exponents Analysis

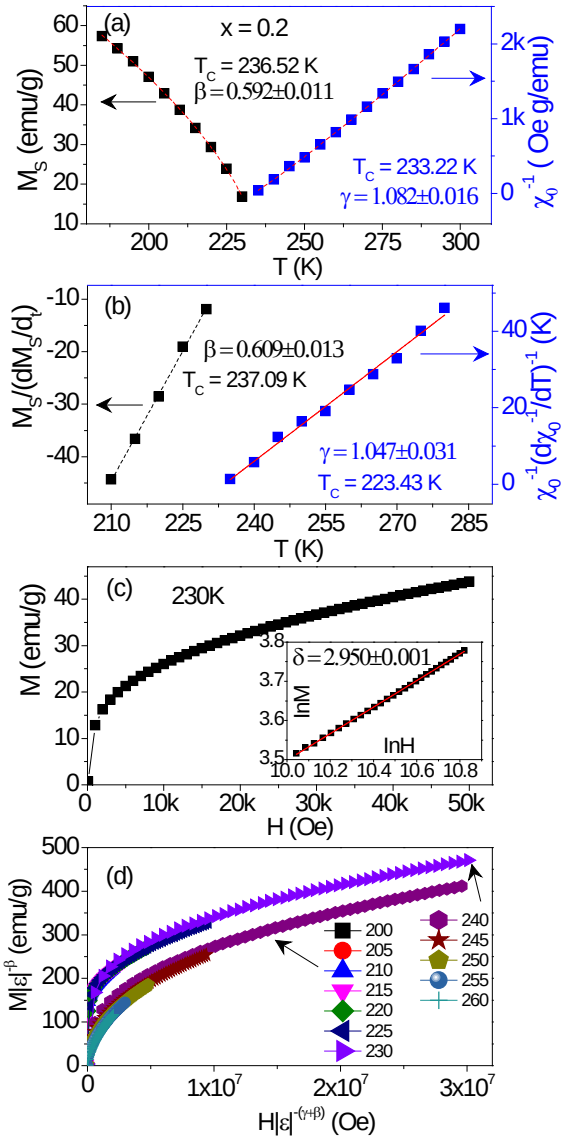

Fig. 5.5. Critical exponent analysis of $DyCo_2Mn_{0.2}$ for (a) Temperature dependent spontaneous magnetization M_S *(T)* and the inverse initial susceptibility χ^{-1}(dash lines are nonlinear-fitted to Eqs. 5.2 and 5.3, (b) Kouvel–Fisher plot for the spontaneous magnetization $M_S(T)$ and the inverse initial susceptibility χ^{-1}(dash lines are linear-fitted to Eqs. 5.5 and 5.6, (c) Critical isotherm of *M vs H* close at the Curie temperature T_C = 230 K. Inset shows the same on log-log scale and the red dash line is the linear fitting following Eq. 5.4. The critical exponent δ is just the slope value of the linear fit, (d) Scaling plots indicating two branches of universal curves below and above T_C.

After distinguishing the first order for $DyCo_2$ from second order for $DyCo_2Mn_x$ (x = 0.2, 0.4, 0.6, and 1.0), we further investigate the nature of the second order transition (3D Heisenberg

model, Mean-field theory or 3D Ising model),[103, 104] the values of the critical exponents β, γ and δ are the criterions which can be calculated out according to scaling hypothesis using the following equations:[123]

$$M_S(0,T) = M_0(-\varepsilon)^{\beta},\ \varepsilon < 0 \tag{5.2}$$

$$\chi_0^{-1}(0,T) = (h_0/M_0)(\varepsilon)^{\gamma} \tag{5.3}$$

$$M(H, T_C) = A_0(H)^{1/\delta} \tag{5.4}$$

Where $\varepsilon = (T-T_C)/T_C$, M_S is spontaneous magnetization below T_C, χ_0^{-1} is initial susceptibility above T_C and $M(H)$ is magnetic moment at T_C. M_0, h_0/M_0 and A_0 are constants of the critical amplitudes. $M_S(T)$ *and* $\chi_0^{-1}(T)$ is the intercept of Y-axis and X-axis respective from the high field data of the Arrott plot as shown the colour dash lines in Fig. 5.3.[123] As discussed in Fig. 5.3, the critical exponents of $DyCo_2Mn_{0.2}$, $DyCo_2Mn_{0.4}$ and $DyCo_2Mn_{0.6}$ can be directly calculated out using Arrott plot through nonlinear fitting the M_S-T and χ_0^{-1}–T curves as shown in Figs. 5.5(a), 6(a) and 7(a). Actually, the Kouvel-Fisher method can be used to obtain the more precise value of β and γ through linear fitting $M_S/(dM_S(T)/dT)$–T and $\chi_0^{-1}(T)/(d\chi_0^{-1}(T)/dT)$–T curves shown in Figs. 5.5(b), 6(b) and 7(b), according to the counterpart equations deduced from Eqs. 5.2 and 5.3 respectively: [40]

$$\frac{M_S(T)}{dM_S(T)/dT} = \frac{T-T_C}{\beta} \tag{5.5}$$

$$\frac{\chi_0^{-1}(T)}{d\chi_0^{-1}(T)/dT} = \frac{T-T_C}{\gamma} \tag{5.6}$$

Finally, the value the δ can be obtained as shown in Figs. 5.5(c), 5.6(c) and 5.7(c) according to Eq. 5.4. Based on the fact that all the calculated value of the critical exponents for $DyCo_2Mn_{0.2}$, $DyCo_2Mn_{0.4}$ and $DyCo_2Mn_{0.6}$ are close to the values of β = 0.5, γ = 1.0 and δ = 3.0 (which are theoretical critical based on the mean field interaction model for long range ordering), we can conclude that long range interactions dominate the critical behavior around T_C.

As for $DyCo_2Mn$, due to its Arrot plot line near T_C deviates from the origin, mean-field theory is not valid.[70] So modified Arrott plot were used on the basis of Arrott-Noaks equation:[43]

$$\left(\frac{H}{M}\right)^{1/\gamma} = \frac{a(T-T_C)}{T_C} + bM^{1/\beta} \quad (5.7)$$

Where a and b is constants. And based on Eq. 5.7, self-consistent method[44, 45] was used to obtain the optimum values of β and γ with repeated process: the initial values of $M_S(T)$ and $\chi_0^{-1}(T)$ were derived from the high field Arrott plot, and then β and γ were calculated according to Eqs. 5.2 and 5.3, and then the values of β, γ were used to build a new modified Arrott plot. The whole process was repeated several times until iteration converge to the optimum final values when the high field modified Arrott plot line at Curie temperature pass through the origin as shown in Fig. 5.8(a).

Finally, to justify if all the calculated critical exponents are correct or not, the function *M (H, ε)* was used according to the scaling hypothesis:[47]

$$M(H,\varepsilon) = \varepsilon^{\beta} f \pm (H/\varepsilon^{\beta+\gamma}) \quad (5.8)$$

Where after value of β and γ were put in, the universal curves $M \mid \varepsilon|^{-\beta}$ vs $H \lfloor\varepsilon\rfloor^{-(\beta+\gamma)}$will collapse into two branches respectively for temperatures above and below T_C as shown in Fig. 5.5, Fig. 5.6, Fig. 5.7 and Fig. 5.8, which means that all our calculations of exponent and T_C are exact and unambiguous. The detailed critical exponents value for each sample can be seen in Table 5.1.

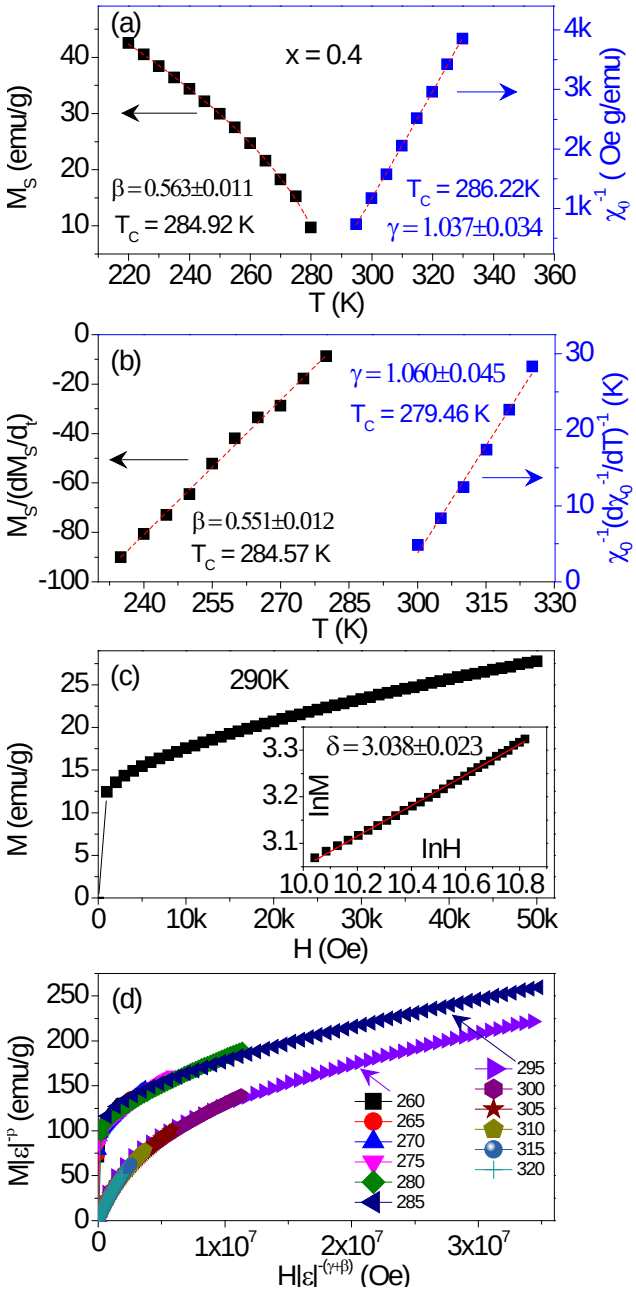

Fig. 5.6 Critical exponent analysis of $DyCo_2Mn_{0.4}$ for (a) Temperature dependent spontaneous magnetization $M_S(T)$ and the inverse initial susceptibility χ^{-1}(dash lines are nonlinear-fitted to Eq. 5.2 and 5.3, (b) Kouvel–Fisher plot for the spontaneous magnetization $M_S(T)$ and the inverse initial susceptibility χ^{-1}(dash lines are linear-fitted to Eq. 5.5 and 5.6, (c) Critical isotherm of M vs H near the Curie temperature T_c = 288 K. Inset shows the same on log-log scale and the red dash line is the linear fitting following Eq. 5.4. The critical exponent δ is just the slope value of the linear fit. (d) Scaling plots indicating two branches of universal curves below and above T_C.

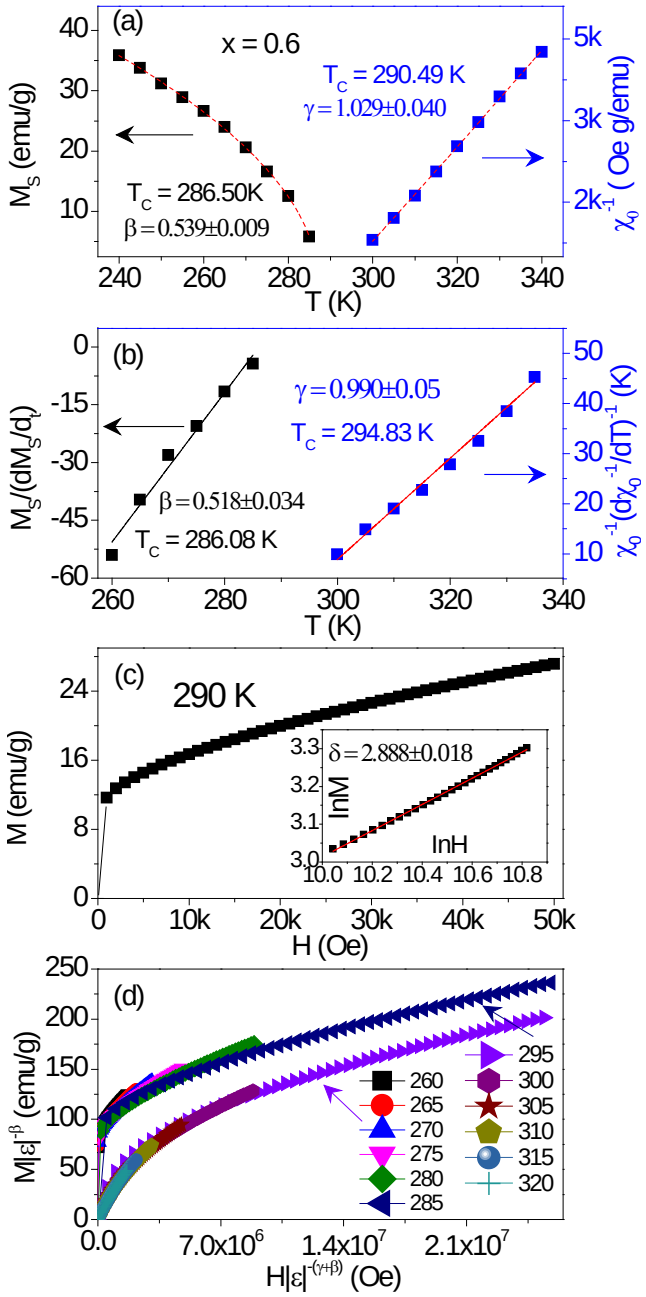

Fig. 5.7. Critical exponent analysis of $DyCo_2Mn_{0.6}$ for (a) Temperature dependent spontaneous magnetization $M_S(T)$ and the inverse initial susceptibility χ^{-1} (dash lines are nonlinear-fitted to Eq. 5.2 and 5.3, (b) Kouvel–Fisher plot for the spontaneous magnetization $M_S(T)$ and the inverse initial susceptibility χ^{-1}(dash lines are linear-fitted to Eq. 5.5 and 5.6, (c) Critical isotherm of M *vs* H near the Curie temperature T_c = 290 K. Inset shows the same on log-log scale and the red dash line is the linear fitting following Eq. (4). The critical exponent δ is just the slope value of the linear fit. (d) Scaling plots indicating two branches of universal curves below and above T_C.

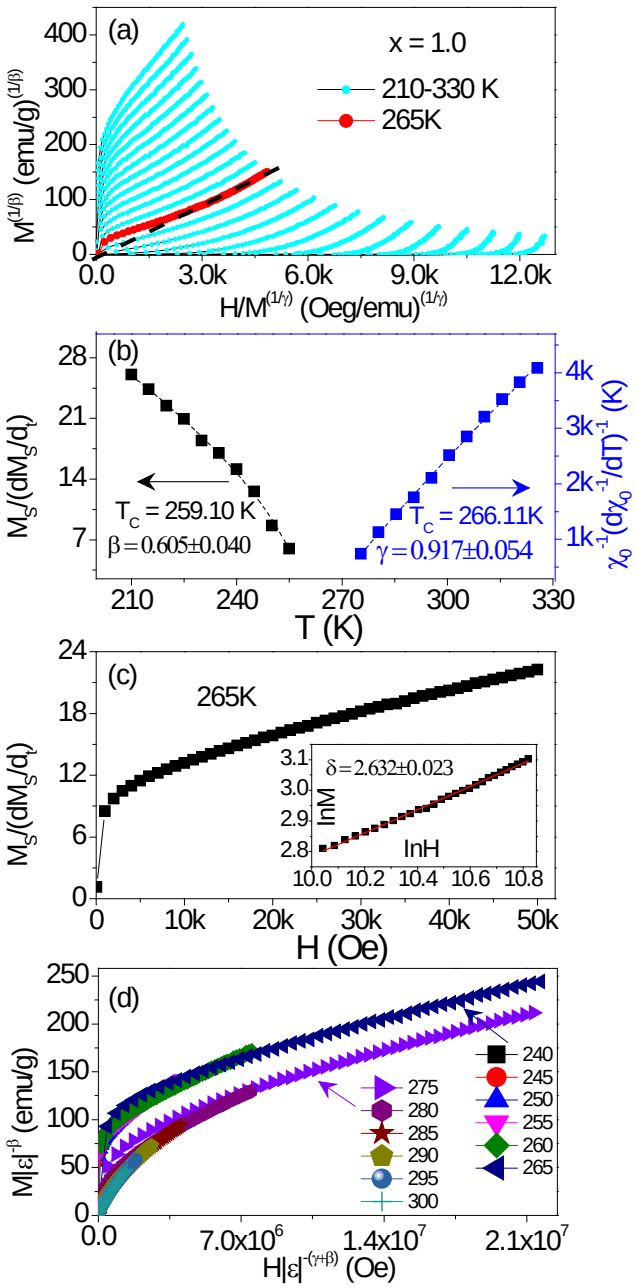

Fig. 5.8 Critical exponent analysis of $DyCo_2Mn$ for (a) Temperature dependent spontaneous magnetization $M_S(T)$ and the inverse initial susceptibility χ^{-1} (dash lines are nonlinear-fitted to Eqs. 5.2 and 5.3, (b) Kouvel–Fisher plot for the spontaneous magnetization $M_S(T)$ and the inverse initial susceptibility χ^{-1}(dash lines are linear-fitted to Eq. 5.5 and 5.6, (c) Critical isotherm of M vs H near the Curie temperature T_c = 268 K. Inset shows the same on log-log scale and the red dash line is the linear fitting following Eq. 5.4. The critical exponent δ is just the slope value of the linear fit. (d) Scaling plots indicating two branches of universal curves below and above T_C.

5.3.4 Crystal Structure Transition: Synchrotron Powder Diffraction Pattern Analysis

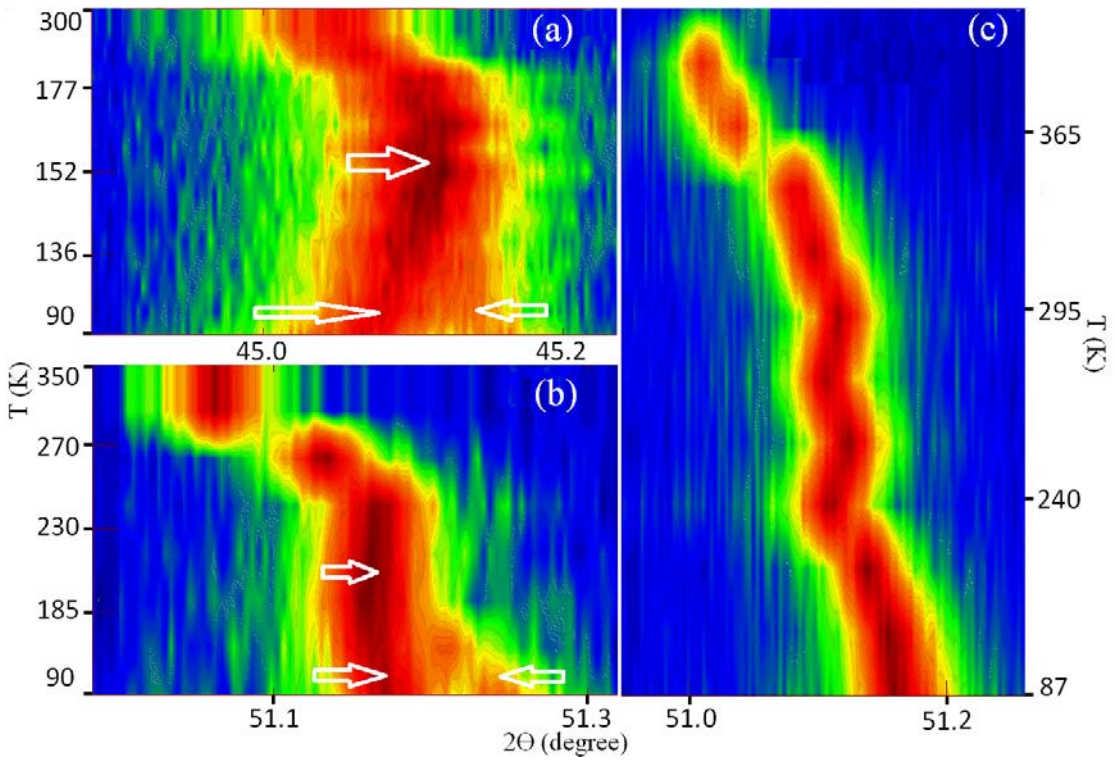

Fig. 5.9. Synchrotron x-ray Bragg diffraction patterns at various temperatures display the [800] peak splits into two small peaks ([800], [008]) as fingered by the white arrows, after cooling down below T_C for (a) $DyCo_2$, (b) $DyCo_2Mn_{0.2}$ and (c) for $DyCo_2Mn_{0.4}$.

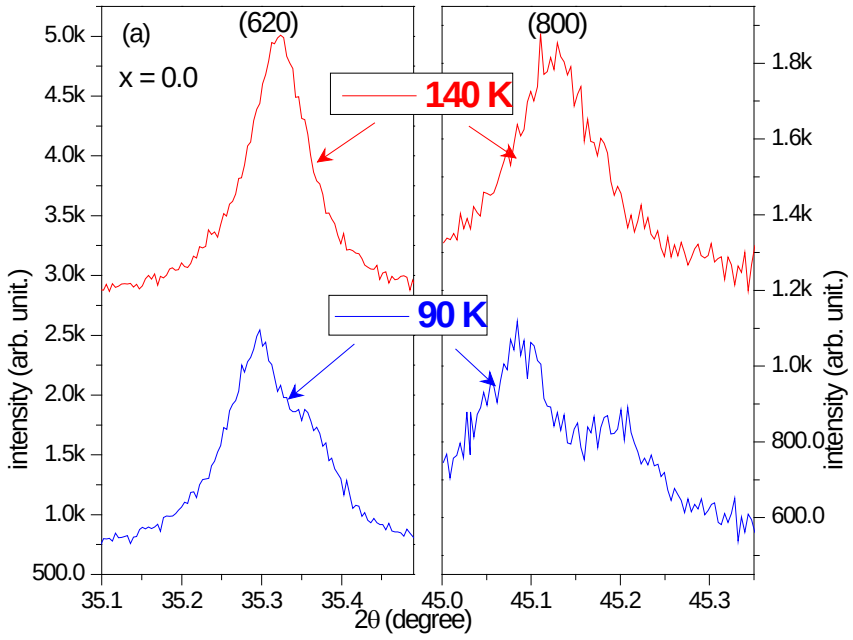

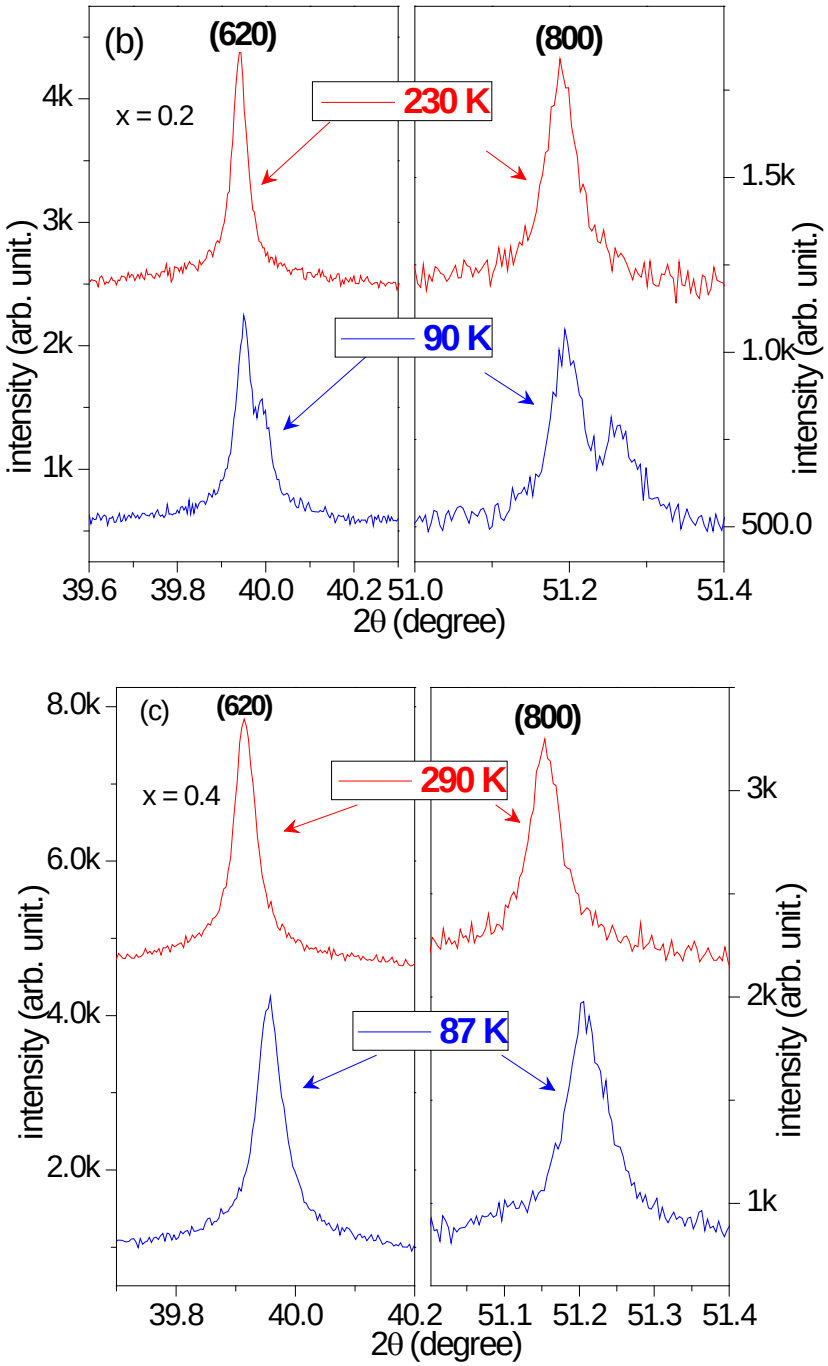

Fig. 5.10 The amplified peaks ([620] and [800]) splitting transformation for $DyCo_2$ (a) $DyCo_2Mn_{0.2}$ for (b) and $DyCo_2Mn_{0.4}$ for (c).

Synchrotron x-ray diffraction experiment at various temperatures was performed to clarify the crystal structure transition during the magnetic state transition PM−FM. Here we found that only in $DyCo_2$ and $DyCo_2Mn_{0.2}$ there is peak splitting from [800] into [800] and [008], which can be observed more directly through the Synchrotron x-ray Bragg diffraction patterns and the amplified peaks shown in Fig. 5.9 and Fig. 5.10. (the peak [620] also splits,

the same as [800] splitting) As a comparison, the pattern of $DyCo_2Mn_{0.4}$ was drawn as shown in Fig. 5.9(c) and Fig. 5.10 (c) respectively without peak splitting for both peak [620] and [800].

As for $DyCo_2Mn_{0.4}$, $DyCo_2Mn_{0.6}$ and $DyCo_2Mn$ compounds, no peak was found splitting, which we think there is no obvious space group transformation keeping still at cubic structure with the $Fd\bar{3}m$ space group. The refinement was done to obtain the lattice parameter variation with a range of temperatures crossing the Curie temperature as shown in Figs. 5.11-5.13. In order to compare directly between the lattice parameters of the cubic structure ($Fd\bar{3}m$) and the tetragonal structure (*I41/amd*) at the transition, we modify the tetragonal structure lattice parameters by using $\sqrt{2} \times a$ as shown in Figs. 5.11 and 5.12 for $DyCo_2$ and $DyCo_2Mn_{0.2}$ respectively. The dash lines distinguish the tetragonal, cubic and the mixture of both structures.

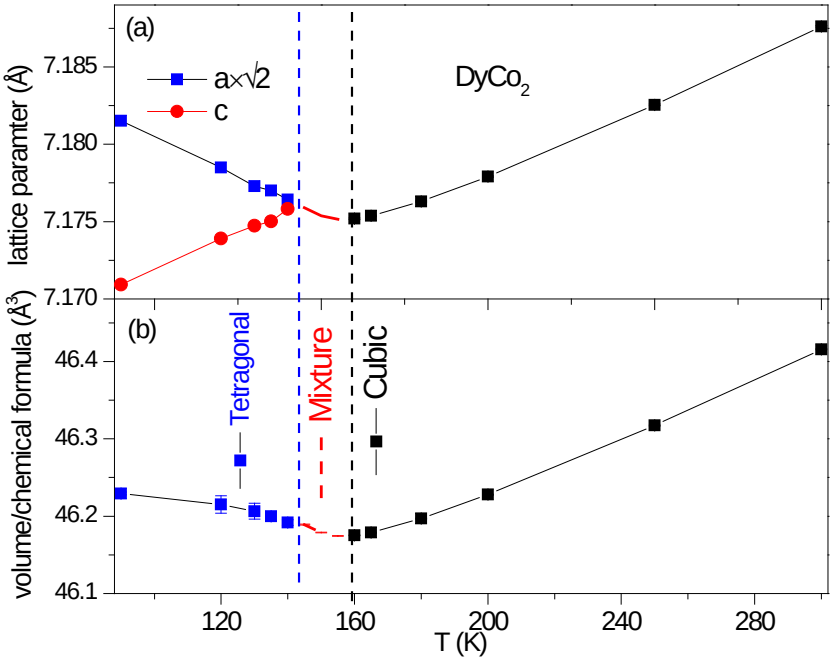

Fig. 5.11. Temperature dependence for $DyCo_2$ of (a), lattice parameters, (b) volume per chemical formula. Between the two dashed lines is the phase transition region with possible both cubic and tetragonal structure apparently present.

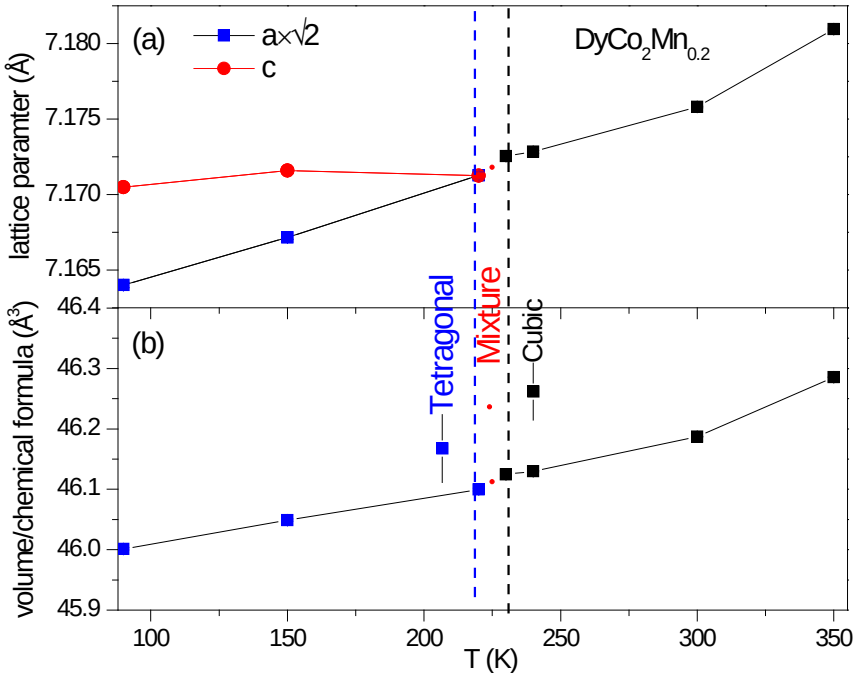

Fig. 5.12. Temperature dependence for $DyCo_2Mn_{0.2}$ of (a), lattice parameters, (b) volume per chemical formula. Between the two dashed lines is the phase transition region with possible both cubic and tetragonal structure apparently present.

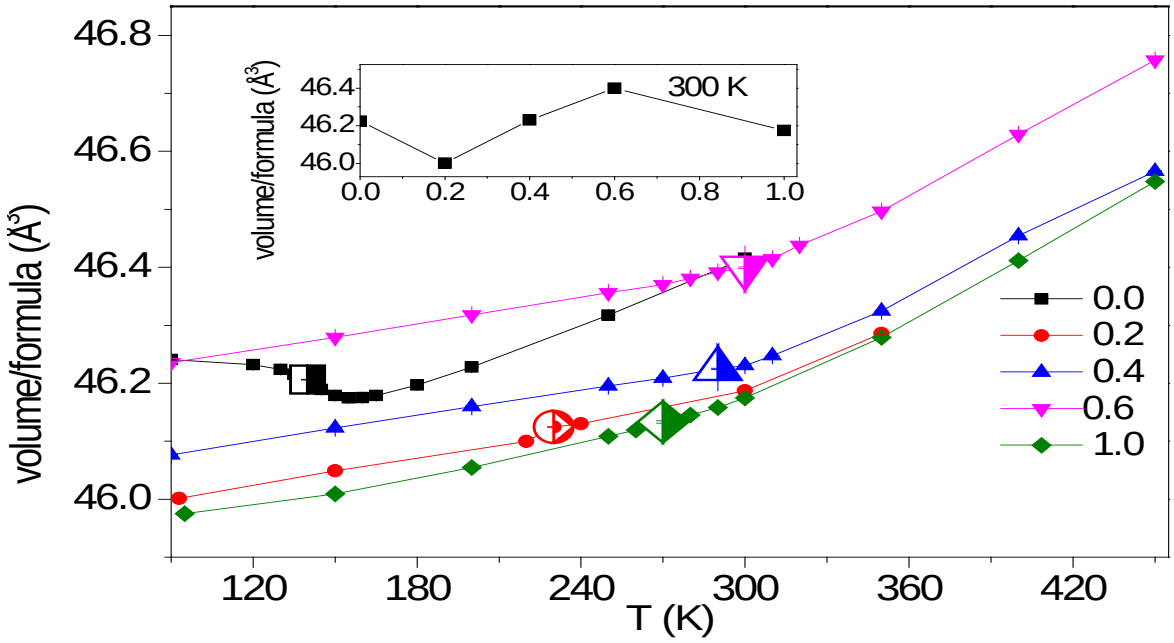

Fig. 5.13 The volume various with the temperatures $DyCo_2Mn_x$ compounds. The larger half solid symbol is the Curie temperature point for each sample. The inset shows the volume variation with the *x* value at 300 K.

From Fig. 5.13， we can see that although there is no abrupt drop in the lattice parameter versus temperature line, an inflection point (marked by the half solid colour symbols) exhibit at the Curie temperature for each sample. As for $DyCo_2$ compound, there is a strong magnetovolume effect. It proves that the magnetic state transition is synchronized with the crystal structure transition. The volume variation with the *x* value at 300 K is depicted by the inset in Fig. 5. 13, where we can see that the volume tendency displays fluctuation with the *x* value increasing. The atomic occupation ratio was obtained through refinement as shown in Table 5.2.

5.4. Conclusion

Single phase $DyCo_2Mn_x$ series compounds were synthesised and systematically investigated. Firstly, the effects of Mn doping on the magnetic properties were specifically discussed: with the more Mn doped, the value of H_C at 5 K increases monotonously from 2344 Oe for $DyCo_2$ to 21170 Oe for $DyCo_2Mn$, while with sharp decreases of spontaneous magnetic moment M_S and magnetic entropy change $-\Delta S$. However, after a consecutive increase of the Curie temperature value with the *x* value increasing, there is a little bit decrease for $DyCo_2Mn$. The nature of the magnetic transition transforms from first order transition for $DyCo_2$ to second order transition for Mn doped compounds. Further analysis of the critical exponents shows that all the second order transitions belong to Mean-field theory, although $DyCo_2Mn$ deviates a little. Finally, synchrotron powder diffraction measurements were performed, proving that the magnetic state transition is simultaneous with the crystal structure transformation.

Table 5.1 Deduced critical exponents β, γ and δ for $DyCo_2Mn_x$ (x = 0.2, 0.4, 0.6 and 1.0) compounds along with standard critical exponents of three standard theories: 3D Heisenberg model, Mean field (MF) Theory and 3D Ising Model

Composition		Technique	β	γ	δ
$DyCo_2Mn_x$	x = 0.2	Kouvel-Fisher method	0.61±0.013	1.047±0.031	2.950±0.001
	x = 0.4		0.551±0.012	1.060±0.045	3.038±0.023
	x = 0.6		0.518±0.034	0.990±0.050	2.888±0.018
	x = 1.0		0.605±0.040	0.917±0.054	2.632±0.023
3D Heisenberg model		Theory	0.365	1.386	4.80
Mean field (MF) Theory		Theory	0.500	1.000	3.00
3D Ising Model		Theory	0.325	1.241	4.82

Table 5.2 Atomic (Dy, Co and Mn) occupancy in cubic and tetragonal structure respectively.

x	Cubic ($Fd\bar{3}m$)				Tetragonal (I41/amd)			
	8a		16d		4a		8d	
	Dy	Mn	Co	Mn	Dy	Mn	Co	Mn
0	100.00%	0.00%	100.00%	0.00%	100.00%	0.00%	100.00%	0.00%
0.2	93.76%	6.24%	93.76%	6.24%	93.76%	6.24%	93.76.00%	6.24%
0.4	88.24%	11.76%	88.24%	11.76%	none			
0.6	83.33%	16.67%	83.33%	16.67%				
1.0	75.00%	25.00%	75.00%	25.00%				

CHAPTER 6 INVESTIGATION OF $TbY_xMn_2Ge_2$ (x = 0, 0.1, 0.2) COMPOUNDS

6.1. Introduction

Since the discovery in 1997 of a giant magnetocaloric effect (GMCE) originating from a discontinuous first order magnetic transition in $Gd_5Si_2Ge_2$,[22, 124] room-temperature magnetic refrigeration based on the magnetocaloric effect (MCE) has attracted significant attention due to its energy efficiency and environment friendly in comparison with conventional gas compression-expansion refrigeration.[125] A number of materials which exhibit giant magnetic entropy changes at magnetic transitions have been investigated, including $MnFeP_{0.45}As_{0.55}$,[126] $MnAs_{1-x}Sb_x$,[127] Ni-Mn-Sn-based alloys,[128] Ni-Mn-Ga,[129, 130] and $La(Fe,Si)_{13}$.[131] The key features of these systems are the temperature- and magnetic field-induced first-order magneto-structural or magneto-elastic phase transitions. Given these promising developments, magnetic materials which exhibit a large magnetocaloric effect have been studied extensively, both experimentally and theoretically, over the past two decades with the overall aim of increasing the efficiency of magnetic refrigeration techniques.[132, 133] While a key focus is exploration of materials that exhibit pronounced magnetocaloric effect at room temperature, materials that operate in the low temperature region are also useful in fields such as gas liquefaction or attaining millikelvin for experimental research facilities. However, so far only a few materials such as $GdLiF_4$, GdF_3 and $Gd_3Gd_5O_{12}$ are used commercially. [134] As reflected by the increase in exploration of materials which exhibit a large MCE below room temperature,[133-136] the search for materials which exhibit large magnetocaloric effects over the hydrogen and natural gas liquefaction temperature ranges are also important for exploring potential applications.

Some RT_2X_2 compounds (R = rare earth, T = transition metal, and X = Si or Ge) have been found to exhibit large MCE values with small hysteresis losses near their low magnetic transition temperatures.[135-139] For example, the magnetic entropy values of RNi_2Si_2 (R = Dy, Ho, Er) compounds are 21.3 J kg^{-1} K^{-1}, 21.7 J kg^{-1} K^{-1} and 22.9 J kg^{-1} K^{-1} around 6.5 K, 4.5 K and 3.5 K respectively during a change of magnetic induction intensity from 0-5 T,[137] while the magnetic entropy of $ErCr_2Si_2$ attained 29.7 J kg^{-1} K^{-1} near the magnetic ordering temperature 4.5 K.[137] The crystal structure of the RT_2X_2 series is body centred tetragonal

$ThCr_2Si_2$-type (with space group I4/mmm),[71, 91, 140-142] with the sequence -R-X-T-X-R- atomic layers stacked along the c-axis. The rare earth elements typically exhibit large magnetic moment (for example the $M_{Tb} = 8.8\ \mu_B$ in $TbMn_2Si_2$ at 5 K)[160] and correspondingly make a large contribution to the magnetocaloric effect.[137-139] Given the sensitivity of the magnetic state in RMn_2X_2 to the intra-planar Mn-Mn spacing,[71, 140, 144, 145] compounds in this series are found to display a rich variety of interesting phenomena, including superconductivity, magnetism, mixed valence, heavy fermions, and Kondo behaviour.[146-148] This diversity enables control of the interplay between the R-Mn and Mn-Mn exchange interactions in RMn_2X_2 through external factors such as pressure,[149] temperature and magnetic field[150]meaning that such compounds have the potential for competitive performance.[71, 140, 145] Using standard magnetic methods[140, 151] $TbMn_2Ge_2$ was found to be antiferromagnetic below Néel temperature T_N = 410 K and ferromagnetic below T_C = 95 K, $TbMn_2Ge_2$ exhibits a collinear ferrimagnetic structure in which the Tb moments order ferromagnetically and couple antiferromagnetically with the Mn moment.[144] Meanwhile the thermal expansion anomaly of a-axis was found near T_C.[144] Furthermore, for the $Tb_{1-x}Y_xMn_2Ge_2$ series (x = 0-0.4), the replacement of Y for Tb leads to a significant modifications of both Curie temperature (from 76 K to 0 K for $TbMn_2Ge_2$ and $Tb_{0.6}Y_{0.4}Mn_2Ge_2$ respectively) and magnetovolume effect (the volume effect is $\Delta V/V = 3.2\times10^{-3}$ and 2.7×10^{-3} for x = 0 and 0.1 respectively).[151] The magnetic phase transitions around T_C in the Tb-rich $Tb_{1-x}Y_xMn_2Ge_2$ compounds were shown to be first order,[151] offering scope for large magnetocaloric effects around the region of their Curie temperatures.

Here we present a systematic study of the magnetic transition from antiferromagnetism to ferromagnetism in a series of $Tb_{1-x}Y_xMn_2Ge_2$ samples (x = 0, 0.1, 0.2) using a combination of methods including variable temperature x-ray diffraction (XRD), specific heat, differential scanning calorimetry (DSC) and magnetization measurements. The overall aim is to understand fully the influence of Y substitution for Tb in the search for novel magnetocaloric materials that may be suitable for operation over the hydrogen and natural gas liquefaction temperature ranges.

6.2 Experimental Techniques

The polycrystalline $Tb_{1-x}Y_xMn_2Ge_2$ samples with x = 0, 0.1, 0.2 were prepared by arc melting constituent elements of 99.9 % purity under argon atmosphere. For improved crystallization

and chemical homogeneity, the samples were annealed in vacuum-sealed quartz tube at 850°C for 7 days after arc melting. The dc magnetic measurements were performed using a Quantum Design 9 T physical properties measurement system (PPMS). The magnetic behaviour was investigated over the range from 5 K to 340 K in a magnetic field 0.01 T. Differential scanning calorimetry measurements were performed on differential scanning calorimetry equipment (DSC 204 **F1** Phoenix®) from 340 K to 500 K. Magnetization-field loops were obtained at temperatures close to the Curie temperature of samples with magnetic fields over the range 0-5 T. The heat capacity measurements were performed on a Quantum Design 14 T physical properties measurement system scanning from 2 K to 250 K. Finally, the structures of the samples were characterized by variable temperatures XRD measurements over the temperature range (12-300 K) using a PANAlytical diffractometer with Cu-Kα radiation.

6.3 Results and Discussion

6.3.1 Structural Behaviour

The room temperature x-ray diffraction study shows that all samples are single phase and that patterns can be indexed with a space group of I4/mmm as expected. The Rietveld refinements have been carried out using the FullProf package with the main results shown in Fig. 6.1(a), (b) and (c) for x = 0, 0.1 and 0.2 respectively. It can be seen from Fig. 6.1. that the variations of lattice parameters of a and c with temperature display strong anisotropy: the lattice parameter c (red solid circle) increases monotonically with increasing temperature while a pronounced discontinuity is observed in the a lattice parameter (black solid square) around the Curie temperature T_c for each sample (the transition temperatures determined as the point where the value of the dM/dT is minimum). The discontinuity in the a lattice parameter around T_c leads to the associated decrease in the unit cell volume for all samples as also evident in Fig. 6.1. These behaviours are very similar to the behaviour reported for $Pr_{0.5}Y_{0.5}Mn_2Ge_2$[91] (i.e. $PrMn_2Ge_2$ diluted by Y), but different from $NdMn_2Ge_{0.4}Si_{1.6}$,[70] $NdMn_{1.9}Ti_{0.1}Si_2$[153]and $NdMn_{1.7}Cr_{0.3}Si_2$[70] (Mn diluted with transition metal Ti or Ge diluted by Si) for which the lattice parameter a shrinks with increasing temperature around T_C while the lattice parameter c expands. In order to derive the magneto-volume effect below T_C, we have calculated the contribution from lattice vibration using the Debye model which can be obtained through

$$\beta = k\gamma C_v/V \quad (6.1)$$

where β is the volume thermal expansion coefficient of the parameter state, k is the compressibility, γ is the Gruneisen constant and C_v is the specific heat at constant volume caused by lattice vibrations. C_v was derived from the Debye theory of the specific heat using the value of the Debye temperature θ_D (as derived from our specific heat measurements described in **Section 6.3.5** [Heat Capacity study] for the three compositions)

$$C_v = 9Nk_B(\frac{T}{\Theta_D})^3 \int_0^{\Theta_D/T} \frac{x^4 e^x}{(e^x-1)^2} dx \quad (6.2)$$

where k_B is Boltzmann constant, N is the number of the atoms. The thermal expansion for the hypothetical paramagnetic state is given by integrating Eq. (6. 2) with respect to temperature. The parameter $k\gamma/V$ was adjusted to get the best least-squares fitting to the successive data points of the observed thermal expansion curve well above the magnetic ordering temperature (based on the fact that the magnetic contribution in the antiferromagnetic region to total thermal expansion can be ignored for these types of compounds).[70]

The temperature dependence of the unit cell volumes based on Debye theory for the $TbMn_2Ge_2$, $Tb_{0.9}Y_{0.1}Mn_2Ge_2$ and $Tb_{0.8}Y_{0.2}Mn_2Ge_2$ samples are shown by the dashed lines in Fig. 6.1(a), (b) and (c) with pronounced magneto-volume effects evident below their magnetic transition temperatures T_C = 94 K, T_C = 83 K and T_C = 70 K respectively. The discontinuous nature of the changes in *a* lattice parameter and unit cell volume *V* at the Curie temperatures as shown in Fig. 6.1., are consistent with the first order nature of these transitions as discussed fully in **Section 6.3.4** [Magnetocaloric effect].

The changes in the *a* lattice parameters are $\Delta a/a$ = 0.125%, 0.124% and 0.130% for x = 0, 0.1 and 0.2 respectively with spontaneous volume magnetostriction ω_s (= $\Delta V/V$) at 5 K determined as: $TbMn_2Ge_2$ - $\omega_s = 4.1\times10^{-3}$; $Tb_{0.9}Y_{0.1}Mn_2Ge_2$ - $\omega_s = 3.2\times10^{-3}$ and $Tb_{0.8}Y_{0.2}Mn_2Ge_2$ - $\omega_s = 5.8\times10^{-3}$.

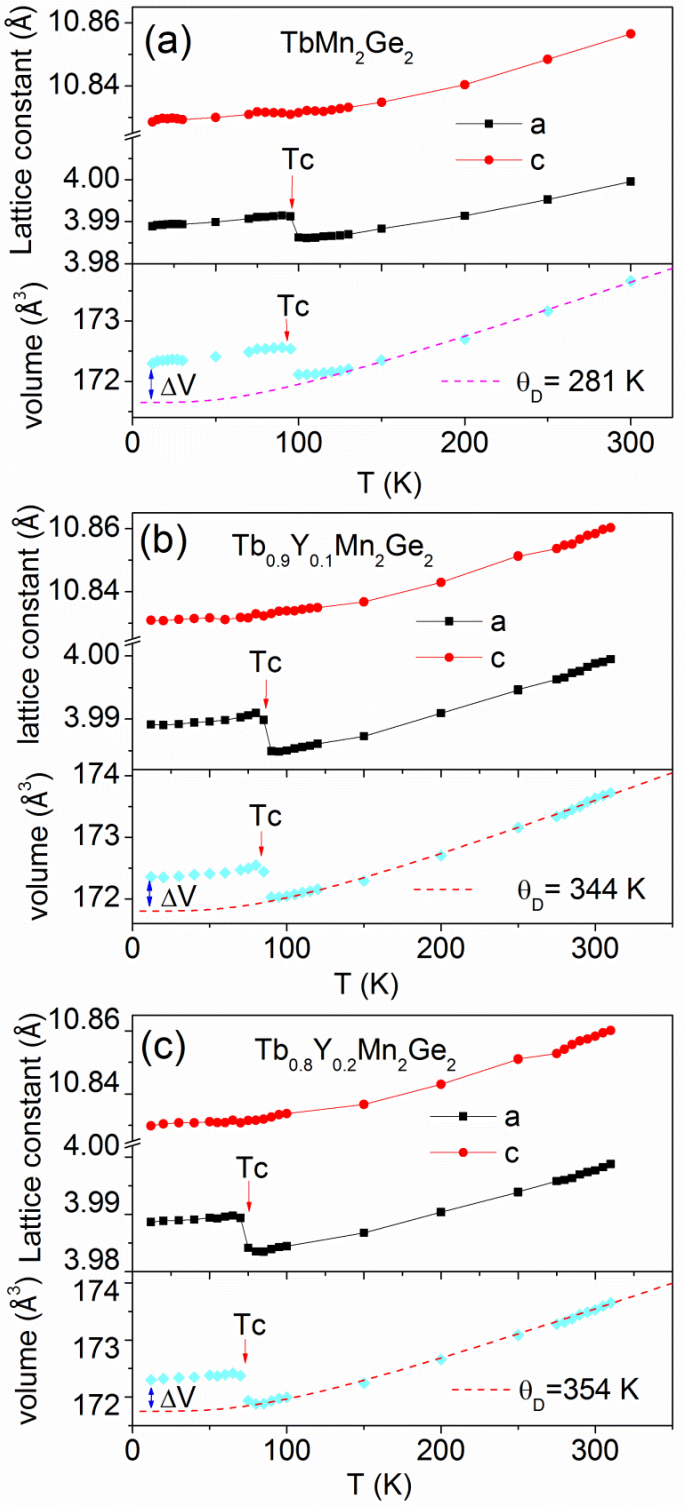

Fig. 6.1. Temperature dependence of lattice constants *a*, *c* and unit cell volume. (a) $TbMn_2Ge_2$, (b) $Tb_{0.9}Y_{0.1}Mn_2Ge_2$ and (c) $Tb_{0.8}Y_{0.2}Mn_2Ge_2$. The dashed lines show the phonon contribution to the lattice expansion as evaluated from the Gruneisen relation.

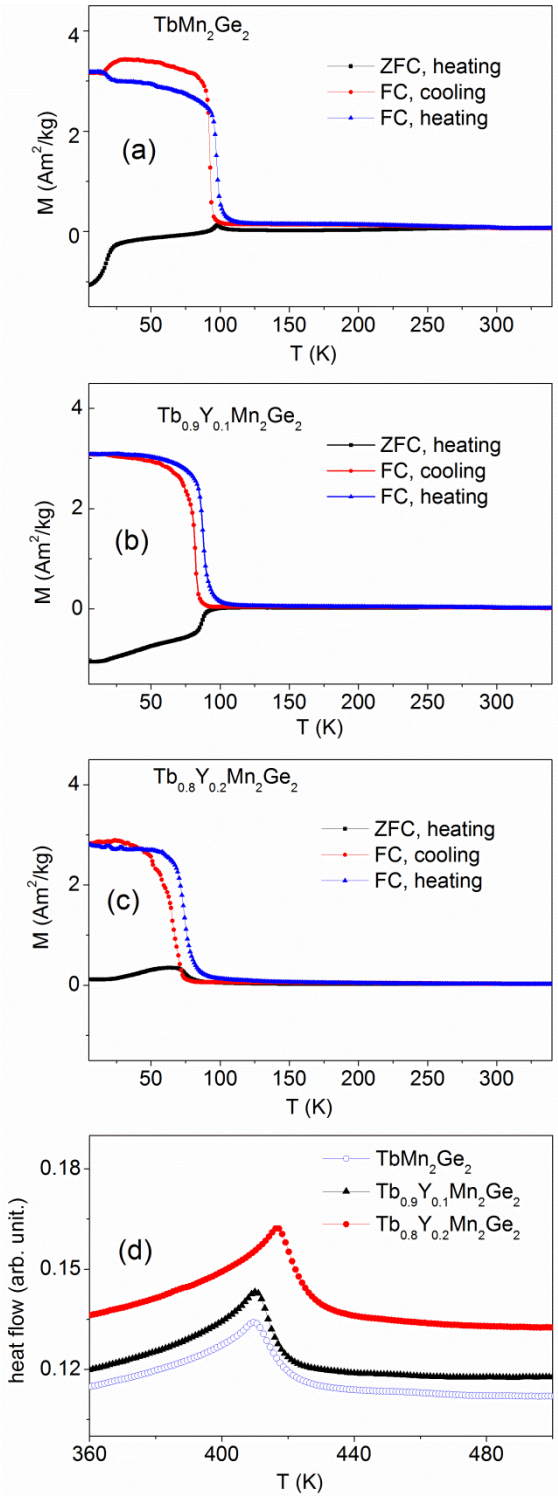

Fig. 6.2. Temperature dependence of magnetization on ZFC heating, FC cooling and FC heating processes under a field of B = 0.01 T. (a) $TbMn_2Ge_2$, (b) $Tb_{0.9}Y_{0.1}Mn_2Ge_2$ and (c) $Tb_{0.8}Y_{0.2}Mn_2Ge_2$. (d) the differential scanning calorimetry curves for the three samples over the range ~300-500 K.

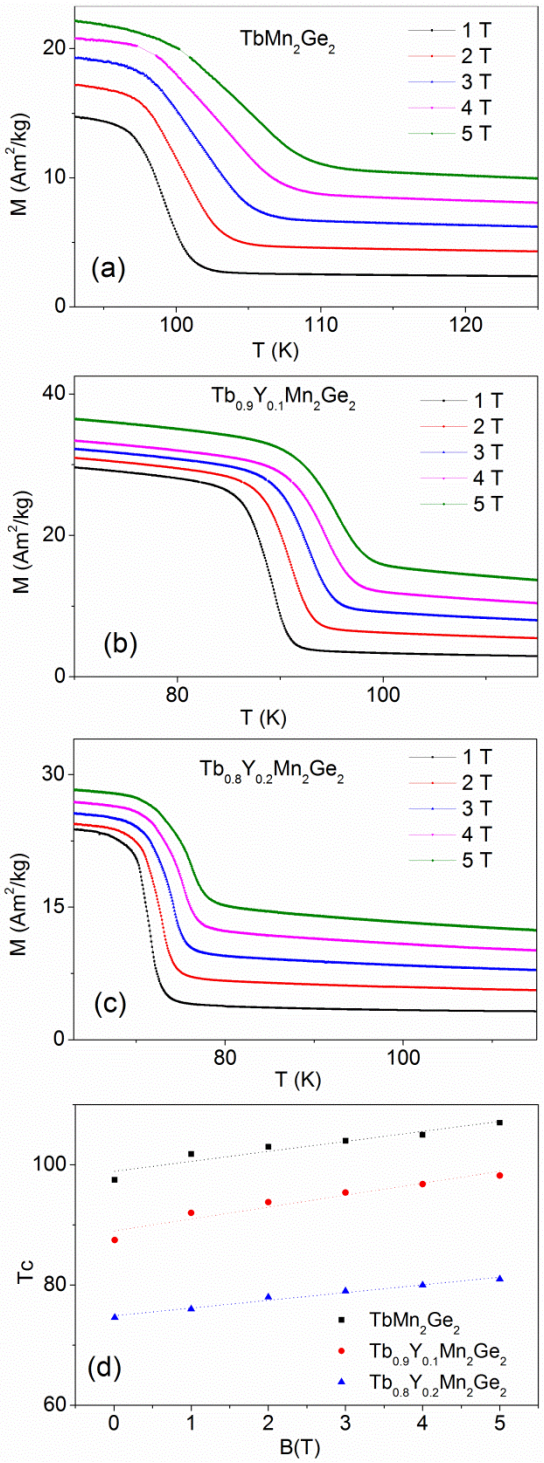

Fig. 6.3. The magnetisation versus temperature curves during cooling under various magnetic field (B = 1-5 T). (a) $TbMn_2Ge_2$, (b) $Tb_{0.9}Y_{0.1}Mn_2Ge_2$, (c) $Tb_{0.8}Y_{0.2}Mn_2Ge_2$. (d) The variation of ferromagnetic transition temperature T_c with magnetic field for the three samples. The dashed lines represent linear fits to the T_c-B curves leading to dT_c/dB values for each sample.

6.3.2 Magnetic Phase Transition

The magnetisation of the three samples have been measured in a field of B = 0.01 T over the temperature range 5–340 K. As in Figs. 6.2(a), (b) and (c), the $TbMn_2Ge_2$, $Tb_{0.9}Y_{0.1}Mn_2Ge_2$ and $Tb_{0.8}Y_{0.2}Mn_2Ge_2$ samples were respectively measured on warming from 5 K in three states: after cooling in zero field (ZFC heating) and after cooling and heating in a field of B = 0.01 T (FC cooling and FC heating). As is evident from the magnetisation versus temperature curves of Fig. 2a, b and c, there is an abrupt change in magnetisation at the Curie temperature T_C^{inter} that marks the magnetic phase transition from a collinear antiferromagnetism (AFil) at higher temperature to a collinear ferrimagnetic structure along the c axis at lower temperature according to the neutron diffraction study on $TbMn_2Ge_2$.[144] Specifically, $TbMn_2Ge_2$ has the highest T_C^{inter} (warm) = 97.5 K and T_C^{inter} (cool) = 93.0 K determined from its FC heating and cooling M-T curves, respectively. While the values for $Tb_{0.9}Y_{0.1}Mn_2Ge_2$ are derived to be T_C^{inter} (warm) = 87.5 K and T_C^{inter} (cool) = 81.8 K with the values for $Tb_{0.8}Y_{0.2}Mn_2Ge_2$ being T_C^{inter} (warm) = 74.6 K and T_C^{inter} (cool) = 66 K (normally we choose the transition temperature during the FC process as the Curie temperature T_c). As expected, the higher the level of doping of non-magnetic Y atoms in $Tb_{1-x}Y_xMn_2Ge_2$, the lower the magnetic phase transition temperature.[151]

Differential scanning calorimetry measurements have been carried out on the $Tb_{1-x}Y_xMn_2Ge_2$ samples over the temperature range 300–500 K (Fig. 6.2(d)) in order to investigate the paramagnetic to antiferromagnetic transition[144] at T_N^{inter}. As revealed by the DSC results in Fig. 6.2(d), the T_N^{inter} transition temperatures are found to increase slightly with increasing Y concentration - T_N^{inter} = 409 K, T_N^{inter} = 410 K and T_N^{inter} = 417 K for x = 0.0, 0.1 and 0.2 respectively. Compared with the reduction in ferromagnetic transition temperature on replacement of Tb atoms by Y atoms, the paramagnetic to antiferromagnetic transition temperatures are found to exhibit a slight increase (Fig. 6.2). The increase in T_N^{inter} values is due to enhancement of the Mn-Mn exchange interaction as a result of the slight reduction of Mn-Mn distance. This behaviour is similar to the $PrMn_2Ge_{2-x}Si_x$ system[154] in which the paramagnetic to antiferromagnetic transition temperatures are found to increase slightly while the antiferromagnetic to ferromagnetic transition temperatures decrease on replacing Ge with Si.

The temperature dependences of magnetization for $TbMn_2Ge_2$, $Tb_{0.9}Y_{0.1}Mn_2Ge_2$ and $Tb_{0.8}Y_{0.2}Mn_2Ge_2$ under various external magnetic fields are presented in Fig. 6.3(a), 6.3 (b) and 6.3 (c) respectively. As expected the ferromagnetic transition temperature T_C^{inter} is shifted

to higher temperature with increase in applied magnetic field. For example, the transition temperatures are T_C^{inter} = 101.8 K, 92 K and 76 K for $TbMn_2Ge_2$, $Tb_{0.9}Y_{0.1}Mn_2Ge_2$ and $Tb_{0.8}Y_{0.2}Mn_2Ge_2$ respectively in an external magnetic field of B = 1 T, while the transition temperatures are shifted to T_C^{inter} = 107 K, 98.2 K and 81 K respectively in a field of B = 5 T. The field dependence of the magnetic transition temperatures are summarized in Fig. 6.3(d). The values of dT_c/dB (obtained on linear fitting of the experimental data in Fig. 6.3(d)) along with a summary of experimental data determined for $Tb_{1-x}Y_xMn_2Ge_2$ (x = 0, 0.1, 0.2) in this investigation, is provided in Table 6.1.

6.3.3 Y Doping in $Tb_{1-x}Y_xMn_2Ge_2$ - Chemical Pressure Effect

As noted above, the effect of replacing the magnetic rare earth Tb with the nonmagnetic ion Y in $Tb_{1-x}Y_xMn_2Ge_2$ is to weaken the exchange interaction between magnetic ions due to the dilution effect. The magnetic behaviour of Y-doped $Tb_{1-x}Y_xMn_2Ge_2$ will also be modified as a result of chemical pressure due to differences in the atomic radii of the Tb (1.80 Å) and Y(1.78 Å) ions and resultant changes in lattice parameters. In order to separate these two contributions-dilution effect and pressure effect and their influence on the variation in magnetic transition temperature, the decrease of TC by chemical pressure was calculated as follows. The chemical pressure Δp was calculated[141, 142, 153] according to the Murnaghan equation below:

$$\Delta p(V) = \frac{B_0}{B_0'}\left(\left(\frac{V_0}{V}\right)^{B_0'} - 1\right) \tag{6.3}$$

where V_0, B_0 and B_0' are the volume, bulk modulus and its first derivative. Here, due to the similarity of crystal structure for the RMn_2Ge_2 system, we assume that the values of B_0 and B_0' for $PrMn_2Ge_2$ (B_0 = 38.0 Gpa, B_0' = 19.5 as derived from our synchrotron data under external pressure[155]) can be applied to $TbMn_2Ge_2$ at room temperature. Given that the doped materials $Tb_{1-x}Y_xMn_2Ge_2$ (x = 0.1, 0.2) retain the $ThCr_2Si_2$-type tetragonal structure, the chemical pressure Δp caused by doping can be assumed to have the same effect as mechanical pressure. According to previous findings that describe the pressure effect on the magnetic properties of $TbMn_2Ge_2$ (dT_c/dP = −2.9 K/kbar),[156] the values of ΔT_C can be deduced by the relationship:

$$\Delta T_c^{chemical} = dT_c/dp * \Delta p \tag{6.4}$$

where Δp is the calculated chemical pressure. The calculated values of ΔT_C for $Tb_{0.9}Y_{0.1}Mn_2Ge_2$ and $Tb_{0.8}Y_{0.2}Mn_2Ge_2$ are ΔT_C = 1.94 K and ΔT_C = 8.7 K respectively. As noted above (see also Fig. 6.1., Fig. 6.2. and Fig. 6.3.) the effect of replacing Tb atoms with Y atoms in $Tb_{1-x}Y_xMn_2Ge_2$ also contributes to the decrease in the Curie temperature. It can therefore be concluded that chemical pressure accounts for ~17.3% and ~32.2% of the decrease in transition temperatures for x = 0.1 and 0.2 respectively. In addition, the value of dT_c/dp can be derived using the Clausius-Clapeyron thermodynamic relation as follows:[91]

$$\frac{dT_c}{dp} = -\Delta V/\Delta M^*(\frac{dT_c}{dB}). \quad (6.5)$$

The values of ΔV, ΔM and dT_c/dB for each sample were taken from the present experimental results listed in Table.6.1. The derived results are dT/dp = −3.03 K/kbar, −2.84 K/kbar and −3.07 K/kbar for $TbMn_2Ge_2$, $Tb_{0.9}Y_{0.1}Mn_2Ge_2$ and $Tb_{0.8}Y_{0.2}Mn_2Ge_2$, respectively. These calculated values are in general accord with the value of dT_c/dp = −2.9 K/kbar for $TbMn_2Ge_2$,[156] deviating by ~4.5%, ~2.1% and ~5.9% for the x = 0.0. 0.1, 0.2 samples respectively.

6.3.4 Magnetocaloric Effect

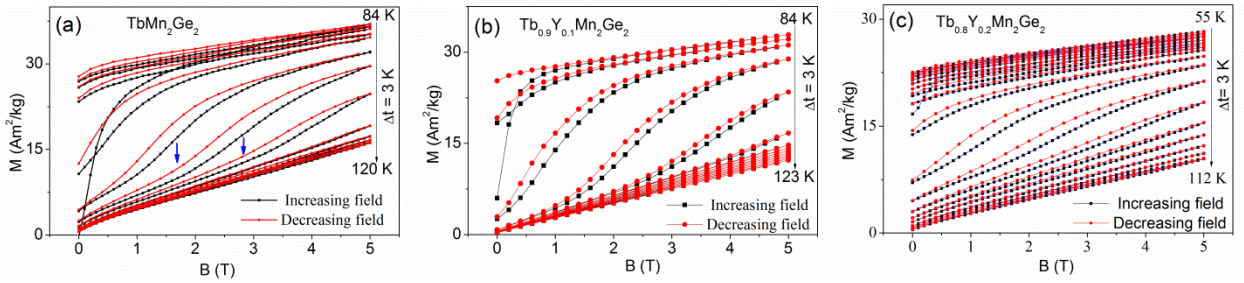

Fig. 6.4 Curves of isothermal magnetization versus magnetic field at temperatures around T_c. (a) $TbMn_2Ge_2$, (b) $Tb_{0.9}Y_{0.1}Mn_2Ge_2$ and (c) $Tb_{0.8}Y_{0.2}Mn_2Ge_2$.

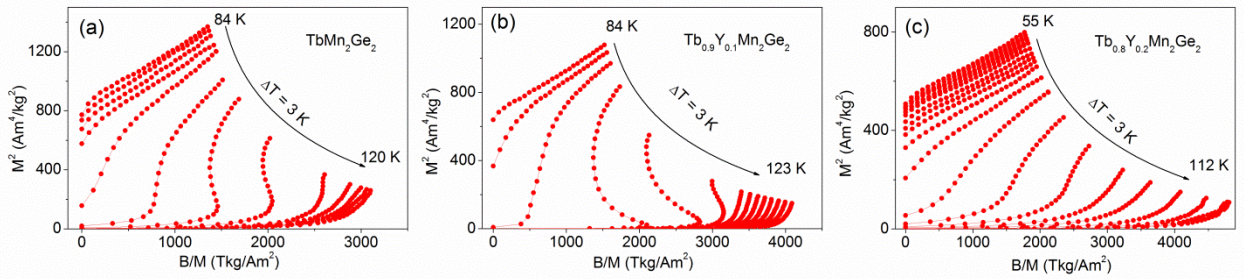

Fig.6.5 Arrott plots: isotherms graphs of M^2 versus B/M for decreasing magnetic fields at temperatures around T_c. (a) $TbMn_2Ge_2$, (b) $Tb_{0.9}Y_{0.1}Mn_2Ge_2$ and (c) $Tb_{0.8}Y_{0.2}Mn_2Ge_2$.

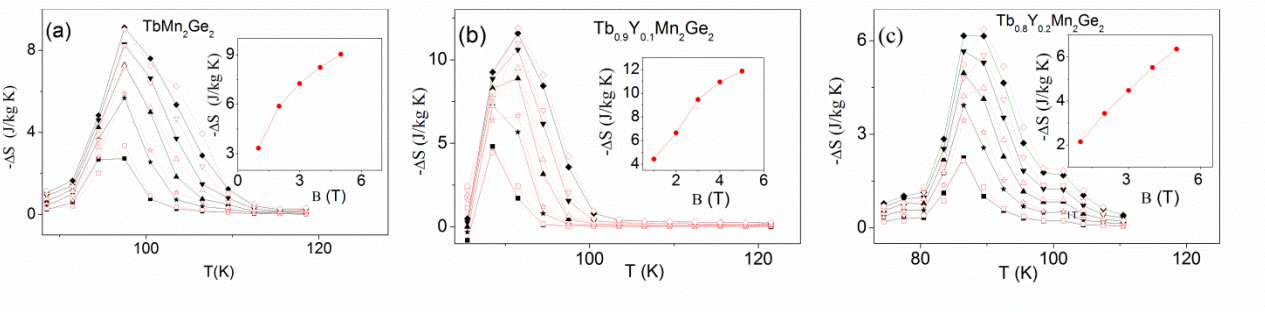

Fig.6.6 The magnetic entropy changes around the ferromagnetic transition temperatures for applied magnetic fields from 1-5 T. (a) $TbMn_2Ge_2$, (b) $Tb_{0.9}Y_{0.1}Mn_2Ge_2$ and (c) $Tb_{0.8}Y_{0.2}Mn_2Ge_2$ (black full symbols ■ ★ ▲ ▼ ◆ for 1-5 T respectively during increasing field and the red empty symbols correspond to 1-5 T for the decreasing field). The insets show the variation of the maximum values of magnetic entropy changes for the decreasing field values.

Graphs of the magnetization as a function of applied field are shown for $TbMn_2Ge_2$, $Tb_{0.9}Y_{0.1}Mn_2Ge_2$, and $Tb_{0.8}Y_{0.2}Mn_2Ge_2$ at temperatures around T_C in Fig. 4(a), (b) and (c) respectively. It can be seen that with increasing temperature beyond T_C, a field-induced metamagnetic phase transition from the antiferromagnetic state to the ferromagnetic state at certain temperatures has been detected. The region of the metamagnetic phase transition for $TbMn_2Ge_2$ is indicated by arrows in Fig. 6.4(a) as a typical example. This behaviour indicates that the region of ferromagnetic ordering in $Tb_{1-x}Y_xMn_2Ge_2$ can be shifted to higher temperatures by a stronger applied magnetic field.

The nature of the magnetic transitions (first order or second order) was analysed using Arrott plots with the magnetisation expressed in the usual way as graphs of M^2 versus B/M (Fig. 6.5.) As can be seen in Fig. 6.5(a), (b) and (c), negative slopes are detected in the M^2 versus B/M graphs for the $TbMn_2Ge_2$, $Tb_{0.9}Y_{0.1}Mn_2Ge_2$ and $Tb_{0.8}Y_{0.2}Mn_2Ge_2$ samples thus indicating that the antiferromagnetic to ferromagnetic processes are first order.[176] This conclusion also supports our crystal structure analyses above, where strong magneto-elastic coupling around T_C^{inter} has been detected (Fig. 6.1). Moreover, it is also noted that the negative slopes for $Tb_{0.8}Y_{0.2}Mn_2Ge_2$ around the antiferromagnetic to ferromagnetic transition was reduced compared with those for the $TbMn_2Ge_2$, and $Tb_{0.9}Y_{0.1}Mn_2Ge_2$ samples, indicating that the

nature of the first order transition is weakened due to the doping of non-magnetic Y. The magnetic entropy changes ΔS_M for all samples have been determined from the isothermal magnetization curves of Fig. 4a, b and c, by using the standard Maxwell relationship:

$$\Delta S_M(T,B) = \int_0^{B^{max}} \left(\frac{\partial M(B,T)}{\partial T}\right)_B dB. \quad (6.6)$$

The calculated temperature dependent magnetic entropy changes for the $Tb_{1-x}Y_xMn_2Ge_2$ samples with x = 0, 0.1 and 0.2 for both increasing field and decreasing field processes between field changes of ΔB = 0-1 T and ΔB = 0-5 T are shown in Fig. 6.6(a), (b) and (c) respectively with the maximum values ΔS_{max} shown as a function of applied field in the insets of Fig. 6.6. With a field change of ΔB = 0-5 T, the value of $-\Delta S_{max}$ are 9.1 J/kgK, 11.9 J/kgK and 6.3 J/kgK for $TbMn_2Ge_2$, $Tb_{0.9}Y_{0.1}Mn_2Ge_2$ and $Tb_{0.8}Y_{0.2}Mn_2Ge_2$ respectively, demonstrating that the entropy change for $Tb_{0.9}Y_{0.1}Mn_2Ge_2$ is the largest of the three samples. As it is clear from Fig. 6.4, while $TbMn_2Ge_2$ with the highest fraction of magnetic rare earth element and largest saturation magnetization (42.5 Am^2/kg at 84 K), its large hysteresis loss (7.40J/kg) leads to reduction in the magnetic entropy change. By comparison, with the lowest concentration of magnetic rare earth Tb, the $Tb_{0.8}Y_{0.2}Mn_2Ge_2$ sample displays the lowest saturation magnetization (only 32.5 Am^2/kg even at 55 K) and the smallest hysteresis (5.21J/kg) loss. By comparison, as shown in Fig. 6.4(b), $Tb_{0.9}Y_{0.1}Mn_2Ge_2$ with medium concentration of Tb has a relatively large saturation magnetization of 38.0 Am^2/Kg at 84 K and small hysteresis loss (0-5.36 J/kg). The refrigerant capacity (RCP), defined as the product of $-\Delta S_{max}$ and the full width at half maximum of the $-\Delta S_{max}$ curve, for the three samples are: 93.3 J/kg, 102.9 J/kg, 62.4 J/kg for $TbMn_2Ge_2$, $Tb_{0.9}Y_{0.1}Mn_2Ge_2$ and $Tb_{0.8}Y_{0.2}Mn_2Ge_2$ respectively (field change ΔB = 0-5 T). The MCE value of $Tb_{0.9}Y_{0.1}Mn_2Ge_2$ is comparable to those of other materials for a field change of ΔB = 0-5 T including: GdCoAl $-\Delta S_{max}(T)$ = 10.4 J/kgK at 100 K,[93] TbCoAl $-\Delta S_{max}(T)$ = 10.5 J/kgK at 70 K[93] and $GdMn_2Ge_2$ $-\Delta S_{max}(T)$ = 1.2 J/kgK at 95 K,[149] all of which, in common with $Tb_{0.9}Y_{0.1}Mn_2Ge_2$, importantly exhibit negligible field and thermal hysteresis losses.

6.3.5 Heat Capacity

The heat capacity of $TbMn_2Ge_2$ over the temperature range 2–250 K is shown in Fig. 6.7(a). The sharp peak in the heat capacity near the Curie temperature of $TbMn_2Ge_2$ on both zero magnetic field and a field of 2 T reflects the first order character of the magnetic phase

transition. The peak in specific heat shifts from ~98 K to 102.6 K for magnetic fields Dof 0 T and 2 T respectively; this behaviour corresponds well to the values of the Curie temperature of $TbMn_2Ge_2$ - 97.5 K (B = 0 T) to 103.0 K (B = 2 T) - obtained for the magnetisation measurements (Fig. 6.3(d)).

The heat capacity *C (T)* of a metallic magnetic material includes contributions from phonons, electrons and magnon. The relative formulas and derivation was done in **Chapter 2.2.4** Hence for the specific heat of $TbMn_2Ge_2$ at low temperatures $T \leq 10$ K, well away from the magnetic transition, as shown in Fig. 6.7(b), a fit to the graph of C_p/T versus T^2 leads to $\gamma = 65.2\ \mathrm{mJ/molK^2}, \beta = 4.37 \times 10^{-4}\ \mathrm{J/molK^4}$. The electronic density of states N (E_F) at the Fermi surface of $TbMn_2Ge_2$ compound, is derived to be 5.54 state/eV atom. Likewise, the Debye temperature θ_D can also be obtained to be θ_D = 281 K .

The magnetic entropy change, $-\Delta S_M(T, B)$ can also be derived from measurements of the in-field heat capacity using the expression thermodynamic relations below:[159]

$$\Delta S_M(T, B) = \int_0^T \frac{C(T', B) - C(T', 0)}{T'} dT' \qquad (6.11)$$

where *C (T, B)* and *C (T, 0)* are the values of the heat capacity measured in field *B* and zero field, respectively. The corresponding adiabatic temperature change, $-\Delta T_{ad}$ (shown as inset of Fig. 6.7(c) can be evaluated from $-\Delta S_M(T, B)$ and the heat capacity data.

The equivalent heat capacity parameters for $Tb_{0.9}Y_{0.1}Mn_2Ge_2$ and $Tb_{0.8}Y_{0.2}Mn_2Ge_2$ are shown in Fig. 6.8. and Fig. 6.9. respectively. The Debye temperatures were found to increase from 281 K for $TbMn_2Ge_2$ to 344 K for $Tb_{0.9}Y_{0.1}Mn_2Ge_2$ and 354 K for $Tb_{0.8}Y_{0.2}Mn_2Ge_2$, which can be understood in the terms of the difference in their molecular mass.[169] And the adiabatic temperature change near the Curie temperature decreases from 2.6 K to 2.3 K and 1.8 K for $TbMn_2Ge_2$, $Tb_{0.9}Y_{0.1}Mn_2Ge_2$ and $Tb_{0.8}Y_{0.2}Mn_2Ge_2$ respectively. The electron density at the Fermi surface is found to decrease from 5.54 state/eV atom for $TbMn_2Ge_2$ to 2.18 state/eV atom and 3.06 state/eV atom for $Tb_{0.9}Y_{0.1}Mn_2Ge_2$ and for $Tb_{0.8}Y_{0.2}Mn_2Ge_2$ respectively. The modification of the electron density at the Fermi surface may be related to the difference of electronic configuration of Y and Tb as well as the unit cell size variation.

6.4 Conclusion

In conclusion, we have carried out a detailed investigation around the region of the magnetic transitions of compounds in the $Tb_{1-x}Y_xMn_2Ge_2$ series (x = 0, 0.1, 0.2) by variable temperature x-ray diffraction, heat capacity, differential scanning calorimetry and magnetic measurements. Two magnetic phase transitions occur at T_N^{inter} and T_C^{inter} for each of the three samples. The antiferromagnetic transition at T_N^{inter} is shown to increase slightly with increase in the Y concentration, while the ferromagnetic transition at T_C^{inter} drops significantly. The mechanism of reduction of T_C due to the substitution of Y for Tb has been analysed and chemical pressure is found to play a significant role. Moreover, the entropy change of $Tb_{0.9}Y_{0.1}Mn_2Ge_2$ is found to exhibit very good magneto-caloric performance around T_C^{inter} ($-\Delta S$ = 11.9 J kg^{-1} K^{-1} and RCP = 102.9 J kg^{-1} for a field change of ΔB = 0-5 T) with very little hysteresis loss of. This behaviour reflects the potential suitability of $Tb_{0.9}Y_{0.1}Mn_2Ge_2$ for operation as a magnetic refrigerant below the nature gas liquefaction temperature. The Debye temperature and the density of states N (E_F) at the Fermi level have been determined and analysed from the heat capacity.

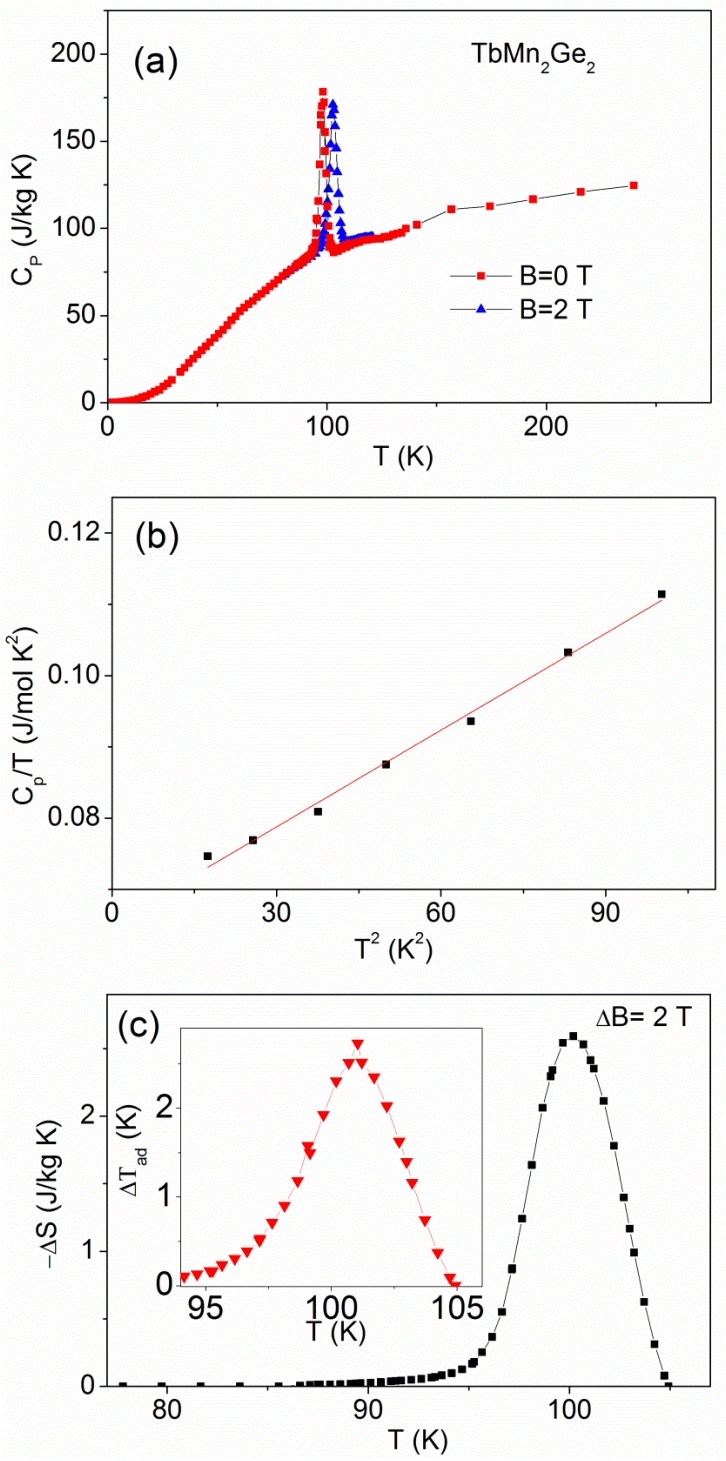

Fig. 6.7 The specific heat capacity relative parameters for $TbMn_2Ge_2$. (a) The specific heat capacity C_P of $TbMn_2Ge_2$ over the temperature range 2-250 K in zero magnetic field (red solid square) and a field of 2 T (blue solid triangle). (b) A graph of C_p/T versus T^2 for $TbMn_2Ge_2$ at temperatures below 10 K. (c) Magnetic entropy change $-\Delta S$ as a function of temperature derived from the specific heat data of Fig. 7a for ΔB = 0-2 T. The inset shows the corresponding adiabatic temperature change, ΔT_{ad}.

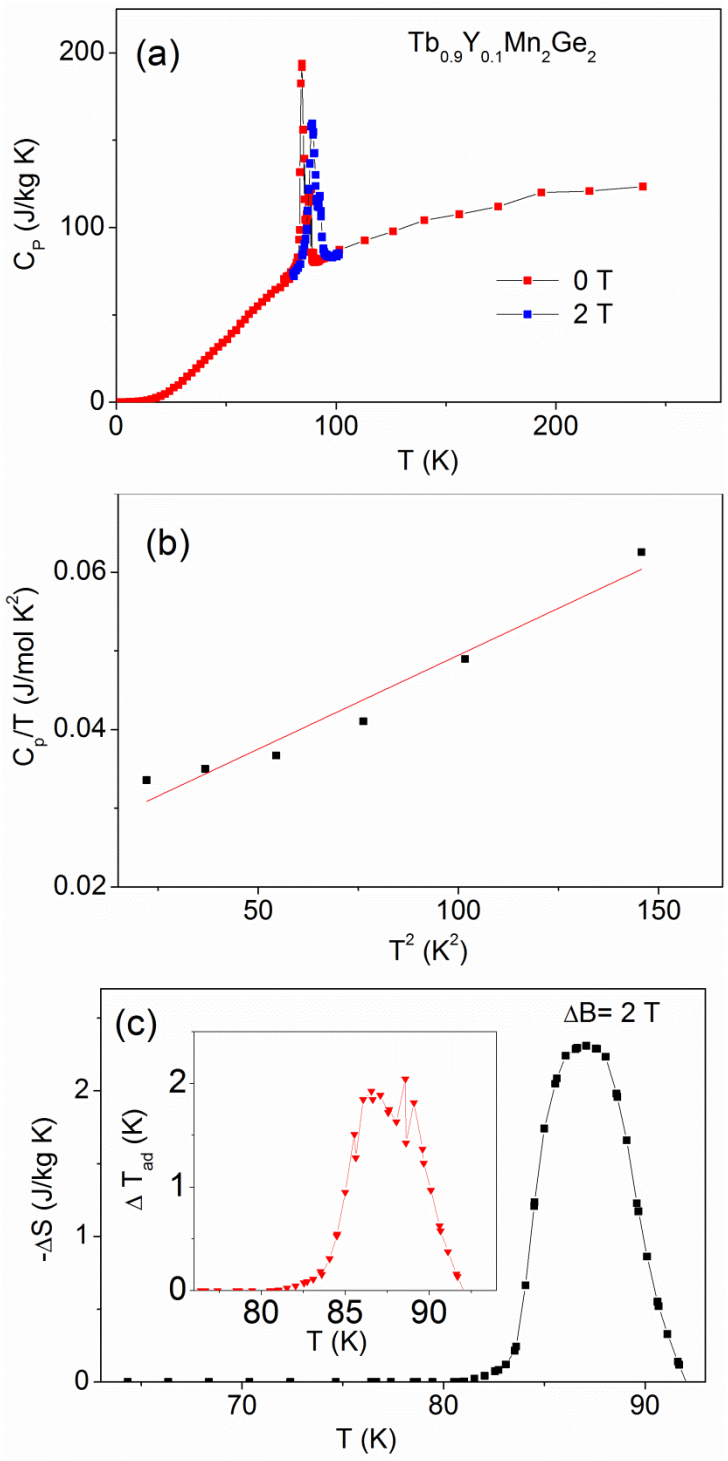

Fig. 6.8 The specific heat capacity relative parameters for $Tb_{0.9}Y_{0.1}Mn_2Ge_2$. (a) The specific heat capacity C_P of $Tb_{0.9}Y_{0.1}Mn_2Ge_2$ over the temperature range 2-250 K in zero magnetic field (red solid square) and a field of 2 T (blue solid triangle). (b) A graph of C_p/T versus T^2 for $Tb_{0.9}Y_{0.1}Mn_2Ge_2$ at temperatures below 10 K. (c) Magnetic entropy change $-\Delta S$ as a function of temperature derived from the specific heat data of Fig. 8a for ΔB = 0-2 T. The inset shows the corresponding adiabatic temperature change, ΔT_{ad}.

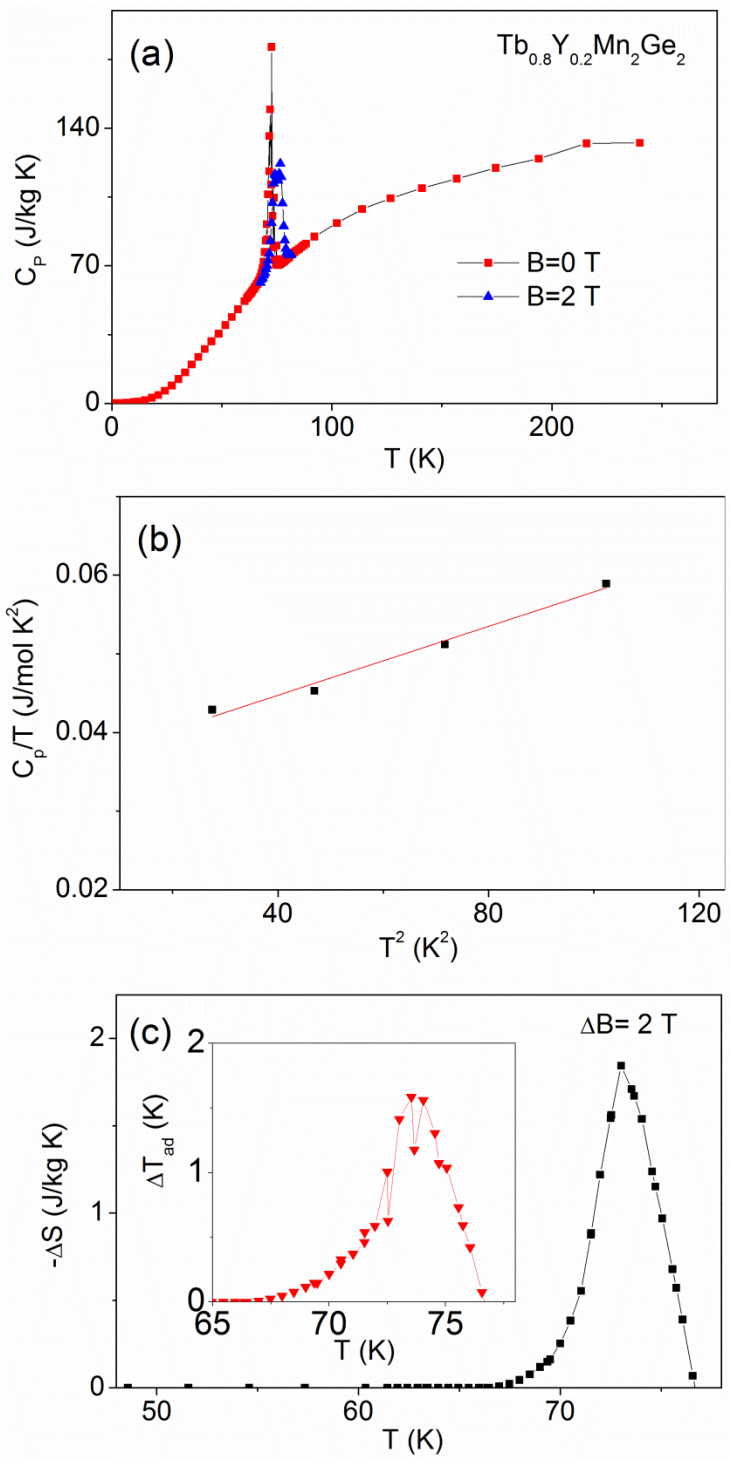

Fig. 6.9 The specific heat capacity relative parameters for $Tb_{0.8}Y_{0.2}Mn_2Ge_2$. (a) The specific heat capacity C_P of $Tb_{0.8}Y_{0.2}Mn_2Ge_2$ over the temperature range 2-250 K in zero magnetic field (red solid square) and a field of 2 T (blue solid triangle). (b) A graph of C_p/T versus T^2 for $Tb_{0.8}Y_{0.2}Mn_2Ge_2$ at temperatures below 10 K. (c) Magnetic entropy change $-\Delta S$ as a function of temperature derived from the specific heat data of Fig. 9a for ΔB = 0-2 T. The inset shows the corresponding adiabatic temperature change, ΔT_{ad}.

Table 6.1. Experimental data for the three $Tb_{1-x}Y_xMn_2Ge_2$ samples (x = 0, 0.1 and 0.2). Y composition x, chemical pressure Δp, lattice volume at 300 K, difference values of volume ΔV and moment ΔM during the structural transition on magnetic field 1 T, value of T_c during the FC process, the value of dT_c/dB, the total difference value of Curie temperature $\Delta T_c{}^{total}$ between $Tb_{1-x}Y_xMn_2Ge_2$ (x = 0, 0.1 and 0.2) and $TbMn_2Ge_2$, the derived values of $\Delta T_c{}^{chemical}$ (caused by chemical pressure) and dT_c/dp of $Tb_{1-x}Y_xMn_2Ge_2$ (x = 0, 0.1 and 0.2).

x	0	0.1	0.2
Δp (Gpa)	0	0.012	0.053
$V(^{0}_{A}{}^{3})$ (300 K)	173.66	173.63	173.53
ΔV $(^{0}_{A}{}^{3})$	0.4	0.52	0.54
ΔM (Am^2/kg) (B = 1 T)	14.0	28.2	22.7
experimental T_c (K) (FC)	93.0	81.8	66.0
$\Delta T_c{}^{chemical}$ (K)	0	1.94	8.70
$\Delta T_c{}^{total}$ (K)	0	11.2	27.0
$\Delta T_c{}^{chemical}/\Delta T_c{}^{total}$	0	17.3%	32.2%
dT_c/dB (cooling)	1.06	1.54	1.29
dT_c/dp (K/kbar) (FC)	−3.03	−2.84	−3.07

Table 6.2. Calculated heat capacity parameters for $Tb_{1-x}Y_xMn_2Ge_2$ (x = 0, 0.1, 0.2). electronic heat capacity coefficient γ, phonon heat capacity coefficient β, electronic density of states N (E_F) and Debye temperature θ_D.

x	γ ($mJ/molK^2$)	β ($J/molK^4$)	N (E_F) (state/eV atom)	θ_D (K)
0	65.2	4.37×10^{-4}	5.54	281
0.1	25.6	2.39×10^{-4}	2.18	344
0.2	36	2.19×10^{-4}	3.06	354

CHAPTER 7 CONCLUSIONS AND RECOMMENDATIONS

7.1 Introduction

Research was conducted on RCo_2Mn_x (R = Tb, Ho, Dy, $0 \leq x \leq 1.0$) series compounds. It was found that all the Mn doped samples are isostructural to the original RCo_2 series compounds with the cubic $MgCu_2$ structure ($Fd\bar{3}m$ space group). The Mn doping effects on the magnetic properties, such as the Curie temperature T_C, coercivity H_C, spontaneous magnetic moment M_S, and magnetic entropy change $-\Delta S$ were discussed specifically. We found that the Curie temperature can be raised efficiently because of the enhanced atomic exchange interaction. The spontaneous magnetic moment normally also decreased due to the Mn, which has an antiparallel coupling with the rare earth moment. Meanwhile the magnetic entropy change decreased with more Mn doping as the operation temperature increased. Furthermore, after the Mn doping, the order of the RCo_2 magnetic transition was always transformed from first order to second order. In addition, a very wide operational temperature range and high coercivity were observed respectively in $HoCo_2Mn$ and $DyCo_2Mn$. Meanwhile, the $Tb_{1-x}Y_xMn_2Ge_2$ series (x = 0, 0.1, 0.2) compounds were also studied. We found negative volume changes with increasing temperature increasing in all the samples near the Curie temperatures. The magnetic entropy change was investigated as a function of Y element doping.

So from all the above research, we totally investigated the magnetic properties affected by the element doping. To deeply understand the physical principled, critical exponent analysis was conducted. Meanwhile, high resolution neutron and synchrotron diffraction measurements were performed to clarify the magnetic structure and crystal structure. We could see that there were many influences on the magnetic properties, such as external magnetic field, element doping, mechanical or chemical pressure, etc. Beyond this thinking. we can try many other ways to tune the magnetic properties of the current magnetocaloric materials. Besides, some new materials can be produced by fusing various elements, which may lead to novel magnetocaloric materials.

7.2 Conclusions and Recommendations

7.2.1 Conclusions

We can summarize all the above work as follows:

(1). According to the investigation of $TbCo_2Mn_x$ (x = 0, 0.1, 0.2, and 0.3), with Mn increasing from x = 0 to 0.3, the Curie temperature T_C increases significantly from 227 K to 332 K, while the spontaneous magnetization at 5 K decreases from 6.19 to 5.0 μ_B/f.u. Furthermore, the nature of the magnetic transition around T_C changes from the first order for x = 0 to second order for x = 0.1, 0.2, and 0.3. The derived critical exponents are $\beta \approx 0.5$, $\gamma \approx 1.0$, and $\delta \approx 3.3$, close to the theoretical prediction from the mean-field model, indicating that the magnetic interactions are long-range. There is a rhombohedral distortion below T_C with the structure changing from cubic $Fd\bar{3}m$ above T_C to $R\bar{3}m$ below T_C.

(2). According to the investigation of the $HoCo_2Mn_x$ (x = 0, 0.2, 0.5, 0.7, and 1.0) series compounds, the Curie temperature T_C was significantly raised from 88 K for $HoCo_2$ to 253 K for $HoCo_2Mn$. Similar to $HoCo_2$, spin reorientations were also found in $HoCo_2Mn_{0.2}$, $HoCo_2Mn_{0.5}$, $HoCo_2Mn_{0.7}$, and $HoCo_2Mn_{1.0}$ near 16 K. Abnormally, a huge operational temperature range during the paramagnetism-ferromagnetism (PM-FM) transition was found with higher Mn doping: from the range of 80-120 K for $HoCo_2$ to 40-280 K for $HoCo_2Mn$. Furthermore, through critical exponent (β, γ, and δ) analysis using different techniques such as Arrott-Noaks plots, Kouvel-Fisher plots, and isotherm analysis, we found that with more Mn doping, the nature of the second order transition was transformed from the mean-field theory prediction for x = 0.2 to a slight deviation from mean-field theory for x = 0.5, 0.7, and 1.0. Finally, novel transformation from strong negative to positive thermal expansion in $HoCo_2Mn_x$ compounds has been detected. And almost zero thermal expansion over a wide temperature range (over 200 K) can be achieved in the compound $HoCo_2Mn_{0.5}$.

(3). According to the investigation of $DyCo_2Mn_x$ (x = 0, 0.1, 0.2, 0.4, 0.6, and 1.0) compounds, the value of T_C increases from 141 K to 295 K with greater Mn doping from x = 0 to 0.6, while it decreases to 268 K for x = 1.0. Meanwhile, a huge coercivity, H_C = 21170 Oe can be observed for $DyCo_2Mn$, and the value of H_C increases monotonically with increasing x value from 0 to 1.0. In addition, the spontaneous magnetic moment M_S decreases as the x value increases from 136 emu/g for x = 0 to 67 emu/g for x = 1.0. Meanwhile, the critical exponents $\beta \approx 0.5$, $\gamma \approx 1.0$, and $\delta \approx 3.0$ were calculated using different methods such as Arrott-Noaks plots, Kouvel-Fisher plots, and critical isotherm analysis. The results

proved that all the second order transitions are close to the mean-field theory predictions with long-range interaction.

(4). According to the investigation of the $Tb_{1-x}Y_xMn_2Ge_2$ series (x = 0, 0.1, and 0.2), all the compounds are proved to have two magnetic phase transitions. The first transition from the paramagnetic state (PM) to the antiferromagnetic interlayer (AFil) state occurs at T_N^{inter}, with the second transition from the AFil magnetic structure to a collinear ferrimagnetic interlayer structure at T_C^{inter}. Compared with the slight change of T_N^{inter} (409 K, 410 K, and 417 K for x = 0, 0.1, and 0.2, respectively), the replacement of Y for Tb leads to a significant decrease in T_C^{inter} from 97.5 K for x = 0 to 74.6 K for x = 0.2. To fully understand this behaviour, two effects were specifically studied: (1) chemical pressure due to the smaller atomic size of Y compared with Tb and (2) the magnetic dilution effect due to the non-magnetic nature of Y. In addition, a strong anisotropic magnet-volume effect was detected around T_C^{inter} in all the compounds with $\Delta a/a$ = 0.125%, 0.124%, and 0.130% for x = 0, 0.1, and 0.2, respectively while no obvious effect was detected along the c-axis. The maximum magnetic entropy changes were found to be $-\Delta S_{max}$ = 9.1 J kg^{-1} K^{-1}, 11.9 J kg^{-1} K^{-1}, and 6.3 J kg^{-1} K^{-1} with a field change from 0 T to 5 T for $TbMn_2Ge_2$, $Tb_{0.9}Y_{0.1}Mn_2Ge_2$, and $Tb_{0.8}Y_{0.2}Mn_2Ge_2$, respectively.

7.2.2 Recommendations

According to our research, there are many prospects for future research on the magnetocaloric materials, which can be listed as follows:

(1). For the new phase series materials, there are still many other rare earth compounds that we can explore, such as with Tm, Gd, etc. Meanwhile, various proportions of the elements can be tried to obtain pure phases with different magnetic properties. We can also produce new materials experimentally according to the predictions of theoretical calculations.

(2). The morphologies of the samples can be varied for different fabrication methods. For example, after the solid phase sintering to obtain a compound, other advanced technologies can be used to produce various forms of the material. For example we can use HV(high vacuum) Arc Melting and Single-roller Melt Spinning System to obtain nanoribbon samples, which may have novel magnetic properties.

(3).Various external conditions, such as strong magnetic field and huge mechanical pressure, can be applied during the magnetic, synchrotron or neutron measurements to study the variations in physical properties under different extreme experimental conditions.

REFERENCES

1. J. U. Ahamed, R. Saidur, H. H. Masjuki, Renew. Sustainable Energy Rev 15, 1593–600 (2011).

2. H. Xi, L. Luo, G. Fraisse, Reviews 11,923–36 (2007).

3. M. I. Karamangil, S. Coskun, O. Kaynakli, N. Yamankaradeniz, Renew. Sustainable Energy Rev 14, 1969–78 (2010).

4. X. Q. Zhai, M. Qu, L. Yue, R. Z. Wang, Renew. Sustainable Energy Rev 15, 4416–23. (2011).

5. B. Choudhury, P. K. Chatterjee, J. P. Sarkar, Renew. Sustainable Energy Rev 14, 2189–95 (2010).

6. B. F. Yu, Gao, Q. B. Zhang, X. Z. Meng, Z. Chen. Int. J. Refrig 26, 622–636 (2003).

7. W. F. Giauque, D. P.MacDougall, Phys. Lett 43, 768 (1933).

8. C. Zimm, A. Jastrab, A. Sternberg, V. K. Pecharsky, Jr K. A. Gschneidner, M. Osborne, and I. Anderson, Adv Cryog Eng 43, 1759–66 (1998).

9. W. Q. Ao, J. Q. Li,_, F. S. Liu, Y. X. Jian. Solid State Commun 141, 219–222 (2007).

10. Z. D. Han, Z. H. Hua, D. H. Wang, C. L. Zhang, B. X. Gu and Y. W. Du, J. Magn. Magn. Mater 302, 109–112 (2006).

11. F. S. Liu, W. Q. Ao, L. Wub, J. Q. Li, Intermetallics 17, 738–743 (2009).

12. J. Herrero-Albillos, F. Bartolome, L. M. García, F. Casanova, A. Labarta, X. Batlle, J. Magn. Magn. Mater 301, 378–382 (2006).

13. S. Yang, H. X. Bao, C. Zhou, Y. Wang, X. B. Ren, X. P. Song, M. Yoshitaka, K. Yoshio, T. Masahiko, and K. C. Keisuke. Phys. B 22, 046101 (2013).

14. R. Zeng, S. X. Dou, J. L. Wang, S. J. Campbell, J. Alloys Compd 509, L119–L123 (2011).

15. E. G. Gerasimov, T. Kanomata, V. S. Gaviko, Physica B 390 118–123 (2007).

16. E. Warburg, Ann Phys 13, 141–64 (1881).

17. P. Weiss, A. Piccard, Compt Rend AcSci 166, 352 (1918).

18. P. Debye, Ann Phys 81, 1154–60 (1926).

19. W. F.Giauque, J. Am. Chem. Soc 49, 1864–70 (1927).

20. N. Kurti and F. Simon. *Nature* 133, 907-908 (1934).

21. G. V. Brown, J. Alloys Compd 47, 3673–80 (1976).

22. V. K. Pecharsky, K. A. Gscdneidner, Jr, Phys. Lett 78, 4494–7 (1997).
23. C. B. Zimm, A. Sternberg, A. G. Jastrab, A. M. Boeder, L. M. Lawton, J. J. Chell, US Patent6.526.759.4 (2003).
24. V. Pecharsky, K. Gschneidner, A. Pecharsky, A. Tishin, Phys. Rev. B 64, 144406/1–13 (2001).
25. A. M. Tishin, Y. I. Spichkin, Institute of Physics, Publishing Ltd. (2003).
26. K. A. Gschneidner Jr, V. K. Pecharsky and A. O. Tsokol, Rep. Prog. Phys 68 1479–1539 (2005).
27. J. RomeroGo´mez, R. FerreiroGarcia, A. DeMiguelCatoira, M. RomeroGo´mez, Renew. Sustainable Energy Rev 17, 74–82 (2013).
28. B. K. Banerjee, Phys. Lett 12, 16 (1964).
29. A. Arrott, Phys. Rev 108, 1394 (1957).
30. P. B. María, Bartolomé. F, H. A. Julia and M. G. Luis, J. Alloys Compd 481, 8–56 (2009).
31. P. Velasco, J. Mira, F. Guinea, J. Rivas, M. J. Mart´ınez-Lope, J. A. Alonso, and J. L.Mart´ınez, Phys. Rev. B 66, 104412 (2002).
32. M. Parra-Border´ıas, F. Bartolom´e, J. Herrero-Albillos, and L. M. Garc´ıa, J. Alloys Compd 481, 48 (2009).
33. L. A. Burrola-G´andara, C. R. Santillan-Rodriguez, F. J. Rivera-Gomez, R. J. Saenz-Hernandez, M. E. Botello-Zubiate, and J. A. Matutes-Aquino, J. Appl. Phys 117, 17D144 (2015).
34. Z. Qu, L. Ling, L. Zhang, L. Pi, and Y. Zhang, Solid State Commun 151, 917 (2011).
35. S. Bustingorry, F. Pomiro, G. Aurelio, and J. Curiale, Phys. Rev. B 93, 224429 (2016).
36. S. N. Kaul, J. Magn. Magn. Mater 53, 5 (1985).
37. C. Bagnuls and C. Bervillier, Phys. Rev. B 32, 7209 (1985).
38. V. Privman, P. C. Hohenberg, and A. Aharony, in Phase Transitions and Critical Phenomena, edited by C. Domb and J. L. Lebowitz, Academic, New York, 1 (1991).
39. H. Eugene Stanley, Introduction to Phase Transitions and Critical Phenomena, Oxford University Press, New York, (1971).
40. P. Shamba, J. L. Wang, J. C. Debnath1, S. J. Kennedy, R. Zeng, M. F. Md Din, F. Hong, Z. X. Cheng, A. J. Studer, and S. X. Dou J. Phys.: Condens. Matter 25, 056001 (2013).
41. H. Eugene Stanley, J. Phys. Chem B, 115, 13963–13964 (2011).
42. B. Widom, J. Chem. Phys 43, 3898 (1965).
43. A. Arrott and J. E. Noakes, Phys. Rev. Lett 19, 786 (1967).

44. J. Mira, J. Rivas, M. Vázquez, J. M. García-Beneytez, J. Arcas, R. D. Sánchez, and M. A. Señaris-Rodríguez, Phys. Rev. B 59,123 (1999).
45. S. Mukherjee, P. Raychaudhuri, and A. K. Nigam, Phys. Rev. B 61, 8651 (2000).
46. N. Khan, A. Midya,1 K. Mydeen, P. Mandal, A. Loidl, and D. Prabhakaran. Phys. Rev. B 82, 064422 (2010).
47. H. E. Stanley, Rev. Mod. Phys 71, S358 (1999).
48. M. Bouvier, P. Lethuillier, and D. Schmitt, Phys. Rev. B 43, 13137 (1991).
49. B. Emre, I. Dincer, and Y. Elerman, Intermetallics 31, 16–20 (2012).
50. Q. Y. Dong, , J. Chen, X. Q. Zhang, X. Q. Zheng, J. R. Sun, and B. G. Shen, J. Appl. Phys. 114, 173911 (2013); J. L. Wang, C.C. Tang, G. H. Wu, Q. L. Liu, N. Tang, W. Q. Wang, W. H. Wang, F. M. Yang, J. K. Liang F. R. de Boer, K. H. J. Buschow, Solid State Commun 121, 615-618 (2002).
51. J. L. Wang, C. Marquina, M. R. Ibarra, G. H. Wu, Phys. Rev. B. 73, 094436 (2006). N. K. Singh, K. G. Suresh, A. K. Nigam, S. K. Malik, A. A.Coelho, and S. Gama, J. Magn. Magn. Mater 317, 68 (2007).
52. E. G. Gerasimov, N.V. Mushnikov, P.B. Terentev, V.S. Gaviko, A.A. Inishev, J. Alloys Compd. 571, 132–137(2013); K. Yano, Y. Tanaka, I. Matsumoto, I. Umehara, K. Sato, H. Adachi, H. Kawata, J. Phys.: Condens. Matter 18, 6891 (2006); K. Krop, Phys. B 319, 9 (2002).
53. N.V. Mushnikov, V. S. Gaviko, E. G. Gerasimov, P. B. Terent'ev, I. A. Tkach, Phys. Met. Metallogr 110, 210 (2010).
54. E. G. Gerasimov, N.V. Mushnikov, A.A. Inishev, P.B. Terentev, V.S. Gaviko, J. Alloys Compd. 680, 359-365 (2016); Bibekananda Maji, M. K. Ray, K. G. Suresh, and S. Banerjee, J. Appl. Phys 116, 213913 (2014).
55. R. Nirmala, Ya. Mudryk, V. K. Pecharsky, K. A. Gschneidner, Phys. Rev. B. 76, 014407 (2007); L. Morellon, Z, Arnold, J. Kamarad, M.R. Ibarra and P. A. Algarabel, J. Magn. Magn. Mater. 177, 1085-1086 (1998).
56. Bibekananda Maji, K.G. Suresh, A. K. Nigam, J. Magn. Magn. Mater. 322, 2415 (2010).
57. C. W. Zhang, Z. Zhang, S. Q. Wang, H. Li, J. M. Dong, N. S. Xing, Y. Q. Guo, W. Li, Solid State Commun. 142, 477 (2007).
58. J. L. Wang, M. F. Md Din, S. J. Kennedy, F. Hong, S. J. Campbell, A. J. Studer, G. H. Wu, Z. X. Cheng, and S. X. Dou, J. Appl. Phys. 115, 17E135 (2014).

59. J. L. Wang, C. C. Tang, G. H. Wu, Q. L. Liu, N. Tang, W. Q. Wang, W. H. Wang, F. M. Yang, J. K. Liang, F. R. de Boer, and K. H. J. Buschow, Solid State Commun. 121, 615 (2002).

60. D. D. Jackson, S. K. McCall, S. T. Weir, A. B. Karki, D. P. Young, W. Qiu, and Y. K. Vohra, Phys. Rev. B 75, 224422 (2007).

61. M. Halder, S. M. Yusu, M. D. Mukadam, K. Shashikala, Phys. Rev. B. 81, 174402 (2010).

62. J. L. Wang, S. J. Campbell, M. Hofmann, M. Hoelzel, R. Zeng, S. X. Dou, and S. J. Kennedy, J. Appl. Phys. 111, 07E334 (2012).

63. D. Blocht. D. M. Edwards, M. Shimizug and J. Voiront, J. Phys. F: Metal Phys. 5, 1217 (1975).

64. E. Gratzi, H. Sassikt and H. Nowotnyx, J. Phys. F: Metal Phys. 11, 429 (1981).

65. N. H. Duc, D. T. Kim Anh, P. E Brommer, Physica B 319, 1 (2002).

66.. B. K. Banerjee, Phys. Lett. 12, 16 (1964).

67. C. M. Bonilla, F. Bartolomé, L. M. García, M. Parra-Borderías, J. Herrero-Albillos, and V. Franco, J. Appl. Phys. 107, 09E131 (2010).

68. C. M. Bonilla, J. Herrero-Albillos, F. Bartolomé, L.M. García, M. Parra-Borderías, V. Franco, Phys. Rev. B 81, 224424 (2010).

69. Q. Y. Ren, W. D. Hutchison, J. L. Wang , A.J. Studer, S .J. Campbell, J. Alloys Compd. 693, 32 (2017).

70. J. L. Wang, S. J. Campbell, S. J. Kennedy, R. Zeng, S. X. Dou and G. H. Wu, J. Phys.: Condens. Matter. 23, 216002 (2011).

71. P. Kumar, K. G. Suresh, A. K.Nigam, S. K. Malik, J. Appl. Phys. 103, 013909 (2008)

72. M. A. Korotin, N.A. Skorikov, A.V. Efremov, A.O. Shorikov，J. Magn. Magn. Mater. 397，115 (2016).

73. Z. W. Ouyang, F. W. Wang, Q. Hang, W. F. Liu, G. Y. Liu, J. W. Lynn, J. K. Liang and G. H. Rao, J. Alloys Compd. 390, 21 (2005).

74. S. A. Nikitin, K. P. Skokov, Yu. S. Koshkid'ko, Yu. G. Pastushenkov, and T. I. Ivanova, Phys. Rev. Lett. 105, 137205 (2010).

75. T. Hashimoto, T. Numasawa, M. Shino, and T. Okada, Cryogenics. 21, 647 (1981).

76. V. Provenzano, A. J. Shapiro, and R. D. Shull, Nature. 429, 853 (2004).15. V. Sechovsky, D. Vasylyev, and J. Prokleska, Acta Phys. Pol., A. 113, 347 (2008).

77. A. M. Tishin, J. Magn. Magn. Mater. 316, 351 (2007).

78. M. D. Mukadam, and S. M. Yusuf, J. Appl. Phys. 105, 063910 (2009).

79. M. Kumaresavanji, C. T. Sousa, A. Pires, A. M. Pereira, A. M. L. Lopes, and J. P. Araujo, J. Appl. Phys. 117, 104304 (2015).

80. G. Aubert, D. Gignoux, F. Givord, R. Lemaire and B. Michelutti, Solid State Commun. 25, 85 (1978).

81. Y. Mudryk, D. Paudyal, A. K. Pathak, V. K. Pecharsky, and K. A. Gschneidner, Jr. J. Mater. Chem. C. 4, 4521 (2016).

82. R. Hauser, E. Bauer and E. Gratz, Phys. Rev. B. 57, 2904 (1998).

83. O. Syshchenko, T. Fujita, V. Sechovsky, M. Divis and H. Fujii, J. Alloys Compd. 438, 317 (2001).

84. M. Balli, D. Fruchart, D. Gignoux, J. Magn. Magn. Mater. 314, 16 (2007); V. Sechovsky, D. Vasylyev, and J. Prokleska, Acta Phys. Pol., A. 113, 347 (2008).

85. M. Balli, D. Fruchart, D. Gignoux, J. Alloys Compd. 455, 73 (2008).

86 . T.A. Mary, J.S.O. Evans, T. Vogt and A.W. Sleight, Science 272, 90 (1996).

87. J.L. Wang, S.J. Campbell, O. Tegus, C. Marquina and M.R. Ibarra, Phys. Rev. B 75, 174423 (2007)

88. Y. W. Long, N. Hayashi, T. Saito, M. Azuma, S. Muranaka and Y. Shimakawa, Nature (London) 458, 60(2009).

89. Koshi Takenaka, Sci. Technol. Adv. Mater. 13， 013001 (2012)

90. J. Chen, L. L. Fan, Y. Ren, Z. Pan, J. X. Deng, R. B. Yu and X. R. Xing, Phys. Rev. Lett. 110, 115901 (2013)； Jun Chen, Lei Hu, Jinxia Deng and Xianran Xing， Chem. Soc. Rev., 44, 3522-3567 (2015).

91. J. L. Wang, L. Caron, S. J. Campbell, S.J. Kennedy, M. Hofmann, Z.X. Cheng, M. F. Md Din, A.J. Studer, E. Brück and S.X. Dou, Phys. Rev. Lett. 110, 217211 (2013).

92. S. B. Roy, J. Phys.: Condens. Matter 25, 183201 (2013).

93. M. F. Md Din, J. L. Wang, S. J. Campbell, A. J. Studer, M. Avdeev, S. J. Kennedy, Q.F Gu, R. Zeng, and S. X. Dou, Appl. Phys. Lett. 104, 042401 (2014).

94. E.F. Wasserman, in Ferromagnetic Materials, edited by K.H. Buschow and E.P. Wohlfarth (North-Holland, Amsterdam) 5, 237 (1990)

95. E. Gratz and A.S. Markosyan, J. Phys.: Condens. Matter 13, R 385 (2001)

96. S. Khmelevskyi and P. Mohn, Phys. Rev. B 66, 220404® (2002)

97. S. Khmelevskyi and P. Mohn, J. Magn. Magn. Mater. 272-276, 525 (2004)

98. S. Khmelevskyi, and P. Mohn, J. Phys.: Condens. Matter, 12, 9453 (2000).

99. J. Voiron, A. Berton, and J. Chaussy, Phys. Lett. 50, 17 (1974).

100. J. L. Wang, B. García-Landa, C. Marquina, M. R. Ibarra, F. M. Yang and G. H. Wu, Phys. Rev. B. 67, 0144171 (2003).
101. N. K. Singh, K. G. Suresh, A. K. Nigam, S. K. Malik, A. A.Coelho, and S. Gama, J. Magn. Magn. Mater. 317, 68 (2007).
102. B. K. Banerjee, Phys. Lett. 12, 16 (1964).
103. M. Seeger, S. N. Kaul, H. Kronmüller, and R. Reisser, Phys.Rev B 51, 12585 (1995).
104. Bagnuls and C. Bervillier, Phys. Rev. B 32, 7209 (1985).
105. Frank H. Stillinger and Pablo G. Debenedetti, J. Phys. Chem B 103, 4052–4059 (1999).
106. J. C. Debnath, Harikrishnan S. Nair, André M. Strydom, K. Ramesh Kumar, and J. L. Wang, J. Appl. Phys 120, 233902 (2016).
107. John C. Wheeler and R. G. Petschek, Phys. Rev. A28, 2442 (1983).
108. A. Arrott and J. E. Noakes. J. Appl. Phys. 42, 1288 (1971).
109. The-Long Phan, , Y. D. Zhang, P. Zhang, T. D. Thanh, and S. C. Yu, J. Appl. Phys. 112, 093906 (2012).
110. R. Zalecki, P. Stoch, P. Guzdek, A. Kołodziejczyk, and J. Pszczoła, J. Alloys Compd. 442, 292 (2007).
111. P. Stoch, J. Pszczoła, P. Guzdek, J. Chmist, and A. Pańta, J. Alloys Compd. 394, 116 (2005).
112. C. S. Fang, J. L Wang, F. Hong, Wayne D. Hutchison, M. F. Md Din, A. J. Studer, J. A. Kimpton, S. X. Dou, and Z. X. Cheng, Phys. Rev. B. 96, 064425 (2017).
113. J. L. Wang, S. J. Campbell, M. Hofmann, M. Hoelzel, R. Zeng, S. X. Dou, and S. J. Kennedy, J. Appl. Phys. 111, 07E334 (2012).
114. N. Yoshimoto, J. Sakurai and Y. Komura, J. Magn. Magn. Mater. 34, 137-139 (1983).
115. D. P. Kozlenko, E. Burzo, P. Vlaic, S. E. Kichanov, A. V. Rutkauskas and B. N. Savenko, Scientific Reports. 5, 8620 (2015).
116. E. Burzo, P. Vlaic , D.P. Kozlenko, S.E. Kichanov, A.V. Rutkauskas , B.N. Savenko, J. Alloys Compd. 724, 1184-1191 (2017).
117. A. Kowalczyk, J. Baszyfiski, A. Szajek, J. Kovfi, I. Skorvfinek, J. Magn. Magn. Mater. 152, L279−L281 (1996).
118. J. Kamarfid, Z. Arnold, M.R. Ibarra, J. Magn. Magn. Mater. 140-144, 837−838 (1995).
119. Z. H. Nie, S. Yang, Y. D. Wang, Z. L. Wang, D. M. Liu, *and* Y. Ren, Appl. Phys. Lett. 103, 111903 (2013).
120. A. O. Pecharsky K. A. Gschneidner, Jr, V. K. Pecharsky, D. L. Schlagel and T. A. Lograsso, Phys. Rev. B. 70, 144419 (2004).

121. T. Plackowski, M. Matusiak, and J. Sznajd, Phys. Rev. B. 82, 094408 (2010).
122. N. H. Duc, P.E. Brommer, in: K.H.J. Buschow (Ed.), Handbook on Magnetic Materials, (North-Holland, Amsterdam) 12. 259 (1999).
123. H. Eugene Stanley, Introduction to Phase Transitions and Critical Phenomena-Oxford University Press, New York, (1971).
124. D. M. Rajkumar, M. Manivel Raja, R. Gopalan_, V. Chandrasekaran, J. Magn. Magn. Mater 320, 1479–1484 (2008).
125 . Gschneidner Jr, K. A. Pecharsky, V. K. and Tsokol, A. O. Rep. Prog. Phys. 68, 1479–1539 (2005); Gschneidner Jr, K. A. and Pecharsky, V. K. Int. J. Refrig 31, 945–961 (2008); Shen, B. G. Sun, J. R. Hu, F. X. Zhang, H. W. and Z. H. Cheng, Adv. Mater. 21, 4545–4564 (2009).
126 . O. Tegus, E. Brück, K. H. J. Buschow, and F. R. de Boer, Nature 415, 150–152 (2002).
127 . H. Wada, and Y. Tanabe, Appl. Phys. Lett. 79, 3302 (2001).
128 . T. Krenke, E. Duman, M. Acet, E. F. Wassermann, X. Moya, L. Mañosa, and A. Planes, Nature materials 4, 450– 454 (2005).
129. M. Pasquale, C. P. Sasso, L. H. Lewis, L. Giudici, T. Lograsso, and D. Schlagel, Phys. Rev. B 72, 094435 (2005).
130. F. Hu, X. Shen, B. G. Sun, J. R. and G. H. Wu, Phys. Rev. B 64, 132412 (2001).
131. X. X. Zhang, G. H. Wen, F. W. Wang, W. H. Wang, C. H. Yu, and G. H. Wu, Appl. Phys. Lett. 77, 3072 (2000); F. Hu, X. Shen, B. G. Sun, J. R. Cheng, Z. H. Rao, G. H. and X. X. Zhang, Appl. Phys. Lett. 78, 3675 (2001).
132. F. Casanova, A. Labarta, X. Batlle, J. Marcos, L. Mañosa, A.Planes, and S. de Brion, Phys. Rev. B 69, 104416 (2004).
133. P. J. von Ranke, M. A. Mota, D. F.Grangeia, G. Magnus, A.Carvalho, F. C. G. Gandra, A. A.Coelho, A. Caldas, N. A.de Oliveira, and S. Gama, Phys. Rev. B 70, 134428 (2004).
134. L. C. Wang, Q. Y. Dong, J. Lu, X. P. Shao, Z. J. Mo, Z. Y. Xu, J. R. Sun, F. X. Hu, and B. G. Shen, J. Alloys Compd. 587, 10–13 (2014).
135. R. Zeng, S. X. Dou, J. L. Wang, S. J. Campbell, J. Alloys Compd. 509, L119–L123 (2011).
136. Bibekananda Maji, M. K. Ray, K. G. Suresh, and S. Banerjee, J. Appl. Phys. 116, 213913 (2014).
137. W. L. Zuo, F. X. Hu, S. J. Rong, and B. G. Shen, J. Magn. Magn. Mater. 344, 96–100 (2013).
138. T. Samanta, I. Das, and S. Banerjee, Appl. Phys. Lett. 91, 152506 (2007).

139. L. W. Li, W. D. Hutchison, D. X. Huo, T. Namiki, Z. H. Qian, and K. Nishimura, Scripta Materialia. 67, 237–240 (2012).
140. S. Purwanto, M. Ohashi, H. Onodera, Y. Morii, S. Funahashi, and H. Yamauchi, Physica B 213&214, 318–320 (1995).
141. J. L. Wang, S. J. Campbell, A. J. Studer, M. Avdeev, M. Hofmann, M. Hoelzel, and S. X. Dou, J. Appl. Phys. 104, 103911 (2008).
142. Z. Ban, and M. Sikirica, Acta Crystallographica. 18, 594-599 (1965).
143. S. A.Granovsky, I. Y. Gaidukova, M. Doerr, M. Loewenhaupt, A. S. Markosyan, C. Ritter, Physica B 391, 79–87 (2007).
144. L. Morellon, P. A. Algarabel, M. R. Ibarra, and C. Ritter, Phys. Rev B 55, 12363 (1997).
145. S. Purwanto, M. Oihashi, H. Yamauchi, H. Onodem, and Y. Yamaguchr, Prosiding PertemuanI lmiah Sains Materi 1410 (1997).
146. H. R. Ott, Z. Fisk, A. J. Freeman, G. H. Lander, Handbook on the Physics and Chemistry of the Actinides, 85 (1987).
147. A. Szytula, J. Leciejewicz, K. A. Gscheidner Jr and L. Eyring, Handbook on the Physics and Chemistry of Rare Earths.133 (1989).
148. N. P. Kolmakova, A. A. Sidorenko, R. Z. Levitin, J. Low Temp. Physica 28, 653 (2002).
149. P. Kumar, K. G. Suresh, A. K. Nigam, A. Magnus, A. A. Coelho, and S. Gama, Phys. Rev. B 77, 224427 (2008).
150. G. X. Li, J. L. Wang, Z. X. Cheng, Q. Y. Ren, C. S. Fang, Appl. Phys. Lett. 106, 182405 (2015); L. W. Li, K. Nishimura, W. D. Hutchison, Z. H. Qian, D. X. Huo, and T. NamiKi, Appl. Phys. Lett 100, 152403 (2012).
151. I. S. Dubenko, I. Y. Gaidukova, S. A. Granovsky, K. Inoue, A. S. Markosyan, J. Appl. Phys. 93, 10 (2003).
152. L. B. McCusker, R. B. Von Dreele, D. E. Cox, D. Louër, and P. Scardi, J. Appl. Crystallogr. 32, 36–50 (1999).
153. M. F. Md Din, J. L. Wang, S. J. Campbell, R. Zeng, W. D. Hutchison, M. Avdeev, S. J. Kennedy, and S. X. Dou, J. Phys. D: Appl. Phys 46(44), 1–11 (2013).
154. J. L. Wang, S. J. Kennedy, S. J. Campbell, M. Hofmann, and S. X. Dou, Phys. Rev. B 87, 104401 (2013).
155. S. J. Kennedy, J. L. Wang, S. J. Campbell, M. Hofmann, and S. X. Dou, J. Appl. Phys. 115, 172617 (2014).
156. L. Morellon, Z. Arnold, J. Kamarad, M. R. Ibarra, P. A. Algarabel, J. Magn. Magn. Mater. 177, 1085–1086 (1998).

157. M. K. Ray, K. Bagani, and S. Banerjee, J. Alloys Compd. 600, 55–59 (2014).
158. R. A. Susilo, , J. M. Cadogan, R. Cobas, W. D. Hutchison, M. Avdeev, and S. J. Campbell, J. Appl. Phys. 117, 17C113 (2015).
159. R. Nirmala, A. V. Morozkin, and S. K. Malik, Phys. Rev. B 75, 094419 (2007).